An Experimental Investigation of the Mechanism of Heat Transfer Augmentation by Coherent Structures

David Owen Hubble

A dissertation submitted to the faculty of the Virginia Polytechnic Institute and State University in partial fulfillment of the requirements for the degree of

Doctor of Philosophy

in

Mechanical Engineering

Virginia Tech Department of Mechanical Engineering
Advanced Experimental Thermofluids Research Laboratory

Thomas Diller, Chairman
Pavlos Vlachos, Co-Chairman
Roger Simpson
Clinton Dancey
Scott Huxtable
Mark Stremler

02.08.2011
Blacksburg, Virginia

Keywords: heat transfer, mechanism, turbulence, heat flux sensor, particle image velocimetry, time-resolved, vortex

An Experimental Investigation of the Mechanism of Heat Transfer Augmentation by Coherent Structures

David Owen Hubble

Abstract

The mechanism by which convective heat transfer is augmented by freestream turbulence in the stagnation region was studied experimentally. Previous work has suggested that the primary mechanism for the observed augmentation is the amplification of vorticity into strong vortices which dominate the flow field near the surface. Therefore, two separate experimental investigations were performed to further study this phenomenon. In the first, the spatiotemporal convection from a heated surface was measured during the normal collision of a vortex ring. The convection was observed to increase dramatically in areas where vortices forced outer fluid through the natural convection boundary layer to the surface. Regions where fluid was swept along the surface experienced much smaller increases in convection. These observations led to the development of a mechanistic model which predicted the heat transfer based on the amount of time that fluid remained within the thermal boundary layer prior to reaching the surface. In subsequent testing, the model was able to accurately predict the time-resolved convection based solely on the transient properties of the vortex present. In the second investigation, the model was applied to the vortices which form in a stagnating turbulent flow. Three turbulence conditions were tested which changed the properties of the vortices produced. Again, the model was successful in predicting the time-resolved convection over much of the experimental measurement time.

The work of designing and calibrating the heat flux sensor used is also reported. A new sensor was developed specifically for the convection research performed herein as no existing sensor possessed the required spatiotemporal resolution and underwater capabilities. Utilizing spot-welded foils of thermoelectric alloys resulted in a very robust and sensitive sensing array which was thoroughly analyzed and calibrated. In the final section, the hybrid heat flux (HHF) method is presented which significantly increases the performance of existing heat flux sensors. It is shown (both numerically and experimentally) that by combining the spatial and temporal temperature measurements from a standard sensor, the time response increases by up to a factor of 28. Also, this method causes the sensor to be insensitive to the material to which it is mounted.

Acknowledgements

There are a number of people who have helped me reach my goal of obtaining a PhD in mechanical engineering. First, my research advisors Dr. Tom Diller and Dr. Pavlos Vlachos deserve recognition. You have taught me how to be a successful researcher but more importantly how to be a professional. Your guidance is deeply appreciated. Also, to my dissertation committee I give a sincere thank you for your help guiding this research.

No one has helped in this research more than my fellow AEThER lab mates. In particular I thank my collaborators Andrew Gifford, Clayton Pullins, Arun Mangalam, and Jerrod Ewing. I have also worked closely with a number of other lab mates including Christopher Weiland, Satya Karri, Nick Cardwell, Kelley Stewart, Dave Griffiths, Sam Raben, John Charonko, the list goes on and on. I really enjoyed are time together and hope that we can work together again in the future.

Several members of the Randolph Hall staff deserve special recognition for their help. The ladies of the ME office have helped me out of many jams with special thanks to Cathy Hill, Diana Isreal, and Renee Shack. A special thanks also goes out to the ME machine shop and Bill Songer in particular for always tolerating my requests for him to machine inconel.

My family has been very supportive of this endeavor and my life-long goal of being an engineer. No one has taught me more about engineering than my dad. My mom always pushed me to do my best and to her education is everything. For instilling in me this love of learning I say thank you.

Lastly I thank Samantha for putting our life together on hold while I pursue this degree. Thanks for bringing me supper 12 hours into a 24 hour test and putting up with me going back to work after supper. I wouldn't have been able to do this without your support.

Table of Contents

List of Figures

*Unless otherwise noted, all images are the property of the author

List of Tables

1 Introduction

1.1 Motivation

Freestream turbulence has a major effect on surface heat transfer which influences many engineering applications, for example, gas turbines, combustors, electronic cooling devices, and heat exchangers. Numerous studies have shown that elevated freestream turbulence levels cause an increase in the time-averaged heat transfer over laminar flow levels. Modeling this augmentation in such circumstances is difficult even for simple flows and geometries because of the unpredictable effect of the freestream turbulence. The mechanism by which this augmentation takes place must be understood if an accurate predictive tool is to be produced. In this work, new experimental techniques are developed and utilized to gain a deeper understanding of this complicated mechanism.

1.2 Objective and Structure of Dissertation

The objective of this dissertation is to provide an understanding of the mechanism by which convective heat transfer is augmented by freestream turbulence in stagnating flows. To accomplish this, four separate but related studies were undertaken and therefore this dissertation is broken into four sections. The following gives a brief introduction to the work performed while each individual chapter gives a more thorough introduction to the specific subject matter.

A number of researchers have performed experiments which suggest that the primary mechanism for the augmentation of heat transfer by freestream turbulence is the formation of strong vortices which dominate the flow field near the surface. Therefore, this investigation begins by attempting to determine the convection caused by an easily controlled vortex. Chapter 2 reports an experiment in which a vortex ring is produced and allowed to collide normally with a heated instrumented surface. Two time-resolved measurements technologies are exploited to quantitatively visualize the interaction. Specifically, time-resolved digital particle image velocimetry (TRDPIV) is used to investigate the time-resolved flow structure during the interaction while a time-resolved heat and temperature array (THeTA) is used to map the convective heat transfer coefficient at the surface. These measurements provide valuable insight into the mechanism by which vortices affect the heat transfer from a surface. These measurements lead to the development of a mechanistic model which is then used to predict the time-resolved convection based only on the transient properties of the vortex. Results are presented for a range of vortex parameters.

In chapter 3, the model developed in chapter 2 is applied to a flow that is more relevant from an engineering standpoint. Here the stagnation region is examined in a flow which contains large scale freestream turbulence. Again, TRDPIV is used in conjunction with a THeTA to examine the interaction process. In the stagnation region, properly oriented and scaled freestream structures are amplified into strong vortices which dominate the flow field near the surface. These vortices cause large spikes in heat transfer and as a result cause an overall increase in the time-average convection. Results are presented which shows the behavior of the vortices that form along with the simultaneously measured convection. Also, results are presented which show how the model can be applied to these complicated flow fields to obtain accurate, time-resolved convection predictions.

The work of developing and evaluating the THeTA is presented in chapter 4. While this sensor is similar to existing sensors, it is of totally new design using spot-welded thermoelectric foils to measure both the surface temperature of the sensor as well as the temperature drop across the sensor. Analytical and numerical modeling was performed to estimate the time response and sensitivity of the sensor. Calibrations were then performed applying both conductive and radiative heat fluxes to measure the sensitivity and time response. A test of the sensor's response in convection is also presented. The resulting gage should be a valuable tool for convection research as it can directly measure the time-resolved heat transfer coefficient at multiple locations simultaneously.

Chapter 5 reports the development of the hybrid heat flux (HHF) method for obtaining heat flux measurements. In this method, both the spatial and temporal temperature measurements of differential style heat flux sensors are used. By using both measurements, both the heat flowing through the gage as well as the heat being absorbed by the gage is accounted for. It is shown that this improves the time response of the sensor by up to a factor of 28 compared to utilizing the spatial measurements alone as is the standard practice. Perhaps more importantly, utilizing the hybrid method renders the sensor essentially insensitive to the material to which it is mounted. Traditionally, sensors must be mounted on a good thermal conductor for accurate measurements to be made which didn't allow their use on insulation. It is shown that when using the hybrid method, changing the thermal conductivity of the backing material four orders of magnitude causes only an 11% change in sensor output. Results are presented from both numerical and experimental testing of a sensor utilizing the HHF method. The signals from the THeTA in chapters 2 and 3 were also vastly improved by utilizing the HHF method.

The individual chapters (2-5) are presented in a journal manuscript format as each has or will be submitted to archival journals for publication. Chapters 2 and 3 have not yet been submitted. Chapter 4 has been published in the ASME Journal of Thermal Science and Engineering Application and chapter 5 has been published in the ASME Journal of Heat Transfer.

2 A Mechanistic Model for the Convection Caused by Coherent Structures: Examining a Vortex Ring Collision with a Surface

David O. Hubble, Pavlos P. Vlachos, and Tom E. Diller

2.1 Abstract

The physical mechanism by which coherent structures influence the convective heat transfer from a surface is a basic problem of fluid mechanics which plays a central role turbulence. To explore this phenomena, a well-defined structure (specifically a vortex ring) was generated which impacted a heated instrumented surface while the time-resolved characteristics of the flow field were measured. By examining both the heat transfer and flow field in a time-resolved fashion, it was observed that the surface transport was driven by the sweeping of fluid through the boundary layer by this large scale vortex structure. A physics-based mechanistic model was developed from the experimental observations which predicts the time-resolved surface convection using the transient properties of the coherent flow structure. The model was shown to predict the measured convection in a majority of the tests spanning circulation Reynolds numbers from 3100 to 9200. These results indicate the central role of large-scale structures in the augmentation of thermal transport and give a simple approach for quantitative prediction.

2.2 Nomenclature

α = thermal diffusivity (m^2/s)
β = thermal expansion coefficient (1/K)
C = specific heat (J/kg K)
d = distance (m)
D = slave piston diameter (m)
δ = boundary layer thickness (m)
g = gravitational constant
G = Grashof number
Γ = circulation (m^2/s)
h = convective heat transfer coefficient (W/m^2 K)
k = thermal conductivity (W/m K)
L = piston stroke length (m)
λ = eigenvalue

ν = kinematic viscosity (m^2/s)

Pr = Prandtl number

q" = heat flux (W/m^2)

ρ = density (kg/m^3)

St = Stanton Number

t = time (s)

T = temperature (K)

τ = time delay (s)

U = velocity (m/s)

Subscripts

$_{ci}$ = imaginary part of complex eigenvalue

$_{Lam}$ = laminar

$_{\infty}$ = freestream

$_{V}$ = vortex ring

$_{p}$ = piston

$_{S}$ = surface

$_{T}$ = thermal boundary layer

2.3 Introduction

Convective heat transfer in turbulent flows is important in many engineering applications, for example, gas turbines, combustors, electronic cooling devices, and heat exchangers. Although the turbulence present acts to increase the convective transfer, the physical mechanism of this augmentation has long been debated. Only recently have researchers used time-resolved flow field and heat flux measurements to study this phenomena. Turbulence is no longer seen as random motions at a point, but rather well defined vortices which interact with the surface. Therefore, the role that these coherent structures play should be studied if the augmented transport is to be understood.

It is recognized that large scale coherent structures play an important role in turbulent flows (Adrian 2007). Recent experiments have shown the existence of very large scale motions in the logarithmic region of turbulent boundary layers, which can reach up to twenty times the boundary layer thickness in size (Hutchins and Marusic 2007). These coherent structures have been identified as important contributors to transport in boundary layers due to their ability to increase mixing in the near wall region. This is particularly true in stagnating flows where freestream structures are aligned with the wall

and amplified through vortex stretching by the mean flow strain rate (Sutera 1965). Gifford et al. (Gifford, Diller et al.) used Time-resolved digital particle image velocimetry (TRDPIV) and a thin film heat flux sensor to study heat transfer augmentation in the stagnation region of a flow containing large scale freestream turbulence. Subsequent tracking of the vortices present showed that the rate of heat transfer at the wall was directly influenced by the strength and proximity of the coherent structures. It appeared that the largest transport occurred when the structures swept freestream fluid through the boundary layer to the surface. Two numerical studies (Romero-Mendez, Sen et al. 1998; Martin and Zenit 2008) examined the heat transfer resulting from a vortex near a surface and found similar results. In both cases they observed increases in the heat transfer in the downwash regions with a subsequent decrease in the upwash region.

Other researchers have examined the time-average influence of coherent structures on surface transport. Van Fossen and Simoneau (Vanfossen and Simoneau 1987) used wires to create vortices perpendicular to a downstream cylinder and studied the resulting fluid flow and heat transfer near the surface using a combination of smoke visualization and liquid crystals. It was observed that regions where vortices forced fluid towards the surface corresponded to regions of increased heat transfer. Xiong and Lele (Xiong and Lele 2007) used large eddy simulation (LES) to model isotropic turbulence impinging on a stagnation region. Vortices were observed to form near the stagnation boundary layer. These vortices had a stronger influence on the thermal transfer compared to the momentum transfer. Time-resolved experimental measurements of the fluctuating transport at the surface have shown direct correlation with the velocity fluctuations in the freestream (Moss and Oldfield 1996; Holmberg and Diller 2005), but the impact on the overall transport was not established.

Vortex rings represent a canonical type of fluid flow that has been extensively investigated and very well understood from a fluids standpoint (Shariff and Leonard 1992) but not from a heat transfer standpoint. To study the vortex ring-wall interaction (Doligalski, Smith et al. 1994) provides an attractive system due to the simplicity and reproducibility of their generation. Moreover, in contrast to coherent structures in boundary layers, whose strength depends on the external flow, the strength of the vortex ring can be independently controlled and is decoupled from the boundary layer. This makes the vortex ring a good model to study the mechanism by which vortices effect the convection from a surface. In one recent experimental investigation (Arevalo, Hernandez et al. 2007) a vortex ring was created in air and allowed to impact a heated vertical plate. The spatially averaged heat transfer from the surface was

found to increase by up to 15% over natural convection levels while the vortex was in contact with the surface, but they lacked the ability to resolve the heat flux in space or time.

A physics based model of turbulence was recently developed by Marusic et al. (Marusic, Mathis et al. 2010). They showed that the inner boundary layer small-scale structure was directly influenced by the large-scale outer flow structures. The elegance of their model stems from its ability to predict the near wall flow structure, which is very challenging to measure or accurately model, using information from the large scale external flow. A similar concept is used here to model the heat transport at the wall examining only the large scale outer structure. Vortices are produced which interact with a heated surface. During the interaction, the time-resolved convective heat transfer resulting from the vortex interaction is examined in conjunction with the fully resolved two-dimensional flow field. Combining these measurements provides a quantitative picture of the transport mechanism and leads to the development of a physics-based model which predicts the transient convection based only on the properties of the large-scale structure present.

2.4 Experimental Measurements

In this experiment, vortex rings (Shariff and Leonard 1992) were generated in water using a pneumatically actuated vortex ring generator and allowed to collide normally with an instrumented heated surface. The experiment was repeated for a range of vortex rings of varying strengths and speeds. A vortex ring was chosen for a number of reasons including the ease in which it can be created and controlled and the fact that its production can be totally independent of the boundary layer flow near the surface. This allows a vortex to be generated which has similar characteristics to those observed in stagnating flows. Measurements are made to resolve the flowfield near the surface along with the convection from the surface. TRDPIV was used to measure the spatiotemporal characteristics of the propagating ring prior to and during its collision with the surface. A vortex identification scheme was then employed to identify and track the vortices present in the TRDPIV data. Measurements of the convective heat transfer coefficient were made using the newly developed Time-Resolved Heat and Temperature Array (THeTA)(Hubble and Diller 2010). Convection measurements were taken at 10 points along a line which bisected the vortex ring. The following gives a detailed account of the specific equipment used to make the required measurements.

The experiments were conducted in the AEThER laboratory at Virginia Tech. The equipment used in the experiment includes: a vortex ring generator, an instrumented heated plate, the accompanying data

acquisition systems, and a TRDPIV system. A schematic of the overall setup is shown in Fig. 2.1. Note that the vortex ring generator is positioned normal to the flat plate. The height of the TRDPIV laser plane is such that it bisects the vortex ring generator's nozzle and aligns with the heat flux sensors on the heated plate.

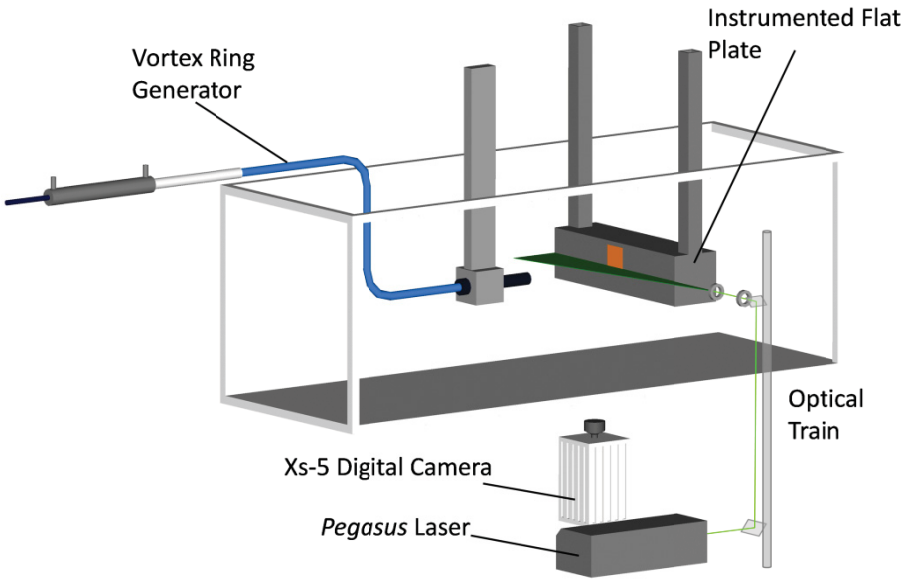

Fig. 2.1 Water tunnel facility and experimental setup

2.4.1 Vortex Ring Generator.

Vortex rings were produced in a conventional way (Shariff and Leonard 1992) by ejecting a slug of fluid through a circular, constant diameter nozzle. The vortex ring generator is shown schematically in Fig. 2.2. A pneumatic cylinder is attached to a regulated air supply via a solenoid valve (MAC 224B). Prior to a test, the piston is withdrawn a prescribed distance corresponding to the desired piston stroke length. When the valve opens, air forces the piston to move the prescribed distance to a stop and in doing so displaces a volume of water. The displaced water travels through the hydraulic hose where it displaces the slave piston located inside the nozzle. Movement of the slave piston displaces the fluid in the nozzle which forms the vortex ring.

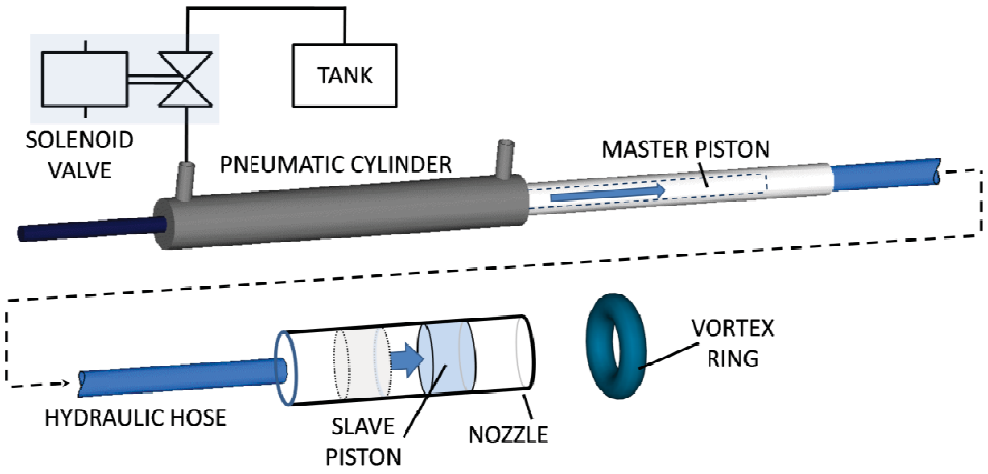

Fig. 2.2 Schematic of vortex ring generator

The nozzle was manufactured from a clear acrylic tube with an inside diameter of 2.54cm. The transparency of the tube allowed the velocity history as well as the stroke length of the slave piston to be measured optically using a high speed digital camera and standard shadowgraph techniques. Varying these parameters allowed the properties of the generated ring to be varied.

2.4.2 Instrumented Flat Plate

A basic flat plate model was constructed as shown in Fig. 2.1 and Fig. 2.3. The model is comprised of a smooth, removable face plate mounted to a water-tight rectangular housing. Two long square tubes are used to hold the model rigidly and double as conduits to carry power and signal wires out of the water tunnel. A 10cm square in the center of the 5mm thick removable face plate was thermally isolated from the rest of the plate by a series of machined channels. These channels were later filled with a low conductivity silicone adhesive both to keep the model water tight as well as to keep the face plate smooth. A thin-film resistance heater was mounted to the backside (inside) of the face plate and was used to heat the test area approximately 30 degrees above the water temperature. Insulation was used on the backside of the heater to force most of the heat through the face plate.

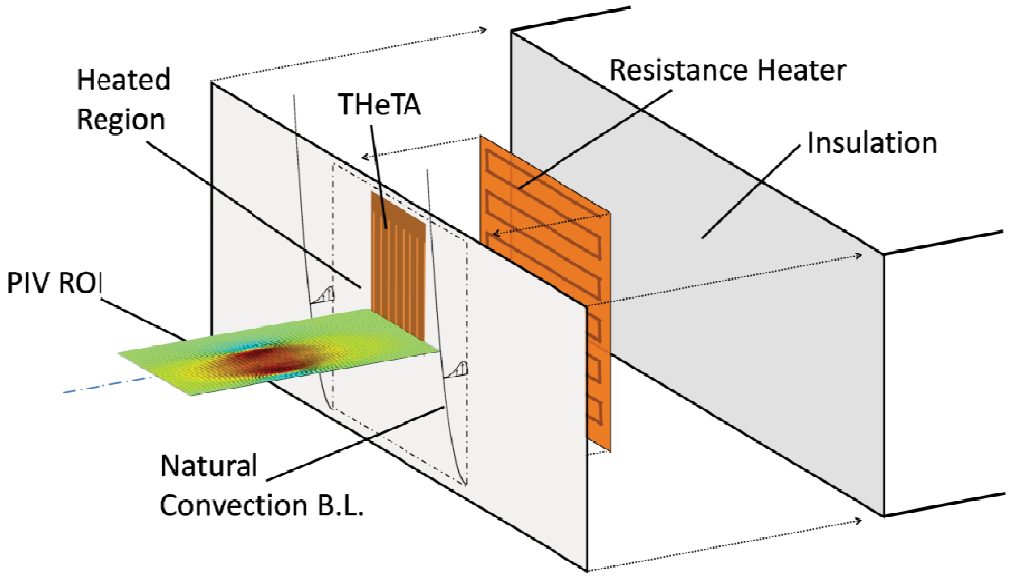

Fig. 2.3 Flat plate model and instrumentation

Heat flux and surface temperature measurements were taken at ten locations along the centerline of the test area at a spacing of 6.3mm using the Time-Resolved Heat and Temperature Array (THeTA). Details of the development and calibration of this sensor are given in (Hubble and Diller 2010) and a depiction of the sensor is given in Fig. 2.4. Heat flux through the sensor is proportional to the temperature drop across the thermal barrier (Kapton® 100HN) as measured by two type-T (copper-constantan) thermocouples connected in series (ΔV_1). Surface temperature measurements are obtained from the thermocouple located on the top of the THeTA (ΔV_2). The average sensitivity of the heat flux sensors on the THeTA is 223 uV/(W/cm^2) with a 95% time response of 509 ms. It was determined that this time response was not fast enough to capture the transient heat fluxes encountered in the present work. Therefore, the Hybrid Heat Flux (HHF)(Hubble and Diller 2010) technique was used to increase the time response of the THeTA. The HHF method increases the performance of differential heat flux sensors by accounting for the thermal energy stored within the sensor in conjunction with the heat flowing through the sensor. Utilizing the HHF method improved the 95% time response of the THeTA to 36 ms.

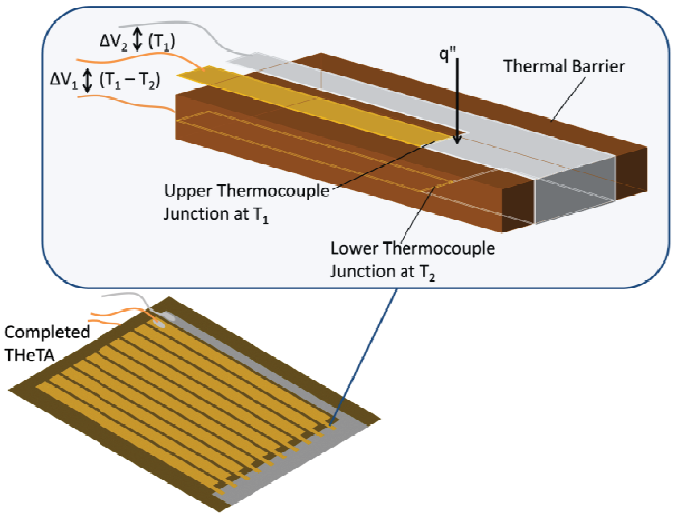

Fig. 2.4 The time-resolved heat and temperature array (TheTA). Provides a measure of both heat flux and surface temperature at 10 locations.

The 20 signals from the THeTA (10 heat flux, 10 surface temperatures) were sampled at a rate of 1 kHz using a National Instruments 6225 16bit DAQ which also synchronized the vortex ring generator and the TRDPIV camera and laser. An additional thermocouple was used to monitor the heater core temperature. The microvolt signals from the THeTA were first amplified using custom fabricated amplifier boards (Ewing 2006) with a fixed gain of 1000 and 480 Hz anti-aliasing filters. Post-processing of the signals from the THeTA was accomplished in Matlab. Applying the HHF method resulted in ten time resolved heat flux measurements with an estimated uncertainty of 7%. These heat flux measurements were then divided by the time-resolved temperature difference between the sensor surface and the water to obtain the time-resolved heat transfer coefficient.

$$h(t) = \frac{q"(t)}{T_S(t) - T_\infty} \qquad \textbf{2.1}$$

2.4.3 Flow Measurements: Time-Resolved Particle Image Velocimetry

The present study examines the full two-dimensional velocity field in front of the model using TRDPIV which delivers non-invasive, full-flow-field measurements with high spatiotemporal resolution. Details on the general method can be found in references (Westerweel 1997; Raffel, Willert et al. 2007).

As shown in Fig. 2.1 the TRDPIV system used employs a New Wave Research *Pegasus* dual head laser. An optical train is used to focus the laser light into a thin (≈1 mm) sheet which illuminates the fluid

plane containing the region of interest (ROI), located directly in front of the ten sensors. Neutrally buoyant glass microspheres with a mean diameter of 11 microns were used as tracer particles in the flow. Motion of the particles was tracked from underneath with an IDT XS-5 high-speed camera using its maximum resolution of 1280 x 1024 pixels. With a magnification of 51 um/pixel, the camera interrogated a ROI 6.5cm wide (along the plate) by 5.2cm long (normal to the plate).

The TRDPIV measurements were taken in a double-pulsed fashion for approximately 6.5 s at a sampling rate of 250 Hz. Due to the large range of velocities encountered throughout the range of vortex rings, no single pulse separation could be used across the entire set of experiments. Therefore, for each different vortex ring produced, preliminary testing was performed to determine the optimal pulse separation to obtain the desired particle displacements. This ranged from 2ms for the slowest rings to 0.5ms for the fastest. The images were processed using in-house developed (Eckstein and Vlachos 2009) TRDPIV software. Images were processed using a standard cross correlation with a 64 x 64 pixel window followed by a 32 x 32 window using the robust phase correlation after a discrete window offset. Using 8 by 8 pixel vector spacing, the ROI contained 19,625 vectors with 416 microns between vectors. The total uncertainty in TRDPIV velocity measurements using the aforementioned experimental setup and image-processing techniques is estimated to be +/- 10% (Eckstein and Vlachos 2009).

2.4.4 Vortex identification and circulation calculation

Starting with the TRDPIV measured velocity vector fields, a coherent structure identification scheme was employed to dynamically identify the vortices present in the ROI. In this study, the swirling strength (or λ_{ci}) method of Zhou et al. (Zhou, Adrian et al. 1999) is employed. Similar to the Delta criterion (Chong, Perry et al. 1990), the λ_{ci} method identifies vortices by regions where the velocity gradient tensor (∇u) has complex eigenvalues, indicating swirling flow. In the λ_{ci} method, the imaginary part of the complex eigenvalue of ∇u is used to identify vortices as it is a measure of the swirling strength of the vortex. To obtain the eigenvalues, the velocity gradient tensor's characteristic equation is solved:

$$\lambda^3 + P\lambda^2 + Q\lambda + R = 0 \qquad \textbf{2.2}$$

where P, Q, and R are the three invariants of ∇u . The imaginary part of the complex eigenvalue then gives the swirling strength at the location in the flow for which ∇u is calculated. While in theory any non-zero value for λ_{ci} indicates the presence of a vortex, the authors (Zhou, Adrian et al. 1999) suggest setting some positive threshold a few percent of the maximum value. By doing so, the identification of

extraordinarily weak structures is minimized. Therefore, in the present work, any location where λ_{ci} is greater than 2% of the maximum value for the flow field is identified as a point within a vortex.

After identifying the vortical structures, the circulation of the vortex was calculated. Circulation is defined as the line integral around a closed curve of the velocity (Panton 2005):

$$\Gamma = \oint_C \vec{V} \cdot \vec{dl} \qquad \textbf{2.3}$$

Equation 2.3 is applied to the TRDPIV measured velocity field around the regions that were identified as vortices. Circulation values ranging from 24 to 80 cm^2/s were calculated prior to the rings impacting the plate. These calculations compare well with Pullin's (Pullin 1979) predictions:

$$\Gamma \approx 1.41\left(L/D\right)^{-2/3} \int \frac{1}{2} U_p^2\left(t\right) dt \qquad \textbf{2.4}$$

where L/D is the non-dimensional piston stroke length and U_p is the piston velocity time-history. Measured circulation values correspond to Reynolds numbers (Γ/ν) ranging from 3000 to 10,000. In all cases, the vortex ring was laminar when it reached the plate.

2.4.5 Steady properties of the heated surface

Properties of the natural convection boundary layer were determined prior to the ring interaction. Both the fluid and thermal properties of the steady-state boundary layer were measured.

TRDPIV was used to measure the profile of the natural convection boundary layer. This test was performed using the TRDPIV setup described above except the laser plane was aligned vertically from below the tunnel and the camera was mounted horizontally. Also, the magnification was increased to 30 um/pixel to resolve the near wall flow field within the boundary layer. To check self similarity, dimensionless velocity was plotted versus a dimensionless coordinate η involving the Grashof number G_x. The dimensionless velocity is defined as

$$f'\left(\eta\right) = \frac{ux}{2\nu} G_x^{-1/2} \qquad \textbf{2.5}$$

and the dimensionless coordinate and Grashof number are defined as

$$\eta = \frac{y}{x}\left(\frac{G_x}{4}\right)^{1/4} \quad , \quad G_x = \frac{g\beta x^3\left(T_s - T_\infty\right)}{\nu^2} \qquad \textbf{2.6}$$

where ν and β are the kinematic viscosity and thermal expansion coefficient of water, g is the gravitational constant. The variables x and y are the coordinates parallel and normal to the plate respectively and u is the velocity parallel to the plate. Fig. 2.5 shows the wall jet profiles for multiple locations up the plate. A good collapse is observed and is in good agreement with the classic work by Ostrach (Ostrach 1953).

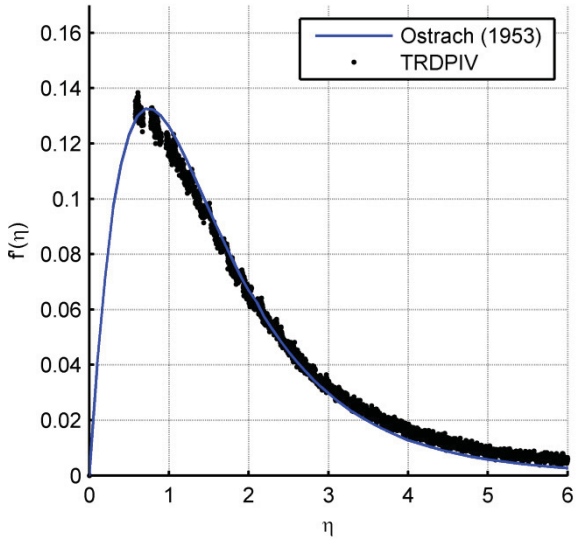

Fig. 2.5 Non-dimensional boundary layer profile shown with standard scaling

The thermal state of the natural convection boundary layer was also examined using the heat flux and surface temperature measurements. Equation 2.7 predicts the heat transfer coefficient at a point on the plate a distance x from the bottom (Incropera and DeWitt 2002)

$$h = \frac{k}{x}\left(\frac{G_x}{4}\right)^{1/4} \frac{.75\,\mathrm{Pr}^{1/2}}{\left(0.609+1.221\,\mathrm{Pr}^{1/2}+1.238\,\mathrm{Pr}\right)^{1/4}} \qquad \textbf{2.7}$$

where k and Pr are the thermal conductivity and Prandlt number of water evaluated at the film temperature. Plugging in the appropriate values, Eq. 2.7 predicts the heat transfer coefficient at the sensor location to be 543W/m^{2}K. The average value measured by the THeTA was 520±38 W/m^{2}K (95%) which is about 5% below the value predicted by Eq. 2.7 but within the experimental uncertainty.

2.5 Ring impingement and resulting heat transfer.

Representative results from the analysis of the planar TRDPIV measurements with the combined heat-transfer are shown in Fig. 2.6. On the left, velocity fields are shown at six evenly spaced time steps

over a half second with the contour representing the vorticity normalized by the ratio of the maximum piston velocity to orifice diameter ($\omega^*=\omega/[Up_{max}/D]$).. The velocity fields show one half of the vortex ring (the bottom axis coincides with the ring's axis of symmetry). The five markers on the right side of the vector fields indicate the location of five heat flux sensors. The plot at right shows the measured transient Stanton number (dimensionless convective heat transfer coefficient) at the five sensor locations normalized by the free convection value, St_o . Here, the Stanton number is defined as:

$$St = \frac{h}{\rho C U_V} \qquad \textbf{2.8}$$

where ρ and *C* are the density and specific heat of water and *U* is the measured self-induced propagation velocity of the vortex ring when it first enters the TRDPIV field of view.

As the vortex ring approaches the heated plate its propagation velocity decreases and its radius increases as it stretches (Walker, Smith et al. 1987). In Fig. 2.6, this is observed as the vortex moving upward, away from its axis of symmetry (the other half of the ring travels downwards, not shown). As the vortex reaches the plate, vorticity of opposite sign is generated in the boundary layer at the surface. At approximately t=0.55s, an eruption (Doligalski, Smith et al. 1994) occurs and the vorticity forms a secondary vortex outboard of the primary. The formation of the secondary vortex causes a rapid decrease in the radial growth of the primary ring. Consequently, the primary vortex never moves farther up the plate than where it is at t=0.75s and never passes the top sensor. The observed behavior of the vortex ring is in qualitative agreement with the work of Walker et al.(Walker, Smith et al. 1987).

As the vortex-ring interacts with the heated plate, the convective heat transfer increases dramatically compared to the unperturbed natural convection level. To highlight the heat-transfer augmentation caused by the vortex interaction, the gray-shaded area represents the increase between the measured Stanton number and the levels corresponding to natural convection. Note that when the vortex is in close proximity to the sensor, in some instances the convective transport increases by more than a factor of four over the free convection levels. This is in stark contrast to the value of 15% reported from spatially averaged measurements (Arevalo, Hernandez et al. 2007) and illustrates that the vortex has a very localized but dominant impact on the convection.

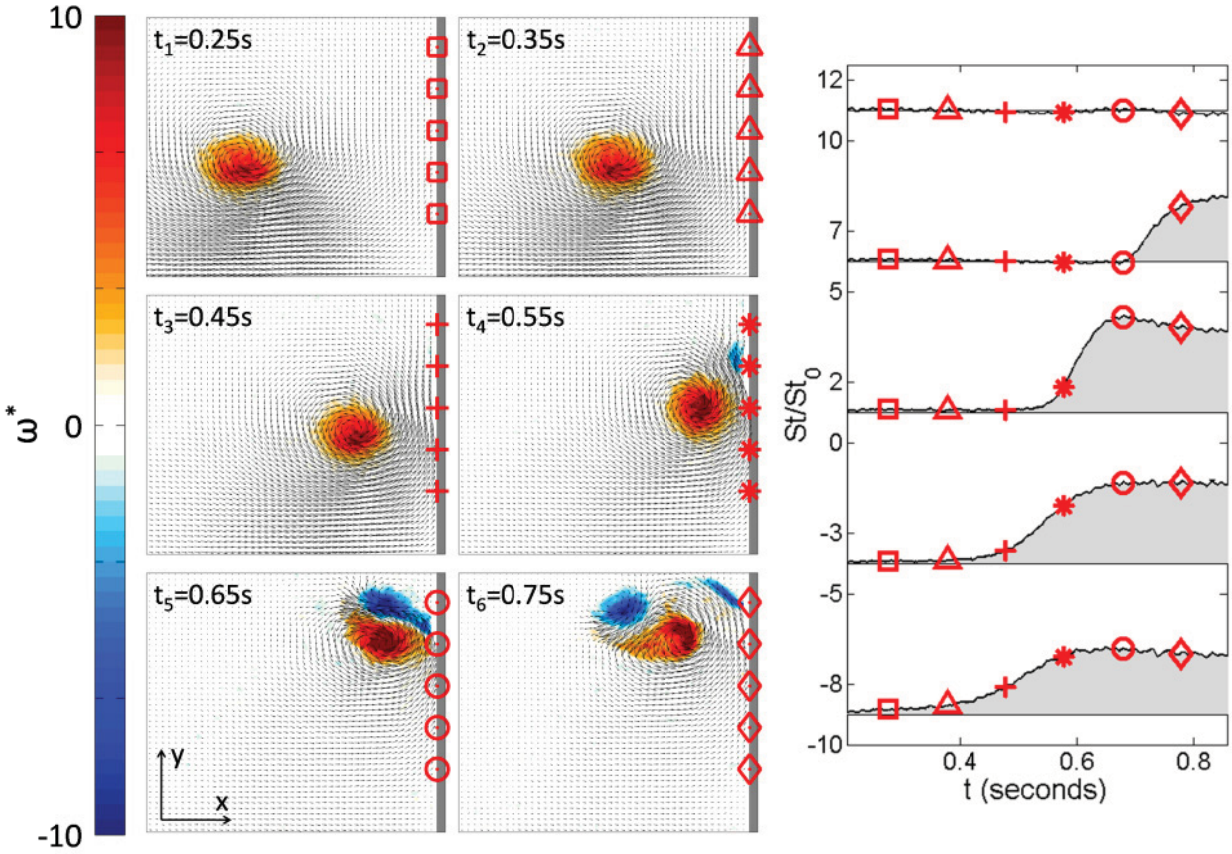

Fig. 2.6 Illustration of ring impingement and heat transfer. Velocity fields sequence at left represent one half of the vortex ring over a one half second period. As the ring approaches the heated plate the measured convection increases as illustrated at right. Markers in the velocity fields correspond to individual heat flux sensor locations and indicate the timing at right.

Fig. 2.7 illustrates the spatial convection distribution caused by a single vortex. Here, the flow field in the vicinity of a vortex is shown with the instantaneous convection from five nearby sensors. Since the vortex is rotating counterclockwise, the two sensors above the vortex are in the upwash region where the vortex is pulling fluid away from the surface. These two sensors indicate that the convection at this point in time is essentially the natural convection level. The two sensors below the vortex are in a strong downwash region and experience a significant increase in convection. Notably, the sensor directly beneath the vortex is experiencing significantly less increase in convection compared to the sensors in the downwash region. Even though it is much closer to the vortex, it experiences less convection. These results indicate that fluid traveling towards the sensor has a much larger affect compared to fluid sweeping along the sensor parallel to the surface. These are important observations to consider as an analytical model is developed.

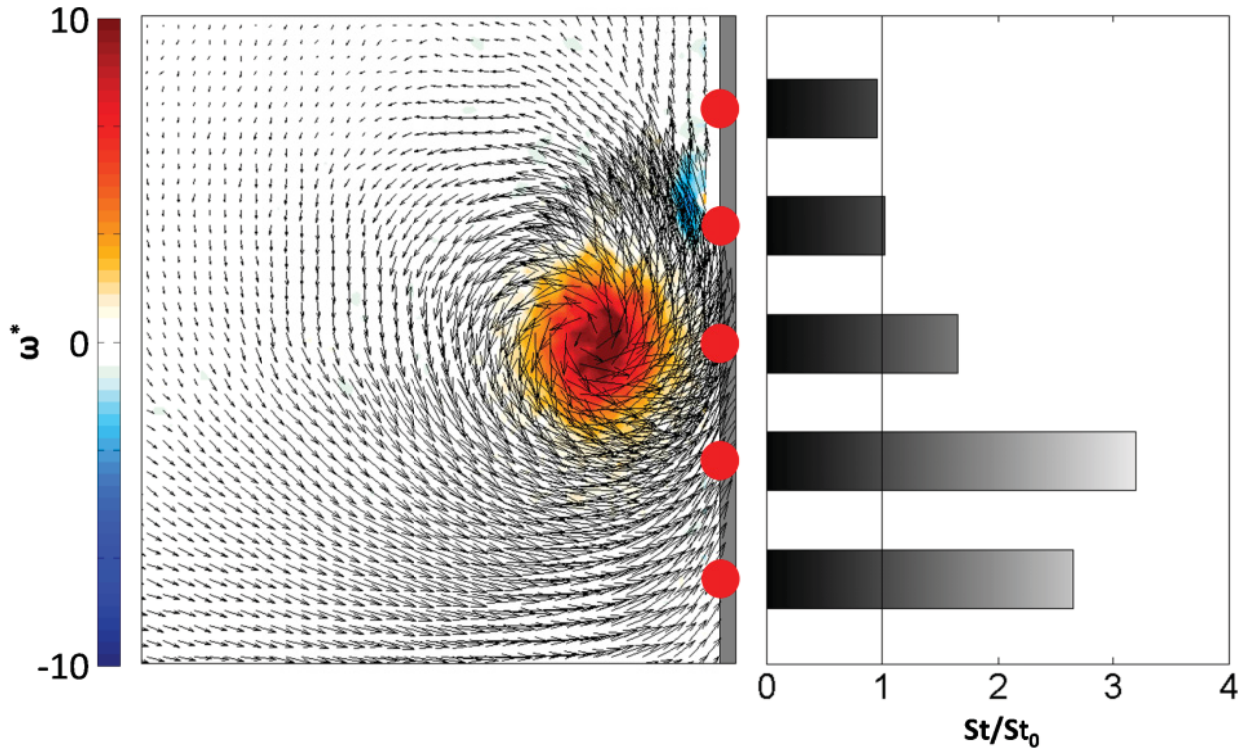

Fig. 2.7 Close up of interaction process and measured rate of convection. The sensors in the downwash region of the vortex experience more convection than the sensor directly beneath the vortex and much more convection compared to sensors in the upwash region.

2.6 A Mechanistic Model

The current effort to develop a physically based model to predict the convective transport due to a vortex is based on the surface renewal model of Nix et al. (Nix, Diller et al. 2007). In their work, it was hypothesized that when a flow structure penetrates through the boundary layer, interaction with the surface causes an increase (augmentation) in the rate of heat transfer over that due to transport through the laminar boundary layer. This process was modeled as a purely conductive event treating the fluid structure as a semi-infinite medium. Heat is conducted to the structure for a characteristic time τ.

$$\Delta h = \frac{\Delta q}{T_\infty - T_S} = \frac{k}{\sqrt{\pi \alpha \tau}} \qquad \textbf{2.9}$$

By defining the time scale as the ratio of the mean stream-wise integral length scale to stream-wise R.M.S fluctuating velocity, this model successfully predicted experimentally measured values of increases in the time-averaged heat transfer coefficient (Nix, Diller et al. 2007).

2.6.1 A time-resolved model

Using the surface renewal model described above, a simple model is developed which captures the time-dependent physics of the vortex-surface interaction. Consider the case of a single vortex located near a heated surface with a thermal boundary layer of thickness δ_T as shown in Fig. 2.8. The vortex induces a velocity field according to the Biot-Savart law (Panton 2005) which forces outer fluid through the boundary layer. This process can be thought of as individual fluid elements which start at the outer fluid temperature (T_∞), move through the thermal boundary layer, and interact with the surface. Within the boundary layer, mixing with the warmer near-wall fluid occurs and causes the temperature to increase. Thermal energy, therefore, is being transferred to the entrained fluid prior to its reaching the plate. Once the entrained fluid reaches the surface, the resulting conduction is diminished because of the amount of thermal energy that has already been transferred to it. Thus, the characteristic time scale governing the heat transfer is the time required for the convected fluid elements to travel from the edge of the thermal boundary layer to the heated surface.

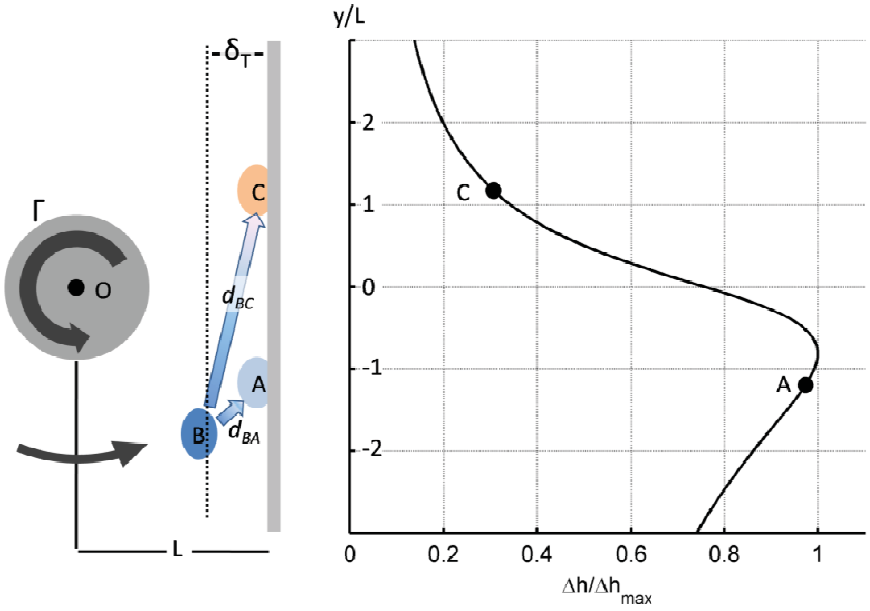

Fig. 2.8 Schematic used in model development along with functional model results. Model predicts much larger convection in the downwash region compared to the upwash region due to the shorter value of d_{BA} compared to d_{BC}.

The characteristic time is dependent on two factors: the distance that the vortex travels within the boundary layer to reach the surface (*d*) and the average induced velocity along this distance. Both of these values are estimated from the velocity field produced by a free vortex of specified strength at the identified location. The average induced velocity is approximated assuming a linear drop to zero at the

surface and is therefore one half the induced velocity at the edge of the boundary layer (point **B**) calculated from the Biot-Savart law. For point **A**, this is:

$$\overline{V}(t) = \frac{1}{2} V_{IND}(t) = \frac{1}{2} \frac{\Gamma(t)}{2\pi d_{OB}(t)} \quad \textbf{2.10}$$

The characteristic time for point **A** is then:

$$\tau(t) = \frac{d_{BA}(t)}{\overline{V}(t)} \quad \textbf{2.11}$$

While the model described above is very simple, the change in d_{BA} allows it to capture the upwash versus the downwash effect as shown in Fig. 2.7. This is illustrated in Fig. 2.8 by plotting the model prediction as a function of non-dimensional vortex location (y/L). Note that while points **A** and **C** are equidistant from the vortex center, point **A** experiences much more convection because $d_{BA}<d_{BC}$. This curve is similar in shape to the experimentally obtained curve shown in Fig. 2.7.

It is expected that a vortex will not have an immediate effect on the surface convection. Therefore, it is necessary to incorporate a time delay to account for the time required for the induced outer fluid to reach the surface. The appropriate time scale is the ratio of the thermal boundary layer thickness (δ_T)to the average induced velocity (Eq. 2.10). Physically, this represents the shortest time that it would take the outer fluid to cross the thermal boundary layer.

$$\tau_{Delay}(t) = \frac{\delta_T}{\overline{V}(t)} \quad \textbf{2.12}$$

Due to the square root in the denominator of the time-averaged augmentation model (Eq. 2), the instantaneous model has a factor of two in the denominator relative to the time-average result in Eq. 2 from the integration. Incorporating the time delay and the factor of two, the heat transfer coefficient augmentation prediction at point **A** becomes:

$$\Delta h\left(t + \tau_{Delay}(t)\right) = \frac{k}{2\sqrt{\pi\alpha\tau(t)}} \quad \textbf{2.13}$$

Adding this augmentation to the heat transfer coefficient of the undisturbed boundary layer as the square root of the sum of the squares gives:

$$h\left(t+\tau_{Delay}\right)=\sqrt{h_0{}^2+\Delta h\left(t+\tau_{Delay}\right)^2} \quad \textbf{2.14}$$

as the total magnitude as a function of time. This always results in an increase shifted in time for the total heat transfer coefficient.

2.7 Comparison of the analytical model and experimental results

The analytical model was used to predict the transient convective heat transfer coefficient at the heat flux sensor locations using the properties of the vortices identified in the TRDPIV measurements. In all, 33 comparisons were performed. The following section along with Fig. 2.9 through Fig. 2.11 gives a detailed description of the interaction process for the same sensor location for tests with vortex Reynolds numbers of Re_Γ=3100, 5800, and 9200. For comparison, the tests labeled Re_Γ=5800 in the following three figures examines the flow field and the convection at the fourth heat flux sensor from the top for the test shown in Fig. 2.6. Fig. 2.12 then summarizes the results for all the tests.

The measured transient circulation and the induced velocity at a single sensor location are shown in Fig. 2.9 for three vortex strengths spanning the range of test conditions. As the vortex ring propagates towards the plate, the circulation remains nearly constant. Then, upon reaching the plate, vorticity of opposite sign is generated at the wall and the vortex strength quickly diminishes. This is seen as the abrupt drop in circulation at t=0.275s, t=0.655s, and t=1.39s for the three tests shown. The different times are due to the smaller self induced propagation velocity for the weaker vortex rings (it takes longer for them to propagate from the edge of the TRDPIV ROI to the plate). Incorporating these measured vortex circulations with the measured vortex position, the transient induced velocity at a sensor on the plate's surface was calculated for each test using the Biot-Savart law as shown in Fig. 4.b. Since in each test the vortex follows approximately the same trajectory, the two main differences are the speed at which the vortex passes the sensor and the induced velocity at the sensor, both of which are affected by the circulation value. Consequently, the strongest vortex with the largest Re_Γ causes the largest induced velocity for a short period of time while the weakest vortex causes a smaller induced velocity for a longer period of time.

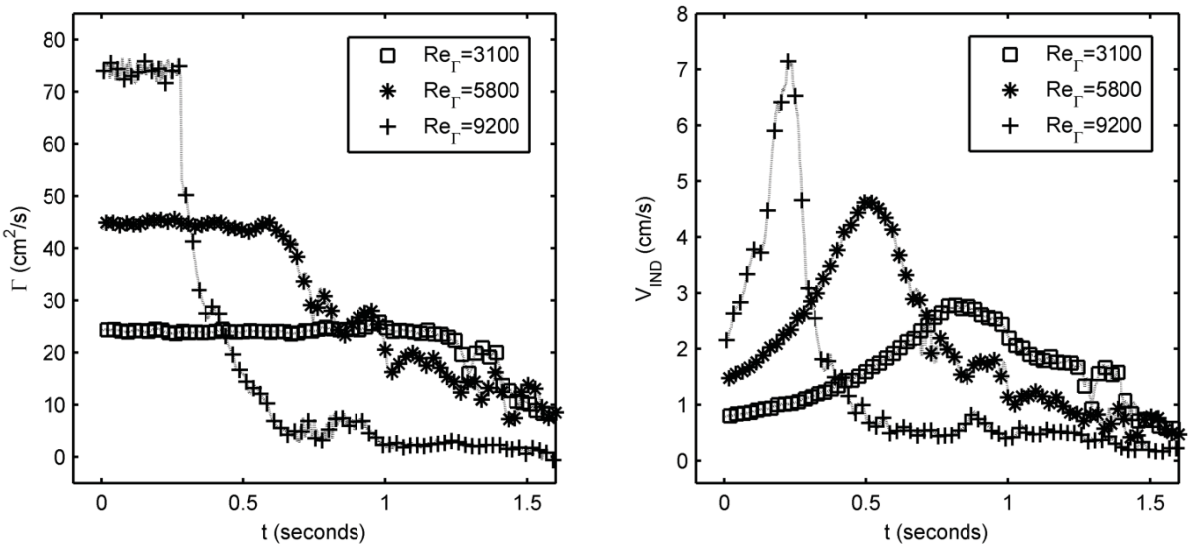

Fig. 2.9 Measured circulation of vortex as it approaches the plate for three different tests. The circulation is used to calculate the induced velocity at the sensor location on the plate using the Biot-Savart law

The characteristic time used in the model is a function of the induced velocity and the distance that the fluid travels within the thermal boundary layer (d_{BA}). Fig. 2.10 shows d_{BA} as a function of time for the Re_Γ=5800 test. Curves for the other tests are not shown due to their similarity to those shown in Fig. 2.10. Specifically, the curves for d_{BA} are essentially identical in magnitude and are only contracted or expanded in time. The characteristic time curve is smaller in magnitude for the stronger vortices and larger for the weaker vortices. It is helpful to again examine Fig. 2.6 as d_{BA} is calculated for the fourth sensor from the top for this test. At the beginning of the test, the vortex is slightly above the sensor. Therefore, the Biot-Savart law predicts that fluid impacting the sensor would travel through the thermal boundary layer at a shallow angle from beneath. Therefore, the predicted distance is more than three times the thermal boundary layer thickness. As the vortex moves closer to and more above the sensor, the sensor transitions to being in a downwash region and the distance approaches the minimum possible value of δ_T which implies that the fluid is essentially passing straight through the boundary layer, normal to the surface. The characteristic time (τ) was then calculated by combining the curve for d_{BA} with the induced velocity to produce the curve shown in Fig. 2.10. The time decreases as d_{BA} decreases but then begins to increase at the end as the induced velocity (and circulation) decrease.

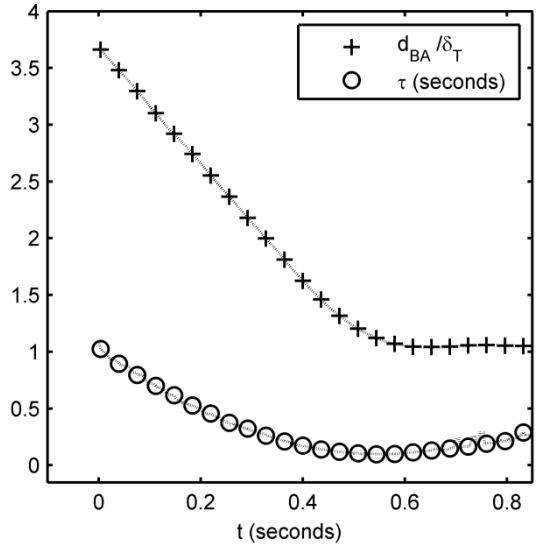

Fig. 2.10 The distance that fluid must travel within the thermal boundary layer (d_{BA}, +) is calculated from the measured vortex location. Combing this value with the induced velocity from above yields the characteristic time (τ, O) used in the model. Re_Γ=5800

The characteristic time (τ) and the time delay (τ_{Delay}) were calculated for each sensor location for each test. Plugging these values into Eqs. 2.13 and 2.14 yields a prediction of the convection as a function of time at that point. Fig. 2.11 shows a comparison of the measured and predicted convection at a single sensor location for three tests spanning the range of vortex strengths tested. The gap in the prediction at t=0 for each test represents the initial calculated time delay, τ_{Delay}. For all t<0, the vortex has not yet entered the TRDPIV ROI and the prediction is therefore the natural convection (undisturbed) Stanton number. At t=0, the vortex first enters the ROI, the model is applied and combined with the natural convection Stanton number and delayed as specified. Then, as the vortex approaches the plate, the induced velocity increases and d_{BA} decreases causing a shorter and shorter characteristic time which in turn causes the predicted convection to increase. Physically, the entrained fluid is spending less and less time within the thermal boundary layer and is removing heat more effectively upon impact with the surface. Comparing the transient model prediction with the measured convection, the two match well in both shape and magnitude. Particularly, predictions at the point of highest augmentation are the most accurate in terms of both magnitude and timing.

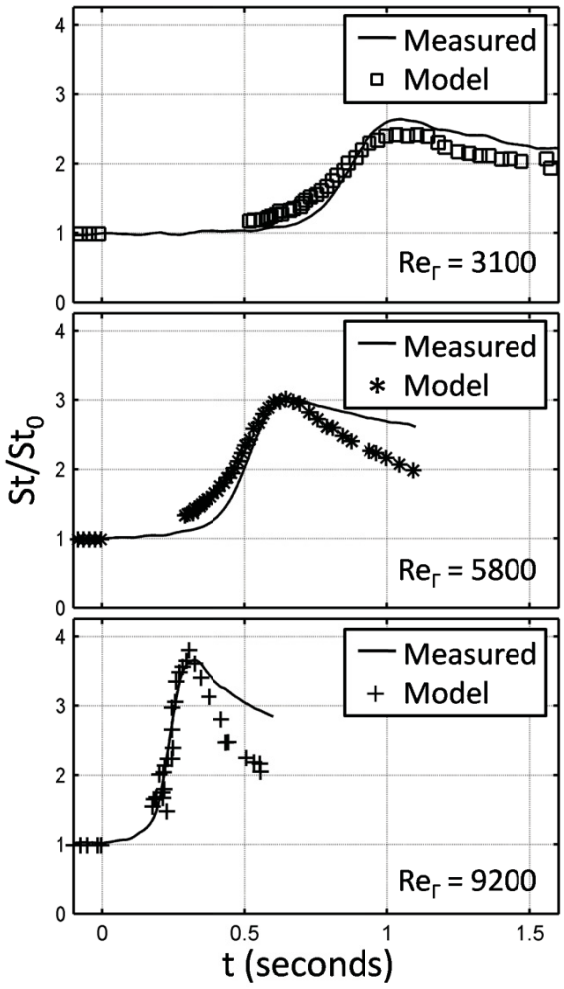

Fig. 2.11 Comparison of model prediction to measured convection during vortex interaction. Results shown from three representative tests spanning the range of vortex strengths.

Similar results were observed for all of the 33 vortex ring tests examined spanning 5 different test conditions and 5 sensor positions. All of the heat flux curves were similar to those in Fig. 2.11. To characterize the results, the maximum values of the measured and modeled Stanton numbers are shown in Fig. 2.12. In over 80% of the cases the model predicts the measured convection within 15% as indicated by the dotted lines. As the vortex strength increases, the induced velocity increases which causes a smaller characteristic time and smaller time delay in the model. This directly increases the augmented heat transfer coefficient predicted by equation 6.

The model's promising results clearly demonstrate that coherent structures increase convection by pushing outer fluid through the boundary layer which then conducts heat from the surface. The simplicity of the model and the ease in which it can be implemented make the results all the more

encouraging. The ultimate application is to model vortices in turbulence which would increase our fundamental understanding of the effects of turbulence on surface transport. It is in this direction that current efforts are ongoing.

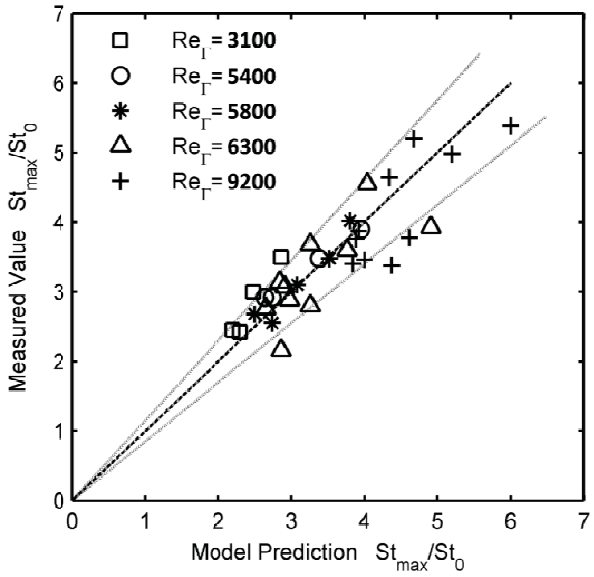

Fig. 2.12 Comparison of the maximum measured convection with maximum model prediction for the range of test conditions. The dotted lines represent the +-15% bounds.

2.8 Conclusions

In this investigation, the convective heat transfer resulting from the interaction of a ring vortex with a surface was studied experimentally using spatiotemporally resolved flow and surface convection measurements. This interaction had not been previously studied in detail which is surprising considering it is a fundamental problem of both convective fluid mechanics and turbulence. The results indicate that the convection from this coherent structure interaction is due to transient heat conduction between the structure and the surface. Based on an analysis of the time-dependent flow and surface heat flux, a mechanistic model was developed using the parameters of the vortices to calculate the characteristic times for the fluid motion through the boundary layer. In regions where vortices force fluid directly through the boundary layer, the convection is high because the fluid quickly reaches the surface. Conversely, regions where fluid is swept along the surface experience less convection because the fluid has already been heated within the boundary layer prior to reaching the surface. The time-resolved heat flux was calculated using this simple model and compared to the measured convection at multiple surface locations for a range of vortex speeds and strengths. For the parameter space investigated, the

model was very accurate at predicting the time-resolved convection resulting from the coherent structure interaction. This transport mechanism has important implications for understanding the role of coherent structures in turbulent flows.

3 A Mechanistic Model of Turbulent Heat Transfer Augmentation in Stagnation Flow

David O. Hubble, Pavlos P. Vlachos, and Tom E. Diller

3.1 Abstract

A time-resolved experimental study has been performed examining the mechanism by which heat transfer is augmented in stagnating flows by freestream turbulence. Recent work has demonstrated that turbulence is amplified into strong vortices in the stagnation region which then dominate the near-wall flow. By utilizing time-resolved digital particle image velocimetry (TRDPIV) and a new variety of heat flux sensor called the time-resolved heat and temperature array (THeTA), the spatio-temporal influence of these structures on the heat transfer is examined. The current study confirms that coherent structures are the primary mechanism for the observed heat transfer augmentation in stagnating flows. It is shown that large increases in convection occur in regions where the structures force freestream fluid through the thermal boundary layer to the surface. Evidence supporting this mechanism is provided by the success of a simple mechanistic model which was recently developed by the authors. The model is able to accurately predict the time-resolved convection at any point on the surface based solely on the transient properties of the large-scale structures present.

3.2 Nomenclature

a	=	acceleration parameter (1/s)
α	=	thermal diffusivity (m^2/s)
b	=	grid bar diameter (cm)
β	=	thermal expansion coefficient (1/K)
C	=	specific heat (J/kg K)
d	=	distance (m)
δ	=	boundary layer thickness (m)
Γ	=	circulation (m^2/s)
h	=	convective heat transfer coefficient (W/m^2 K)
k	=	thermal conductivity (W/m K)
L	=	stagnation body height (cm)
Λ	=	turbulence integral length scale (cm)
ν	=	kinematic viscosity (m^2/s)

Pr = Prandtl number

q" = heat flux (W/m^2)

ρ = density (kg/m^3)

St = Stanton Number

t = time (s)

T = temperature (K)

τ = time delay (s)

Tu = turbulence intensity (%)

U = velocity (m/s)

Subscripts

$_0$ = laminar baseline level

$_\infty$ = freestream

$_S$ = surface

$_T$ = thermal boundary layer

3.3 Introduction

Freestream turbulence has a major effect on surface heat transfer in many engineering applications, for example, gas turbines, combustors, electronic cooling devices, and heat exchangers. Modeling the surface heat transfer under such circumstances is difficult even for simple flows and geometries because of the unpredictable effect of the freestream turbulence. Traditionally, methods for analyzing the convective heat transfer when freestream turbulence exists rely on average and statistical properties of the flow field. The analysis results in empirical correlations which lack a physical foundation and ignore the time-dependent processes. Therefore, it comes as no surprise that no single correlation can capture all available experimental data. In order to understand and model the mechanism by which these processes occur it is necessary to study the detailed transient properties of the flow field in conjunction with the time-resolved heat transfer during the interaction.

In order to understand the effect of freestream turbulence on surface transport, it is important to characterize the coherent structures present and determine how they interact with the surface boundary layer. In a recent paper, large-scale coherent structures were shown to play a dominant role in turbulent flows (Adrian 2007). Experiments have also shown the existence of very-large-scale motions in the logarithmic region of turbulent boundary layers which can reach up to 20 times the boundary layer

thickness in size (Hutchins and Marusic 2007). These coherent structures have been identified to be important contributors to transport in boundary layers. This is particularly true in stagnation regions where structures are amplified into strong vortices at the surface by the mean flow strain rate (Sutera 1965; Blackwelder 1988; Wei and Miau 1992). Heat and mass transport at the wall appear to be directly affected by the sweeping of these large vortices into the boundary layer, particularly at higher levels of turbulence intensity (Thole and Bogard 1995; Mosyak, Pogrebnyak et al. 2001). VanFossen and Simoneau (Vanfossen and Simoneau 1987) used wires to create large vortices perpendicular to a downstream cylinder and studied the resulting fluid flow and heat transfer near the surface using a combination of smoke visualization and liquid crystals. Regions where vortices forced fluid toward the surface (downwash) corresponded to regions of increased heat transfer. Measurements of the fluctuating transport at the surface have shown direct correlation with the velocity fluctuations in the freestream (Simmons, Hager et al. 1990; Moss and Oldfield 1996; Holmberg and Diller 2005) but the impact on the overall transport was not established.

Marusic et al. (Marusic, Mathis et al. 2010) recently developed a model based on fluid experiments which predicted the near-wall turbulence given only large-scale information from the outer boundary layer region. The success of their model showed that the small scale structure was directly influenced by the large scale outer structures. In a similar fashion, the authors (chapter 2 of this dissertation) developed a time-resolved model to predict the convection resulting from the interaction of a single vortex with a surface. The model was tested experimentally by comparing its prediction to the measured convection during the collision of a vortex ring with a wall. Results indicated that the model performed quite well. In the following section the model is briefly described.

In the current work, heat transfer augmentation in a stagnating turbulent flow is examined experimentally. During the test, the spatiotemporally resolved convective heat transfer coefficient along the stagnation line is examined in conjunction with the fully resolved two-dimensional flow field. Combining these measurements gives a quantitative picture of the transport mechanism and provides valuable insight into the physics of the interaction. Finally, the previously developed mechanistic model is applied to the current data and used to predict the transient convection from a more realistic flow field which contains multiple simultaneous vortices.

3.4 Mechanistic Model

A simple model of the mechanism of heat transfer augmentation by a coherent structure was recently developed based on experimental observations of a vortex ring collision with an instrumented heated plate. The model predicts the time-resolved increase in convection over laminar levels based only on the properties of the vortex present. Heat transfer to the structure is modeled as a purely conductive event treating the structure as a semi-infinite medium. The resulting convection is then a function of only a characteristic time-scale for the interaction and the properties of the fluid.

$$\Delta h = \frac{\Delta q}{T_\infty - T_S} = \frac{k}{\sqrt{\pi \alpha t}} \qquad \textbf{3.1}$$

Here, the characteristic time (*t*) can be thought of as a measure of how long a packet of fluid warms prior to reaching the surface. The more heat that is transferred to the fluid before reaching the surface, the less heat the fluid will be able to remove from the surface upon impact. By using the physical properties of the nearby vortex to calculate the characteristic time, the model was able to accurately predict the convection resulting from a vortex-wall interaction. The following paragraphs briefly describe the model inputs and how it is used to produce an overall convection estimate.

Fig. 3.1 is used to describe how the characteristic time can be calculated from vortex properties. A vortex is located at point **O** a distance *L* from a heated surface where a thermal boundary layer of thickness δ_T exists. The characteristic time is defined as the time required for freestream fluid to pass from the edge of the thermal boundary layer to the surface. To determine this time, both a distance and an average velocity are needed. By the Biot-Savart law, the vortex induces a velocity at a surface point **A** that is a function of the vortex circulation, Γ, and the distance from the vortex to the surface, d_{OA}. Since the Biot-Savart law also gives the trajectory of the fluid, it can be used to determine where, for a given surface location, the fluid crossed into the thermal boundary layer. The distance that fluid traveled within the boundary layer can then be determined from this information (d_{BA} for example). Assuming the velocity decreases linearly from the Biot-Savart prediction at **B** to zero at **A**, the characteristic time becomes:

$$t = \frac{d_{BA}}{\frac{1}{2} V_{IND}} = \frac{4\pi d_{OA} d_{BA}}{\Gamma} \qquad \textbf{3.2}$$

Note that the model automatically accounts for the difference between the upwash and downwash region of a vortex. While both **A** and **C** are equidistant from the vortex, **A** predicts higher augmentation (smaller *t*) because d_{BA} is much shorter than d_{BC}.

To complete the model it must be properly delayed and combined with the laminar baseline convection. The time scale that was chosen for the time delay and which worked well in the vortex ring experiment was the ratio of the thermal boundary layer thickness to the ½ V_{IND} value calculated above. Finally, the predicted augmentation (Eq. 3.1) is combined with the baseline level using the square root of the sum of the squares to produce a total convection prediction. In this case, the baseline level is the heat transfer coefficient when no freestream turbulence is present.

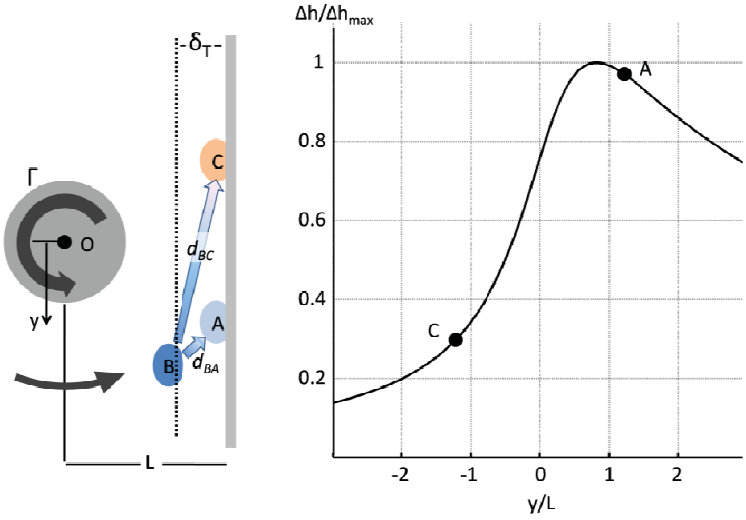

Fig. 3.1 Schematic used in model development with functional model results. Model predicts larger convection in the downwash region due to the shorter distance that fluid travels within thermal boundary layer.

In the original paper, the model was successfully used to predict the time-resolved convection from the collision of a vortex ring with a heated surface. In the current work, it is applied to the more complicated flow field of a stagnating turbulent flow. Here, the convection is strongly influenced by the multiple vortices of different sizes and strengths which exist together.

3.5 Experimental Methodology

The experiments for the data reported in this work examine the convection along the stagnation line of a bluff body in a flow which contains large-scale freestream turbulence. Time-Resolved Digital Particle Image Velocimetry (TRDPIV) (Raffel, Willert et al. 2007) was used to provide full-flow-field, time-resolved velocity measurements while the new Time-Resolved Heat and Temperature Array (THeTA) (Hubble and Diller 2010) was used to measure the convection from the heated stagnation model. All the

tests were performed in a water tunnel at a constant freestream velocity of 10cm/s. Passive bi-plane grids were used to control the freestream turbulence characteristics at the test location. Three grids were used producing 3 different freestream turbulence conditions. A total of eight tests were performed, two each at each turbulence condition including a low turbulence baseline with no grid present. A schematic depicting the relative positions of the equipment used in the experiment is shown in Fig. 3.2.

3.5.1 Water Tunnel Facility and Turbulence Generation

The water tunnel used in the current experiment is a closed loop, variable speed facility which was operated at 10cm/s for all tests. The test section measured 0.61m square by 1.77m long and is constructed from clear acrylic. At the tunnel speed used in the test, the freestream turbulence intensity is approximately 1% throughout the test section.

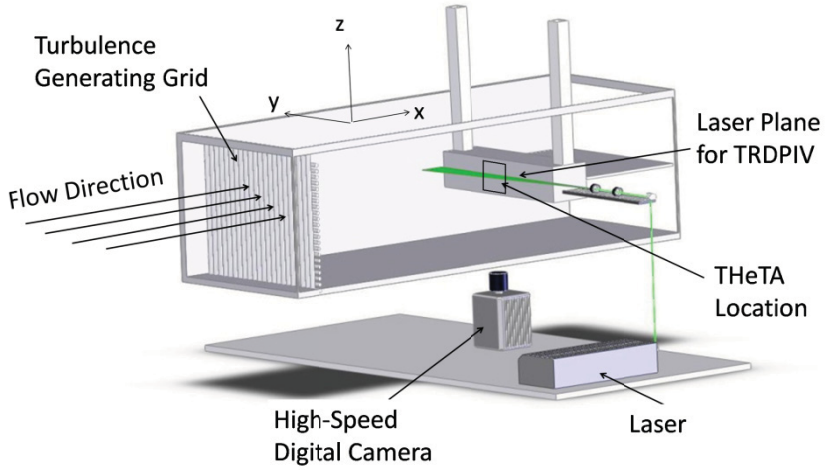

Fig. 3.2 Water tunnel facility and position of model relative to turbulence grid and TRDPIV system.

Freestream turbulence was generated using simple bi-plane grids. Grid bar sizing (b) and positioning was based on correlations by Baines and Peterson (Baines and Peterson 1951). Three grids were constructed with solidity ratios of 0.7 to give integral length scales of approximately 1, 2, and 3cm at a constant turbulence intensity of 7.1%. The properties of the generated turbulence were calculated from the measured flow field using the method described by Gifford (Gifford, Diller et al.). Details of the grid geometry and turbulence properties are given in Table 3.1.

Table 3.1 Details of grids and turbulence statistics

Grid	b (cm)	Tu (%)	Λ (cm)
1	0.66	7.4	0.81
2	1.6	7.2	1.93
3	2.16	6.9	3.24

3.5.2 Instrumented Flat Plate

The instrumented plate used in this experiment is identical to that used in chapter 2. Details of its design can be found in section 2.4.2.

3.5.3 Flow Measurements: Time-Resolved Particle Image Velocimetry

The TRDPIV measurements were performed using the same equipment and lenses used in chapter 2. The only difference was the timing used to control the laser and camera. Here, the TRDPIV measurements were taken in a single-pulsed fashion for approximately 13 seconds at a sampling rate of 250 Hz.

3.5.4 Vortex identification

The vortex identification scheme is identical to that described in section 2.4.4

3.6 Experimental Measurements

3.6.1 Laminar Baseline

Preliminary tests were performed with no grid installed in the tunnel to validate the experimental approach and provide baseline flow and heat transfer quantities for comparison with the turbulent cases. In stagnating flows, the most important parameter for both thermal and fluid analysis is the acceleration parameter, *a*. This parameter was measured using the TRDPIV vector field to be 0.98 (1/s) which compares well with the correlation given by White (White 1974) for a square body in cross flow, which relates *a* to the freestream velocity *U* and the body height *L*.

$$a \approx \frac{\pi}{2}\frac{U}{L} = 1.03 \qquad \textbf{3.3}$$

The excellent match between the predicted and measured acceleration parameter allows its confident use in the calculation of other properties including the laminar boundary layer and thermal boundary layer thickness.

$$\delta = 2.4\sqrt{\frac{\nu}{a}} \qquad \delta_T = \delta \,\mathrm{Pr}^{-0.4} \tag{3.4}$$

Using the kinematic viscosity (ν) and Prandtl number (Pr) at the film temperature gives δ=0.21 cm and δ_T=0.11cm. The acceleration parameter can also be used to predict the baseline heat transfer coefficient from the surface using the correlation given by Goldstein (Goldstein 1938).

$$h_0 = 0.5421k\,\mathrm{Pr}^{0.42}\sqrt{\frac{a}{\nu}} \tag{3.5}$$

Equation 3.5 predicts a baseline heat transfer coefficient of h_0=731 W/(m^{2}K) which matches the value of h_0=755 W/(m^{2}K) measured by the THeTA to within the experimentally uncertainty. The measured convective heat transfer coefficients are made into the dimensionless Stanton number by dividing by the product of the freestream velocity, specific heat, and density ($U_\infty C\rho$).

$$St(t) = \frac{h(t)}{\rho C U_\infty} \tag{3.6}$$

3.6.2 Transient Flow and Convection: Physical Insight of the Mechanism

As turbulence enters the stagnation region, it is stretched and amplified into vortices which interact with the near-wall fluid and cause large increases in the instantaneous convection. This interaction is illustrated in Fig. 3.3 in which the instantaneous flow field and simultaneous convection are shown. By utilizing the multiple sensing locations of the THeTA, the mechanism by which the vortices increase the convection is easily shown. At left, a segment of the TRDPIV ROI is shown which contains multiple vortices interacting with five THeTA sensing location as indicated by the black dots. The contour of the vector plot indicates the U velocity magnitude and helps to illustrate where fluid is moving towards and away from the surface. At right, the bar plot represents the instantaneous convection at the five sensing locations shown relative to the laminar baseline.

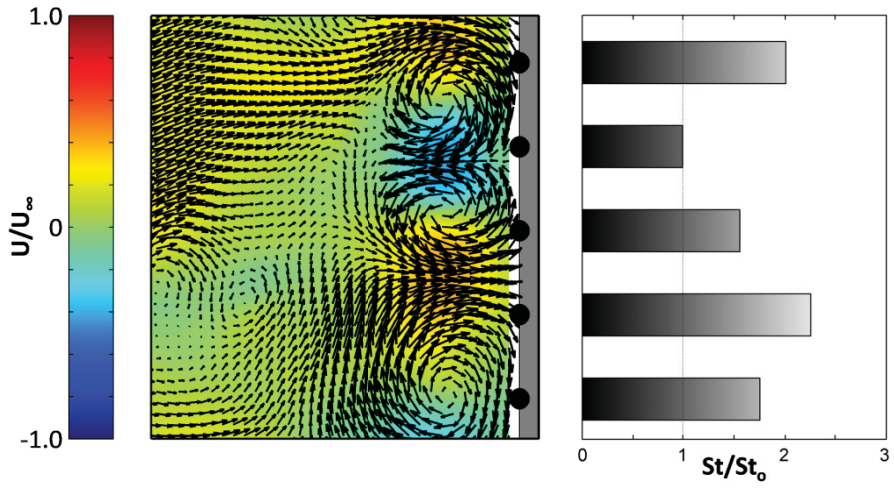

Fig. 3.3 Instantaneous snap shot of the flow field and convection. Sensor locations are indicated by the black dots and convection measurements are given by the bars at right. The contour of the vector field shows the magnitude of the U velocity. Convection increases are localized to areas of vortex downwash.

In the TRDPIV measured vector field, there are three strong vortices at the surface of alternating rotation orientation which produces alternating areas of downwash and upwash at the surface. As expected, the downwash regions correspond to high levels of convection since cool fluid from the freestream is being forced into the thermal boundary layer in these regions. Alternatively, regions of upwash correspond to low levels of convection since the fluid at the surface in these regions has been pulled along the heated surface prior to reaching these locations. Since heat has been transferred to this fluid while traversing the surface, it is ineffective at removing heat in these upwash regions.

An alternative way to view the interaction is shown in Fig. 3.4. Here, a single transient vortex track is shown along with the convection time-histories at three sensors located in the vicinity. At left, the identified vortex (with clockwise rotation) is shown over a time period of 5.3 s. the size of the marker indicates the measured circulation of the vortex while its color corresponds to the time at which it was identified as indicated by the color bar at right. The measured convection is shown at right for the three sensors as indicated by the markers in the left figure. At first, the vortex is both weak and far from the surface and has little impact of the convection over the first two seconds. Then, the vortex moves towards the surface and its circulation is amplified. At this point, the top sensor is positioned directly in the downwash region and experiences more than double the laminar baseline convection. As the vortex approaches the surface, the convection from the middle sensor also increases slightly. Once the vortex is close to the surface, its image in the wall (potential flow theory) causes it to move downward bringing

the middle sensor into a downwash region. Note, however, that by the time that the middle sensor is in a true downwash region the vortex has moved farther from the surface and weakened slightly. The middle sensor does experience an increase in convection but not to the extent of the top sensor. Finally, as the vortex continues to move from the surface and lose strength, the convection falls back to the baseline level. Since the bottom sensor remained in the upwash region of the vortex, its convection remained below the baseline level for nearly the entire test.

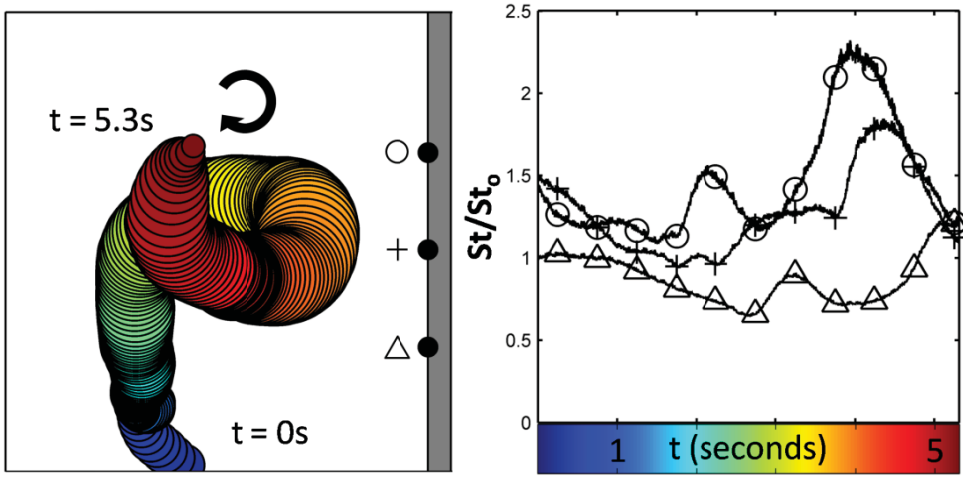

Fig. 3.4 Transient interaction of a single vortex with the surface and resulting convection. Vortex location and strength are indicated by the circular markers at left while the color corresponds to the time at right. Convection history for three nearby sensor locations is shown.

3.7 Comparison of the analytical model and experimental results

The analytical model was tested by using it to predict the transient convective heat transfer coefficient at the heat flux sensor locations using the properties of the vortices identified in the TRDPIV measurements. For each of the turbulent cases, comparisons were made for the center 6 sensors (3-8) to prevent vortices from outside the TRDPIV ROI from influencing the results. In all, 36 comparisons were made (3 grids X 2 trials X 6 sensors) for the entire 13 second duration of the TRDPIV measurements. The following section along with Fig. 3.5 through Fig. 3.8 gives a detailed description of the measured convection and the fluid structure during a particularly interesting set of vortex interactions from one of the tests. Table 3.2 then summarizes the findings from the remaining tests.

Fig. 3.5 shows the three vortex tracks that influence one particular sensor over the final 3.5 seconds of test #1 of grid 2. As in Fig. 3.4, the marker's size indicates the circulation of the vortex while its color corresponds to the time. At right is the normalized Stanton number measured by the sensor and the

vertical dotted lines delineate between the three tracks. The vortex shown at each point in time is shown because it caused the smallest calculated characteristic time (largest estimated augmentation) at the sensor location at that point in time.

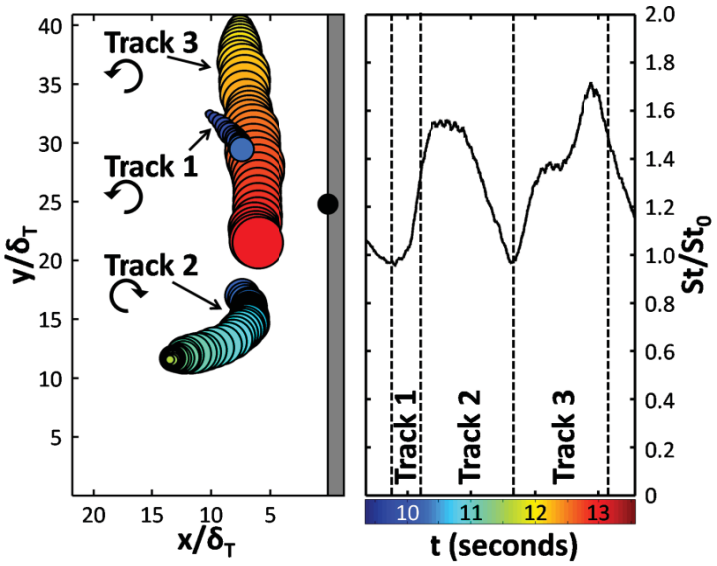

Fig. 3.5 Three vortex tracks and resulting measured convection. Marker size indicates relative strength (circulation) of vortex while the fill color corresponds to the time as indicated at right where the measured convection is shown.

Examining Fig. 3.5 along with Fig. 3.6 gives a clearer picture of the interaction process. Fig. 3.6 shows the measured vortex properties over the same 3.5 seconds as Fig. 3.5 and again the vertical lines delineates between the three tracks. Specifically, the non-dimensional distance from the vortex to the sensor (+) and the measured circulation (◊) is shown. At the beginning of the time shown, there is no strong vortex in the vicinity of the sensor and the convection is at nearly the baseline level. At this time, the vortex which most strongly influences the convection at the sensor location is approximately 13 boundary layer thicknesses away and has a circulation of less than $1cm^2/s$. This vortex then grows in strength as it approaches the stagnation region (and the sensor) with a corresponding increase in measured convection. Then, at t=10.25s, a more dominant vortex emerges. Although vortex number 2 starts approximately the same distance from the sensor, it is stronger with a circulation of $5cm^2/s$ compared to $3.5cm^2/s$. This clockwise rotating vortex forces fluid straight through the thermal boundary layer towards the sensor, increasing the convection to almost 60% above baseline levels. Then, as the vortex begins to move away and weaken, the convection returns to the baseline level. At t=11.7s, vortex 3 appears and quickly grows into a dominant vortex. The counter-clockwise vortex forms above the

sensor then moves downward along the surface. As the vortex approaches and eventually passes the sensor, its circulation grows to a maximum of $9cm^2/s$. This causes the convection to spike at a value nearly 75% higher than the baseline just as the vortex reaches the sensor. Then, as the sensor begins to enter the upwash region of the vortex, a drastic decrease in convection is observed even though the vortex is still quite close to the sensor.

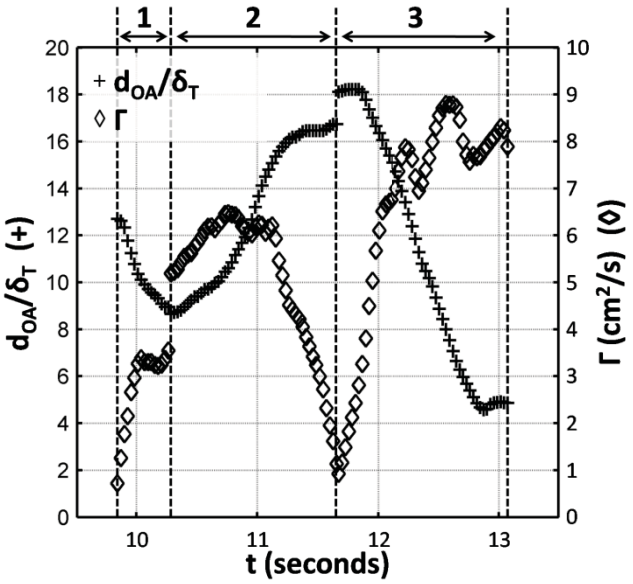

Fig. 3.6 Transient properties of the three vortices during the interaction time

From the measured vortex properties, the transient model inputs were calculated as shown in Fig. 3.7. The Biot-Savart calculated induced velocity is shown (◊) with the non-dimensional distance that the fluid must travel within thermal boundary layer (d_{BA}, +). When the fluid travels a short distance within the thermal boundary layer (values of d_{BA} near one) the sensor is in the downwash region and the fluid is traveling nearly perpendicular to the surface. Larger values indicate that the fluid is sweeping along the surface prior to reaching the sensor location. The average speed that the fluid travels along this distance is proportional to the induced velocity which is a measure of both the strength and proximity of the vortex. At t=10.6s, the induced velocity is at a local maximum and d_{BA} is at a local minimum. Fluid, therefore, is quickly traveling a short distance to reach the surface and little heat is transferred to the fluid prior to reaching the surface. Note that in Fig. 3.5, t=10.6s corresponds to a local maximum in the measured convection. Then, as the vortex dies, V_{IND} falls to essentially zero prior to the arrival of the third vortex. In this third vortex track, the affect of upwash versus downwash is most visible. For most of its life, the vortex is above the sensor and, since the vortex has counter-clockwise rotation, the sensor

remains in its downwash. Once the vortex passes the sensor however, the sensor enters the upwash region. Once this occurs, fluid enters the thermal boundary layer far below the sensor and must travel upwards along the surface prior to reaching the sensor as indicated by the large value for d_{BA}. This fluid has ample time to warm as it slides along the surface and the heat transfer is reduced.

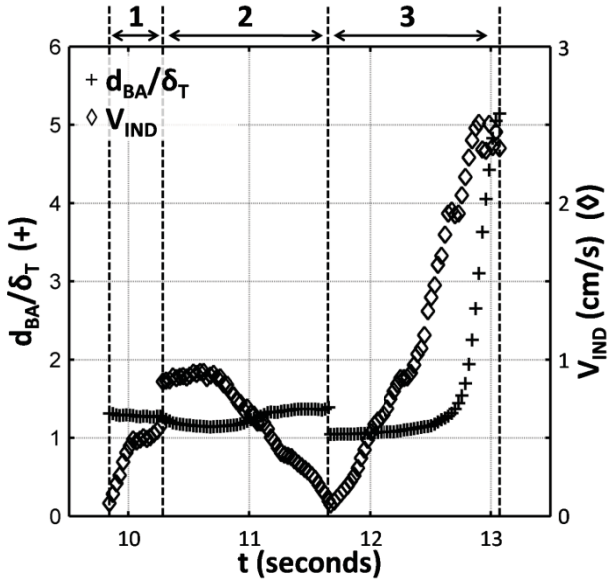

Fig. 3.7 Transient model inputs derived from vortex properties

In Fig. 3.8, the final model prediction is shown with the measured convection. The shaded region indicates the 3.5 seconds discussed in the previous three figures and the vertical dotted lines again delineate between the different tracks. The transient model prediction matches the measured convection well in terms of both shape and magnitude. The two distinct spikes in the measured convection both correspond to times when freestream fluid is quickly reaching the sensor from outside the thermal boundary layer. Times of low convection occur either when fluid is passing very slowly through the thermal boundary layer (weak and/or distant vortex) or when fluid must travel a great distance within the thermal boundary layer (upwash region of vortex). The mechanistic model developed performs quite well considering the complexity of the flow field. Therefore, if the formation of these large-scale coherent structures can be accurately predicted, using LES for instance, the resulting convection can be modeled without solving for the fine scale motions in the near-wall region. Finally, the success of the model also implies that, although there are multiple vortices present at any given time, one vortex is generally dominant at a particular location. The added complication of attempting to

account for the affects of multiple different vortices at the surface can be eliminated if the dominant vortex can be determined.

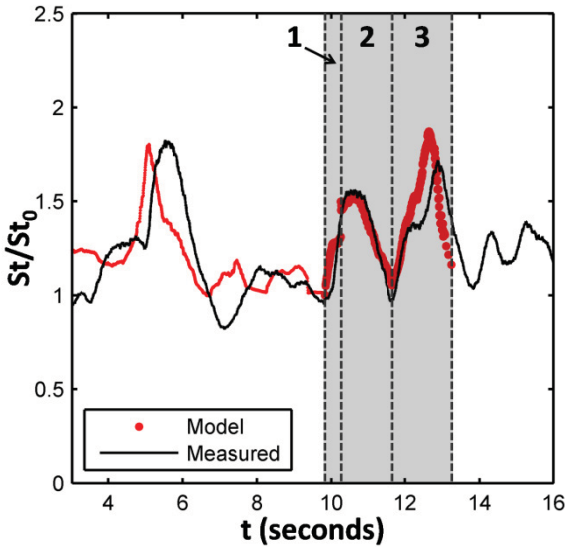

Fig. 3.8 Model prediction with measured convection. The shaded region corresponds to the 3.5 seconds studied in detail in the previous three figures.

Finally, since the model works well in predicting the convection during individual vortex interactions, it would be expected to provide an accurate estimate of the time-averaged turbulent heat flux augmentation. The results are shown in Table 3.2 where the augmentation is calculated based on the laminar baseline value of h_0=755W/m^{2}K. As in previous studies, the measured augmentation decreases with increasing length scale. The model accurately predicts this trend with particularly good results for the smaller two length scales. This is a strong indication that the time-averaged heat transfer augmentation observed in the past is simply the overall effect of a number of these transient vortex interactions.

Table 3.2 Summary of time-averaged augmentation and model predictions

Grid	Λ (cm)	Measured		Model	
		$\bar{h}$ (W/m^{2}K)	Aug (%)	$\bar{h}$ (W/m^{2}K)	Aug (%)
1	0.81	1042	38	1036	37
2	1.93	977	29	984	30
3	3.24	971	29	862	14

3.8 Conclusions

This work has successfully applied a simple vortex model to predict the increase in convection observed in the stagnation region of a flow containing large-scale freestream turbulence. It is shown that coherent structures which form due to the amplification of vorticity dominate the flow field and directly increase the convection. A simple model was developed to predict the resulting time-resolved convection based on the measured vortex location and circulation. Using the model, the resulting convection was accurately predicted in a time-resolved fashion taking only the transient properties of the vortices present as inputs. Evidence supporting the model's capabilities is provided by its successful validation in turbulent flows of varying integral length scale. These promising results support the hypothesis that coherent structures are the mechanism by which heat transfer is augmented in turbulent flows. Modeling the affect of these structures gives a new approach to calculating the heat transfer augmentation in turbulent flows once the large-scale structure of the flow is known.

3.9 Acknowledgements

The principle author would like to thank Dr. Andrew Gifford for his work developing and characterizing the turbulence grids and stagnation model. This material is based upon work supported by the National Science Foundation under Grant No. CTS-0423013. Any opinions, findings, and conclusions or recommendations expressed in this material are those of the authors and do not necessarily reflect the views of the National Science Foundation.

4 Development and Evaluation of the Time-Resolved Heat and Temperature Array

David O. Hubble and Tom E. Diller

Published in the ASME Journal of Thermal Science and Engineering Application, Vol. 2, Sept 2010

4.1 Abstract

The development and evaluation of a differential style heat flux gauge is presented. The sensor is constructed from spot-welded foils of copper and constantan on either side of a thin Kapton polyimide film and is capable of measuring the heat flux and surface temperature at ten locations simultaneously. Analytical modeling was performed to estimate the sensor's sensitivity and time response. Calibrations were performed in conduction and radiation yielding an average heat flux sensitivity of 20.4 μV/(kW/m^2). Time response measurements were also performed which gave an average 63% time response of 168 milliseconds. The capabilities of the sensor are demonstrated by showing its use in ongoing convection research.

4.2 Nomenclature

a	=	stagnation flow parameter (1/s)
α	=	thermal diffusivity (m^2/s)
C	=	specific heat (J/kg-K)
δ	=	sensor thickness (μm)
h	=	convective heat transfer coefficient (W/m^2-^{o}C)
k	=	thermal conductivity (W/m-^{o}C)
L	=	characteristic length (m)
ν	=	kinematic viscosity (m^2/s)
Pr	=	Prandtl number
ρ	=	density (kg/m^3)
q"	=	heat flux (W/m^2)
R"	=	thermal resistance (^{o}C/(W/m^2))
S	=	sensitivity (μV/(kW/m^2))
Se	=	Seebeck coefficient (μV/^{o}C)
T	=	temperature (^{o}C)

Tu = turbulence intensity (%)

T = time (s)

τ = time constant (s)

ΔT = temperature difference (^{o}C)

U = uncertainty

U = freestream velocity (m/s)

V = Voltage (volts)

ΔV = voltage difference (volts)

Subscripts

0 = initial

1 = top

2 = bottom

G = glue

in = input

K = Kapton

out = output

P = paint

ref = reference

SS = steady state

TC = thermocouple

4.3 Introduction

The accurate characterization of a thermal system requires the measurement of both temperatures and energy fluxes. While temperatures can be measured in a variety of ways, the accurate measurement of heat flux is still a challenge. This paper reports on the development and evaluation of a simple heat flux sensor capable of acquiring multiple simultaneous, time-resolved heat flux and surface temperature measurements. This capability allows the sensor to measure the distribution of heat flux over a surface to better describe the thermal environment. Examples of research areas where this sensor could be used include gas turbines, electronics cooling, and biological systems.

Heat transfer rates have been measured using a variety of sensors operating on different principles (Diller 1993). One popular type of heat flux sensor is the differential sensor. By measuring the

temperature drop across a known thermal resistance, the heat flux through the sensor is determined using Fourier's Law which, for 1-D steady state, reduces to

$$q'' = \frac{k}{\delta}\Delta T \qquad \textbf{4.1}$$

assuming the properties of the thermal resistance layer are uniform and constant. In Eq. 4.1, *k* and δ are the thermal conductivity and thickness of the resistance layer between the two temperature measurements. The temperature difference across the thermal resistance layer (ΔT) can be measured using either thermocouples or resistance temperature detectors (RTDs).

Thin-film heat flux gages have certain advantages over other types of differential heat flux sensors. It is generally possible to place a number of sensors on a single film which allows the heat flux to a surface to be mapped. This is particularly important when investigating the effects of non-uniform boundary conditions on heat transfer, such as turbulence, jets, and transition. Another advantage is that thin-film gages can be made flexible, allowing them to be mounted to curved surfaces such as airfoils.

Thin sensors have a frequency response that is faster than traditional designs such as the Schmidt-Boelter gage (Kidd and Adams 2001). One such sensor is the Heat Flux Microsensor (HFM) (Hager, Simmons et al. 1991) which has a thermal resistance layer approximately 1 micron thick and utilizes a sputtered thermopile to measure the temperature difference. Experiments have shown that the frequency response of the HFM is better than 100kHz (Holmberg and Diller 1995). The HFM's principle disadvantages are that it provides only a single point measurement and must be inserted into the test structure.

Several researchers have developed thin-film differential heat flux sensors. Ortolano and Hines (Ortolano and Hines 1983) created a thermopile to measure the temperature drop across a thermal resistance layer. Their sensor was able to produce a large output at the expense of poor spatial resolution. Epstein et al. (Epstein, Guenette et al. 1986) used vapor deposition to deposit nickel RTDs on either side of a 25 micron polyimide (Kapton®) substrate. A similar sensor was developed by Piccini et al. (Piccini, Guo et al. 2000) except that RTDs were only deposited on one side of the polyimide. The sensor was then mounted on a test article which was manufactured from metal whose temperature was monitored using a thermocouple. Since the thermal conductivity of the model was high, it was assumed that the temperature measured by the thermocouple accurately represented the backside temperature

of the heat flux gage. The heat flux at each RTD location was then determined by the temperature difference between the RTD and the thermocouple.

Recently, a new type of heat flux sensor was developed at Virginia Tech (Ewing, Gifford et al. 2010). The Heat Flux Array (HFA) is a differential heat flux sensor which utilizes a pair of vapor deposited copper/nickel thermocouples to directly measure the temperature drop across the sensor. Since the temperature drop is directly measured, the voltage generated is proportional to the heat flux through the gage. The principal problem with this sensor stemmed from the fragility of the thin-films produced by the vapor deposition process. The current paper reports on the development, fabrication, and calibration of an improved version of the HFA called the Time-Resolved Heat and Temperature Array (THeTA). The THeTA utilizes spot welded thermoelectric foils instead of deposited films which produces a more sensitive and robust sensor.

4.4 Sensor Design

The THeTA is a differential sensor that measures the temperature drop across the thermal resistance layer by a series of two thermocouples. Thermocouples were chosen over RTDs for their ability to directly measure a temperature difference rather than individual temperatures and for their long term stability. The junctions of the two thermocouples are located directly across from each other on opposite sides of the thermal resistance, Kapton® HN in this case. Using Kapton® as the thermal resistance sets the theoretical upper temperature limit of the THeTA at 300^{o}C. Fig. 4.1 shows the design concept of the THeTA. The voltage generated between the two positive thermoelectric alloys, ΔV_1, is a direct measure of the temperature difference, T_1-T_2. Also, the voltage generated between one of the positive thermoelectric alloys and the negative thermoelectric alloy, ΔV_2, is a measure of the temperature where the two traces meet, T_1 in Fig. 4.1. The ability to measure both heat flux *and* surface temperature is vital in convection research since this allows the convective heat transfer coefficient to be directly measured in a time-resolved manner. In addition, knowing the temperature distribution over the surface can be used to quantify the thermal disturbance caused by the presence of the gage [1]. Also, recent work has demonstrated that a sensor capable of measuring both the heat flux through the sensor as well as the temperature of the sensor can provide a more accurate measurement of the actual heat flux to the sensor as well as increase the temporal response of the sensor (Hubble and Diller 2010).

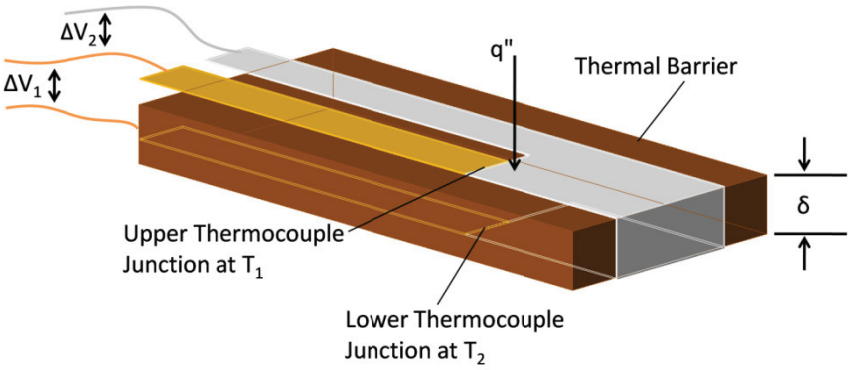

Fig. 4.1 Conceptual design of the THeTA. The temperature drop is proportional to ΔV_1 and the surface temperature is indicated by ΔV_2

The thermoelectric alloys selected for the THeTA were copper and constantan, better known as type T thermocouple alloys. Type T was selected because it offers a number of advantages over other thermocouple types. First, since the positive metal is copper, copper wires can be used to carry the signal from the sensor to the data acquisition unit without creating any additional thermocouple junctions. Second, type T alloys offer a comparatively high Seebeck coefficient at 41μV/^{o}C (ASTM 1981). Finally, since constantan is commonly used in strain gages, it is widely available in thin sheets.

4.5 Sensor Fabrication

The THeTA reported on in this paper was equipped with ten measurement locations. Fig. 4.2 shows the THeTA during construction. The thermocouple pairs were formed by spot welding precision cut foils of type T thermocouple alloys which were 12.5 microns thick. At the weld location, the copper foil was 1.58mm (1/16”) wide and overlapped the constantan foil by 3.16mm (1/8”). The two foils were welded at many locations over this overlap area so the sensing area can be assumed to be 1.58mm by 3.16mm. Ten such pairs were placed on one THeTA at 6.35mm (1/4”) spacing along a line. The thermocouple pairs were connected from one side of the gage to the other by folding the constantan foil over the edge of the Kapton®. As designed, one THeTA is able to measure the heat flux at ten locations as well as the surface temperature on either side of the sensor at all ten sensing locations. Typically, the THeTA is wired so that ten heat fluxes and ten surface temperature measurements are obtained.

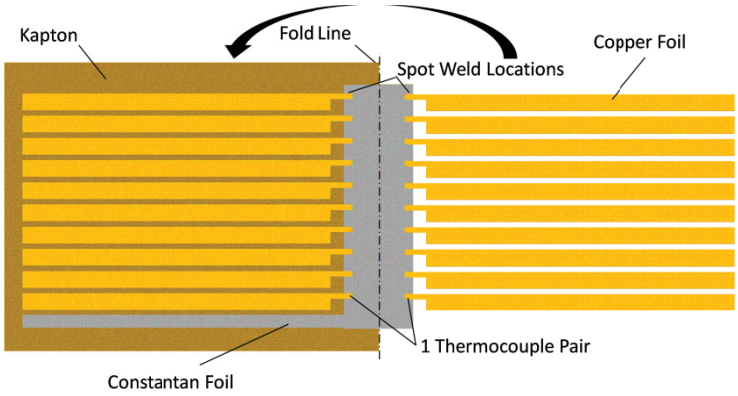

Fig. 4.2 THeTA during construction. Spot-welded thermoelectric foils are folded over Kapton resistance barrier.

One constantan and twenty copper extension wires were used to carry the signals from the THeTA to the data acquisition system. The extension wires were soldered to the foils at the edge opposite the heat flux measurements. Once welded and folded, the foils were bonded to the Kapton using a thermally activated epoxy. The entire gage was also encapsulated in 3 micron thick Mylar using the same epoxy. These two processes were accomplished simultaneously in a hot press with the gage between two sheets of Teflon. Encapsulating the gage serves multiple purposes. First, it protects the foils from oxidation. Second, the Mylar isolates the gage electrically, allowing its use on conductive materials. Finally, encapsulating the gage waterproofs it, allowing it to be used in research in water tunnels. Fig. 4.3 is a drawing of the completed gage after encapsulation. As a final step, the sensor is painted using Zynolyte flat black paint if it will be used to measure a radiative heat flux. Since the sensor discussed in this paper was calibrated in radiation, it received the black coating.

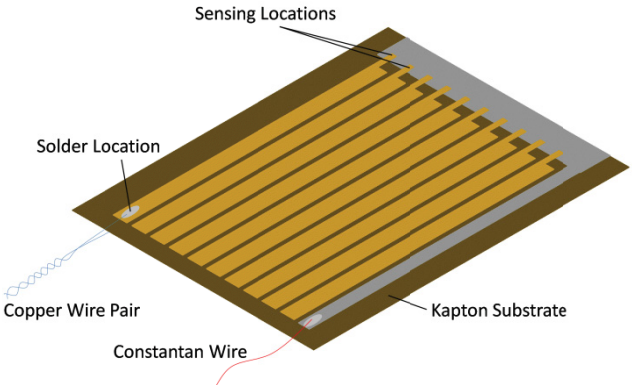

Fig. 4.3 Completed THeTA wire for 10 heat flux and surface temperature measurements

4.6 Theoretical Sensitivity and Time Response

The sensitivity of the THeTA is dependent on the Seebeck coefficient of the thermoelectric materials used and the thermal resistance of the resistance layer between the thermocouple junctions. Multiplying these two parameters gives the theoretical sensitivity of the sensor.

$$S_{THeTA} = \frac{\delta}{k} Se = R'' Se \qquad \textbf{4.2}$$

Fig. 4.4 shows a slice of the THeTA along with a model of its electrical analog circuit. For the sensitivity estimations only the resistances are needed. The capacitances are later used to determine the theoretical time response of the sensor. For the THeTA, the thermal resistance in Eq 4.2 (R") is the combined thermal resistance of the three layers between the two thermocouple layers. From Fig. 4.4 R" is the resistance of the Kapton® plus the resistance of the glue layer on either side of the Kapton. The resistances of the thermocouple layers are neglected because they are more than two orders of magnitude smaller than any of the other layers.

$$R'' = 2R_G + R_K \qquad \textbf{4.3}$$

Each individual resistance is simply the ratio of thickness to thermal conductivity. Based on measurements of the Mylar, Kapton®, and welded foils, the thickness of the glue layer was estimated from measurements of the average completed gage thickness. By assuming that all four glue layers were the same thickness, the glue layer was determined to be approximately 20 microns thick. The thermal conductivity of the epoxy was assumed to be 0.20 W/(m-K) based on the measurements of Tanaeva and Evseeva (Tanaeva and Evseeva 1997). The thickness of the Kapton® was measured to be 50 microns and Dupont reports a thermal conductivity of 0.12 W/(m-K) for type HN Kapton®. Adding these individual resistances gives R"=6.167E-4 K/(W/m^2). Multiplying the thermal resistance by the room temperature Seebeck coefficient (41 μV/^{o}C) gives a theoretical sensitivity of 25.3 μV/(kW/m^2).

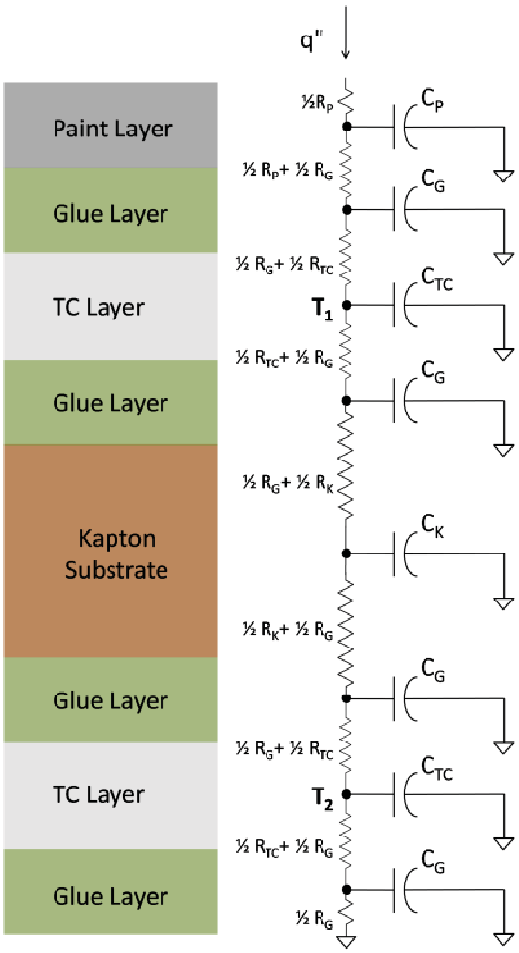

Fig. 4.4 Cross sectional view of THeTA and its electrical analogy

The time response of differential heat flux sensors depends on how long it takes thermal energy to diffuse through the sensor and establish a linear temperature profile within the sensor. The RC network shown in Fig. 4.4 was used to determine an estimate of the THeTA's time response. The capacitance of each layer is the product of the layer's thickness, density, and specific heat. In the electrical analog circuit, each layer was treated as a lumped capacitance. Therefore, as far as the thermal storage term was concerned, the entire layer was at a uniform temperature. A fourth order Runge-Kutta method was used to solve the resulting set of eight coupled ordinary differential equations for a step input in heat flux.

Solving the coupled equations gives the temperature history at each node in the circuit. The heat flux measured by the gage is then:

$$q''(t) = \frac{T_1(t) - T_2(t)}{R''} \quad \textbf{4.4}$$

To determine the time response of the sensor, the ratio of the measured heat flux to heat flux input (q''_{in}) was examined. This ratio was found to be within 10% of a first order exponential response ($1-e^{-t/\tau}$) for all t > 0.014s. Therefore, the sensor can be approximated as a first order system in the timeframe of interest. The time required for the ratio to equal .632 (τ) was found to be 162 milliseconds.

4.7 Sensor Calibration

In order to confidently use any heat flux sensor, it must first be accurately and thoroughly calibrated. As a first calibration, the Seebeck coefficient of the thermoelectric alloys used was determined experimentally. Next, the THeTA was calibrated in both conduction and radiation using RDF and Schmidt-Boelter reference sensors respectively. The radiation calibrations were further used to experimentally determine the time response of the sensor. The THeTA was then analyzed in convection by affixing it to a plate which experienced Hiemenz stagnation flow in a low speed water tunnel. Since the THeTA measures both heat flux and surface temperature, it was used to measure the heat transfer coefficient which was then compared to the analytical solution for Hiemenz flow. Finally, the Hybrid Heat Flux (Hubble and Diller 2010) method was applied to the THeTA measurements to demonstrate how the capabilities of such a sensor can be increased. The results of the calibrations are summarized in Table 4.1 at the end of this section and an uncertainty analysis is presented in section 4.9 for each set of calibrations.

4.7.1 Seebeck Coefficient Measurement

Since a traditional bulk wire thermocouple was not used in the manufacture of the THeTA, the Seebeck coefficient of the copper/constantan foils was measured. This measurement was made by affixing the THeTA to an aluminum plate equipped with a resistance heater. A type E thermocouple was embedded in the aluminum plate and served as the temperature reference. The reference thermocouple came supplied with a voltage to temperature polynomial and a quoted accuracy of 0.5°C. A 24-bit National Instruments (NI) USB-9161 thermocouple DAQ was used to measure the voltages from the THeTA as well as the type E standard at 1Hz. Since all temperature measurements were made relative to room temperature, no cold junction compensation was needed. Prior to running a test, the aluminum plate was wrapped in fiberglass insulation to minimize heat losses to the surroundings. The

plate was then heated to 10, 20, and 30 degrees above room temperature and allowed to reach steady-state. Once steady conditions were reached, the voltages produced between the constantan and copper foils were measured and averaged over 5 minutes (300 samples). The Seebeck coefficient was then determined by dividing this average voltage by the measured temperature rise. This calculation yielded a Seebeck coefficient of the copper/constantan foils of 34.29±0.64μV/K which is somewhat lower than the value typically associated with type T thermocouples. Using this value in place of the 41μV/K value from section IV decreases the predicted sensitivity to 21.2 μV/(kW/m^2).

4.7.2 Conduction Calibration

The THeTA was calibrated in conduction using the conduction calibration facility located in the Advanced Experimental Thermo-fluids Engineering Research (AEThER) laboratory at Virginia Tech. This system is described in detail in (Gifford, Hubble et al. 2010) and is shown in Fig. 4.5. One-dimensional conduction is maintained between two aluminum plates, one heated and the other cooled. An RDF Corp. heat flux sensor (HFS-20455-1) was used as a reference as it has approximately the same thermal resistance as the THeTA. The RDF sensor and the THeTA were placed in a mask of 75 micron thick Kapton® HN the size of the plates in the conduction calibration facility as shown in Fig. 4.5. Above and below the Kapton® layer, a layer of conformable Gap Pad© was used to minimize contact resistance. This layer also served to make the overall resistance between the top and bottom plates more uniform. For example, even though the overall resistance of the THeTA, RDF sensor, and Kapton® vary by up to 40%, once placed in series with two layers of the Gap Pad© (δ=2E-3m, k=1W/mK) the thermal resistance was uniform to within 5% over the area of the plates. Therefore, it was assumed that the heat flux through the RDF sensor was within 5% of the heat flux through the THeTA. Once the stack was assembled, it was insulated to help ensure that only conduction from the hot plate to the cold plate occurred.

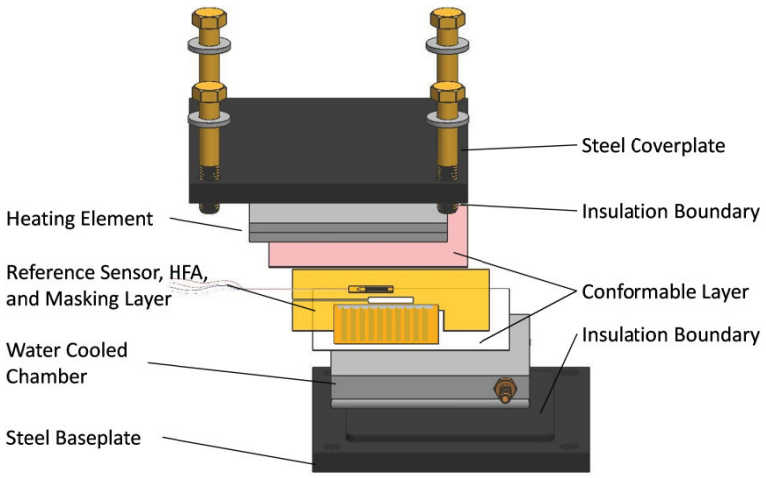

Fig. 4.5 Steady-state conduction calibration facility. Heat flux is maintained between the upper heated palte and the lower cooled plate.

Conduction calibrations were performed at three levels of heat flux, 5, 10, and 15 kW/m^2. This was controlled by varying the voltage to the resistance heater on the hot plate. The ten heat flux signals from the THeTA were amplified using custom amplifier boards whose design is described by Ewing (Ewing 2006). These amplified signals were then recorded at 10Hz using a 16-bit NI USB 6225 DAQ connected to a PC. A 24-bit NI USB-9161 thermocouple DAQ was used to record the RDF output as well as the output of the type T thermocouple built into the RDF. Both RDF signals were sampled at 1Hz.

To determine the sensitivity of the ten sensors on the THeTA, each sensor's output was divided by the calibrated output of the reference sensor.

$$S_{THeTA} = \frac{\Delta V_{THeTA}}{V_{ref} / S_{ref}} \qquad \textbf{4.5}$$

S_{THeTA} was averaged over 5 minutes (300 samples) after the measured heat flux and RDF temperature had reached steady state.

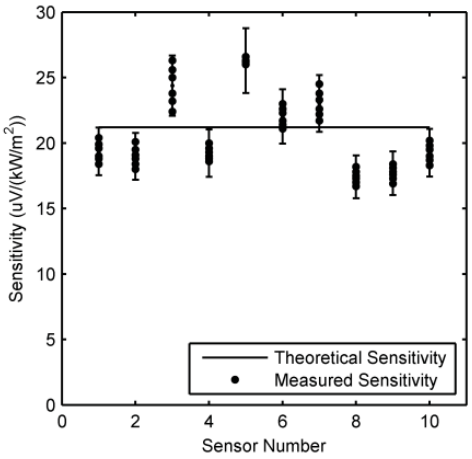

Fig. 4.6 Conduction calibration results with 95% confidence uncertainty and theoretical prediction

To demonstrate the repeatability of the conduction calibrations, the THeTA was calibrated at three heat flux levels, removed from the calibration stand, the Gap Pad© replaced, and the three tests repeated giving 6 total measurements of the sensitivity of the ten sensors. Fig. 4.6 shows the measured sensitivities, the 95% confidence uncertainty estimates, and the theoretical sensitivity calculated using Eq. 4.2. The estimated uncertainty was approximately 9% for the absolute heat flux calibration, the majority of which is from uncertainty in the heat flux that is actually supplied to the gage. Repeatability of all the measurements was better than this. Absolute heat flux calibrations at the national fire research labs gave variations of up to ± 17% (Pitts, Murthy et al. 2006) demonstrating the difficulty in absolute heat flux calibrations. The observed sensor to sensor variation shown in Fig. 4.6 is likely due to the non-uniform thickness of the glue layer, a parameter which proved difficult to control during manufacture. Fig. 4.7 demonstrates how the thickness of the sensor affects its sensitivity by plotting these two parameters against each other. With the exception of one outlier, the data shows a positive correlation between sensor thickness and sensitivity.

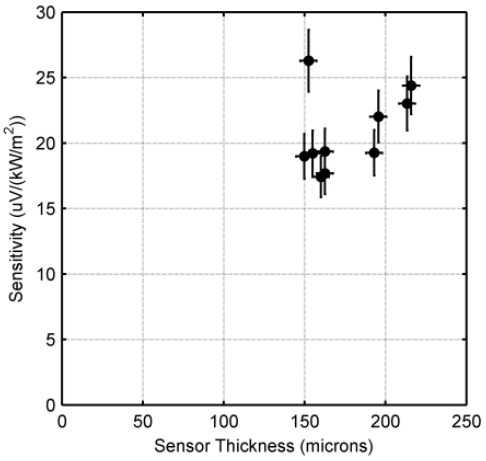

Fig. 4.7 Sensitivity dependence on sensor thickness

4.7.3 Radiation Calibration

Radiation calibrations were performed using a halogen lamp as a radiation source. Equipped with a 600 watt halogen lamp, the radiation facility focuses the radiant energy using an elliptical reflector which was machined from aluminum. The reflector was turned on a lathe and designed to have a focal point 31.7mm (1.25 inches) from its end with heat fluxes up to 200kW/m^2 obtainable. The radial heat flux distribution of the lamp at an axial location corresponding to the focal point of the reflector was characterized using a Vatell Corp. Heat Flux Microsensor (HFM-7) mounted on a 2-D traverse. The HFM reference sensor averages the heat flux over an area approximately 3mm in diameter. Fig. 4.8 shows the measured heat flux distribution and demonstrates that the heat flux is uniform to within 5% as long as the sensor is not more than 5mm from the centerline of the reflector. As previously stated, the sensing area of the THeTA is approximately 1.5mm by 3mm so the heat flux produced by the lamp can be assumed uniform over the THeTA sensing area.

A variable transformer was used to control the AC voltage to the halogen lamp and allowed the level of heat flux produced to be controlled. A Fluke 177 True RMS Multimeter with a quoted accuracy of 1% of reading was used to measure the RMS voltage supplied to the lamp. A Schmidt-Boelter water-cooled heat flux sensor (Medtherm model # GTW-7-32-485A) was used to calibrate the lamp and produce a curve which related the heat flux produced to the voltage supplied. The reference sensor was painted using the same Zynolyte flat black paint as was the THeTA for testing so there was no need to correct for emissivity mismatches. It was found that if the lamp was left on for more than about thirty seconds the reflector heated up enough to begin emitting additional radiation which caused the incident radiation to

the sensor to increase slightly with time. This problem was negated by placing a piece of standard plate glass between the lamp and the test sensor. Since the glass was nearly opaque in the far infrared, it blocked most of the radiation emitted by the reflector while still passing a large portion of the radiation from the much hotter lamp. Tests showed that with the glass in place, the incident radiation increased by less than 1% during the first 30 seconds of a test.

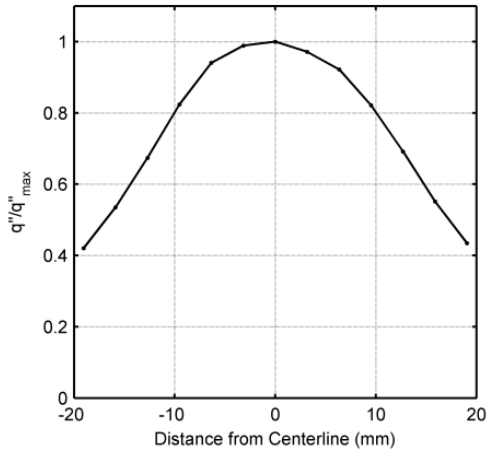

Fig. 4.8 Lamp radiation intensity as a function of radial location

Before the THeTA was calibrated in radiation, it was heat sunk by adhering it to an aluminum plate using the same thermally activated epoxy used in its construction. The calibrations were then completed by mounting the halogen lamp on a 2-D traverse in front of the sensor so that its position could be accurately controlled. A jig was constructed to aid in the positioning of the lamp and allowed the lamp's position relative to the sensor to be accurate to within 0.25mm. A shutter system was designed to subject the sensor to a step change of heat flux and consisted of a pneumatic cylinder which quickly removed a piece of sheet metal from between the lamp and the sensor. Once the lamp had been turned on and allowed to reach steady state (1-2 seconds), the cylinder removed the shutter. Two photodiodes were used to determine the speed of the shutter as it passed the sensor. These tests showed that the shutter was traveling at approximately 3.8 m/s and therefore uncovered the sensor in about 400 microseconds which is more than two orders of magnitude faster than the predicted response of the sensor. Therefore, the incident radiation can be treated as a perfect step input for analysis. Fig. 4.9 is a depiction of the radiation calibration facility.

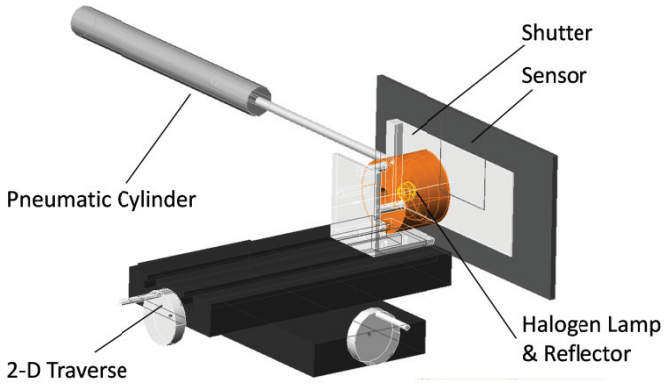

Fig. 4.9 Radiation calibration setup. Shutter utilized to provide a step change in incident flux

Each individual sensor on the THeTA was calibrated at heat fluxes of approximately 10, 15, and 20 kW/m^2. The signals from the THeTA were recorded using the same hardware used in the conduction calibrations except that the signals were sampled at 1kHz. It was necessary to sample at a higher rate to

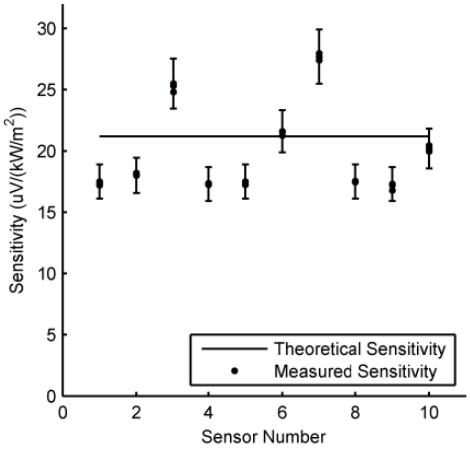

Fig. 4.10 Radiation calibration results with 95% confidence uncertainty and theoretical prediction

determine the time response and to acquire enough data for averaging since the total test time was approximately ten seconds. The data recorded during the first 500 milliseconds of the test was used to determine the sensor's time response while the last 5 seconds was used to determine the sensitivity of the sensors. The sensitivities were determined by dividing the sensor's output averaged over 5 seconds (5000 samples) by the heat flux absorbed by the Schmidt-Boelter with the lamp set at the same voltage. Fig. 4.10 shows the measured sensitivities, the 95% confidence uncertainty estimates, and the theoretical sensitivity calculated using Eq. 4.2. Note that for each sensor the measured sensitivities show very good agreement, far better than the estimated absolute uncertainty (95% confidence) of 8% shown

by the error bar. Radiation calibrations are generally more repeatable than conduction calibrations and are used more often for heat flux calibrations (Murthy, Tsai et al. 2000). It is believed that the relatively large change in sensitivity for sensors 5 and 7 (-34% and +20% respectively) was caused by the process of hot pressing the THeTA onto the aluminum plate which altered the relative thicknesses of the glue layers.

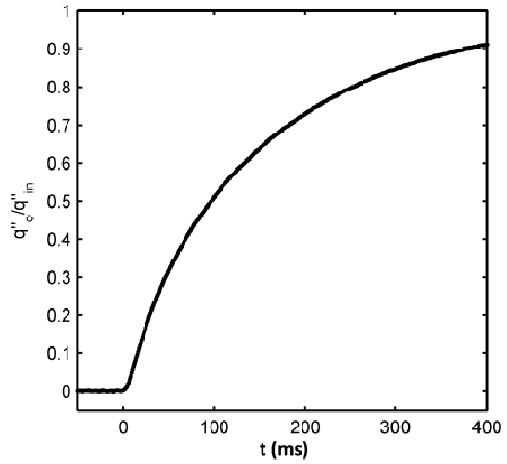

Fig. 4.11 Transient response of THeTA to step radiation heat flux input

To estimate the time response of the THeTA, the method outlined by Doebelin (Doebelin 2004) was used which utilizes the mathematical first-order exponential response to a step change input.

$$\ln\left(1-\frac{q_{out}}{q_{in}}\right)=\ln\left(e^{-t/\tau}\right)=\frac{-1}{\tau}t \qquad \textbf{4.6}$$

Plotting the left hand side as a function of *t* produces a linear curve with a slope of -1/τ if the sensor is behaving as a first order system. Fig. 4.11 and Fig. 4.12 show the sensor response as well as $\ln(1-q_0/q_{in})$ vs. *t*. The near linear behavior of the curve in Fig. 4.12 is an indication that the sensor is behaving as approximately a first-order type. This approximation in turn leads to a more accurate time response estimation compared to the alternative approach of determining the time required for the sensor's output to reach some threshold. To determine the slope of the curve in Fig. 4.12, a linear regression was fit to the data. Using the slope from the linear regression, the time constant for each sensor was determined as reported in the table at the end of the calibration section. The average measured time constant value of 168 milliseconds compares well with the predicted value of 162 milliseconds (section IV).

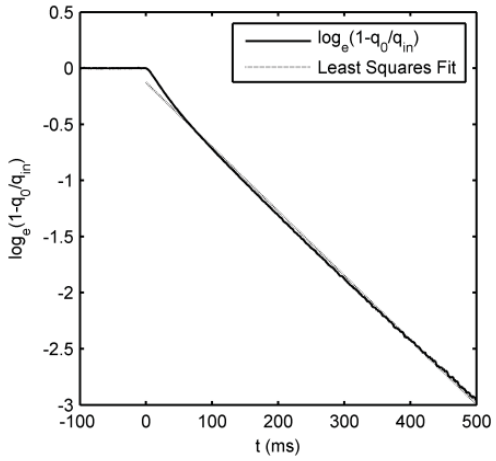

Fig. 4.12 Time response of the logarithmic heat flux and least squares fit. Fit used to measure first-order time constant

4.7.4 Hybrid Heat Flux Analysis

A recent paper by the authors (Hubble and Diller 2010) discusses a procedure called the Hybrid Heat Flux (HHF) method for increasing the performance of differential heat flux sensors. During transient tests, the heat flux flowing through the gage will be different to that flowing into the gage. By accounting for the heat stored by the gage in conjunction with the heat flowing through the gage, the accuracy and time response of a differential heat flux sensor can be improved. In order to apply this method, an extra calibration is needed to determine the thermal mass per unit area of the sensor. This value can be determined by mounting the sensor on an insulating material and subjecting it to a known, radiative heat flux. The thermal mass per unit area ($\rho C\delta$) is then measured as the inverse of the slope of the temperature history curve. Values of 680 to 710 J/(m^{2}K) were measured for the ten sensors on the THeTA. The HHF method is then applied as follows:

$$q''_{HHF} = q''_{Diff} + \frac{1}{2} q''_{Slug} \qquad \textbf{4.7}$$

where q''_{Diff} is the heat flux measured treating the THeTA as a differential sensor and q''_{Slug} is the value measured treating the THeTA as a slug calorimeter. In this case, the slug calorimeter term uses the average temperature measured by the THeTA:

$$q''_{Slug} = \rho C \delta \frac{d}{dt}\left(\frac{T_1 + T_2}{2}\right) \quad \textbf{4.8}$$

Fig. 4.13 shows a plot of the HHF method applied to the radiation calibration data which was presented in Fig. 4.14. A dramatic increase in time response is observed at the expense of a slight (3%) overshoot. Here, the 95% time response is improved by a factor of 14 from 509ms to 36ms. This corresponds to resolving sinusoidal signals with frequencies up to 6.4Hz with less than 10% amplitude attenuation.

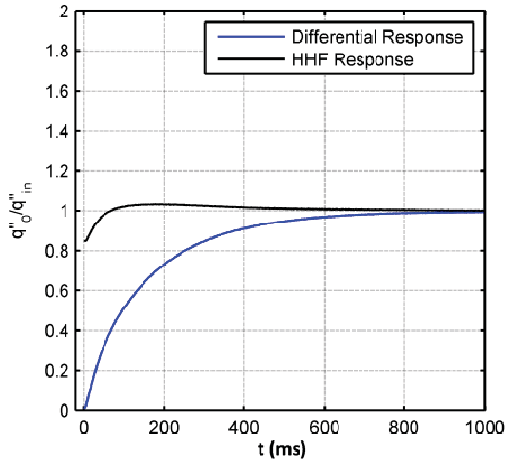

Fig. 4.13 Hybrid heat flux response of THeTA to step change input compared to differential response

4.7.5 Calibration Summary

Table 4.1 summarizes the results of the sensor calibration. Details of the estimated uncertainty calculation are provided in section 4.9.

Table 4.1 Summary of THeTA calibration results

Sensor	$S_{HFA\text{-}Cond}$	$S_{HFA\text{-}Rad}$	Time Constant	Thickness
	$\mu V/(kW/m^2)$	$\mu V/(kW/m^2)$	ms	microns
1	19.4	17.5	172	163
2	19.0	18.0	172	150
3	24.4	25.5	208	216
4	19.2	17.3	180	155
5	26.3	17.5	176	152
6	22.0	21.6	174	196
7	23.0	27.7	165	213

8	17.4	17.5	144	160
9	17.7	17.3	121	163
10	19.3	20.2	173	193
Uncertainty	9%	8%	13%	±5

4.8 Example of Sensor Application

4.8.1 Steady Convection

Using the THeTA, convective heat transfer coefficients were measured in a low-speed, low-turbulence (Tu < 1%) closed loop water tunnel. The aluminum plate to which the THeTA was mounted was attached to a stagnation model which spanned the width of the water tunnel's 0.61m square test section. The stagnation model measured 0.152m square by 0.61m wide and was equipped with an aft splitter plate to prevent vortex shedding interactions with the stagnation region. The THeTA was positioned horizontally such that all 10 sensors fell along the stagnation line. Using the resistance heater that was adhered to the back of the aluminum plate, the central, thermally isolated, test area was heated approximately 15°C above the water temperature. Flow measurements were made along the stagnation line directly upstream of the THeTA using Time-Resolved Digital Particle Image Velocimetry (TRDPIV)(Westerweel 1997). Fig. 4.14 shows the test setup. Tests were performed by allowing the heated aluminum plate to reach steady state conditions while the tunnel was run at U=0.10m/s. The convective heat transfer coefficient was measured by the THeTA using Newton's Law of Cooling.

$$h = \frac{q''}{\Delta T} \qquad \textbf{4.9}$$

ΔT was measured using the surface thermocouples on the sensor and q" was determined using the sensitivity found from the radiation calibrations. For comparison, an analytical value for h was calculated. For stagnation flows, Goldstein (Goldstein 1938) gives a solution for the heat transfer coefficient as

$$h = 0.5421k\,\mathrm{Pr}^{0.42}\sqrt{\frac{a}{\nu}} \qquad \textbf{4.10}$$

where k, ν, and Pr are the thermal conductivity, kinematic viscosity, and Prandtl number of the fluid (water in this case). The parameter a is the spatial acceleration constant and was found experimentally from the TRDPIV measurements to be a=0.98 s^{-1}. This agrees well with the correlation given by White (White 1974) for a square body in cross flow which relates the parameter a to the freestream velocity U and the body height L.

$$a \approx \frac{\pi}{2}\frac{U}{L} = 1.03 \qquad \textbf{4.11}$$

Using Eq. 4.10 with the fluid properties at the film temperature, the heat transfer coefficient was estimated to be 757 W/m^{2}K. Fig. 4.15 shows the comparison of the measured values of *h* along with Goldstein's prediction. On average, the THeTA measurement is about 10% higher than the analytical prediction.

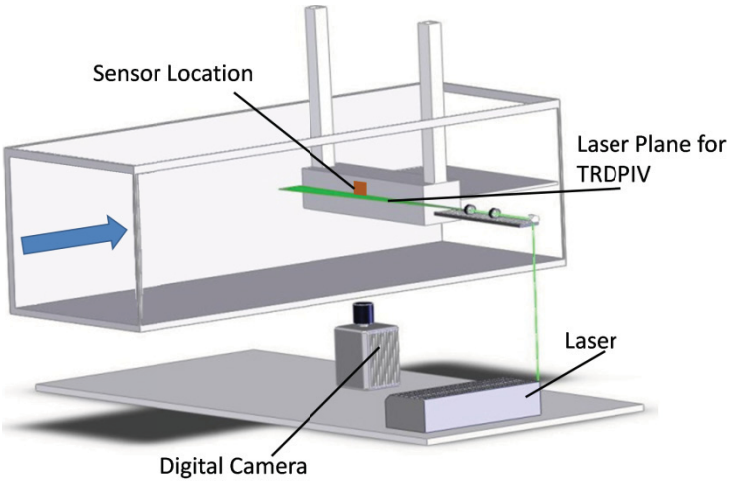

Fig. 4.14 Setup for convection analysis. Hiemenz flow produced in a water tunnel facility.

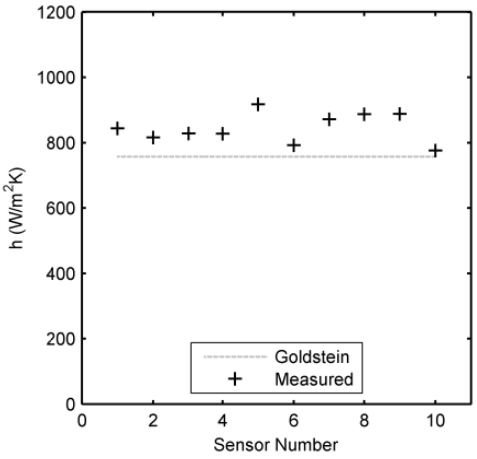

Fig. 4.15 Comparison of measured and predicted heat transfer coefficient values.

4.8.2 Unsteady Convection

One of the purposes for the development of the THeTA was to study the interaction of vortices with a boundary layer and their subsequent transient effect on the convective heat transfer coefficient. To

study this phenomena, a vortex ring (Shariff and Leonard 1992) was generated in water and allowed to impinge normally on the heated plate to which the THeTA was mounted. TRDPIV was used to measure the flow field directly in front of the sensor while the THeTA (with HHF applied) simultaneously measured the heat flux and surface temperature at ten points. Combining these two measurements (Eq. 4.9) allowed the time-resolved heat transfer coefficient to be determined. Fig. 4.16 shows the results obtained from the experiment. On the left is the flow field as measured by the TRDPIV just as the vortex ring impacts the plate after propagating from the left. The plot on the right is the heat transfer coefficient measured by the THeTA normalized by the natural convection value of 510 W/(m^{2}K). These measurements are made at the ten locations indicated by the dots at the right edge of the TRDPIV measured flow field. The vertical line indicates the time corresponding to the instantaneous TRDPIV field shown. When the vortex ring arrives, the heat transfer coefficient increases by over a factor of four indicating an *h* value of more than 2000 W/(m^{2}K).

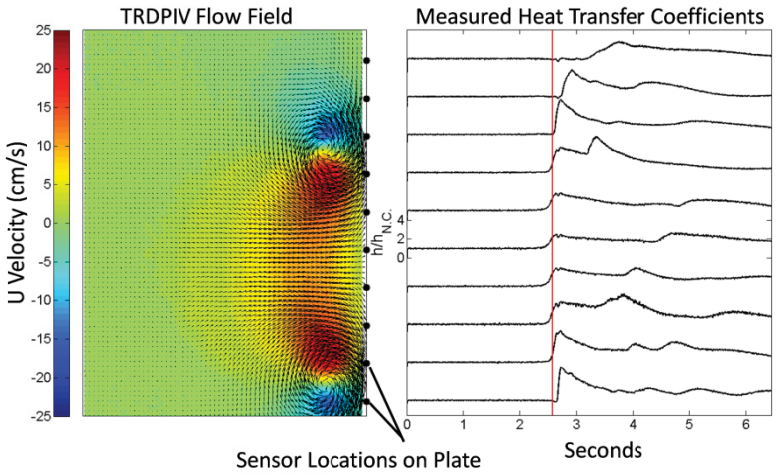

Fig. 4.16 Sensor application, vortex ring impinging on a heated plate.

4.9 Uncertainty Analysis

The following uncertainty analysis was performed on the calculation of the sensitivity of the THeTA in conduction and radiation and follows the procedure outlined by Coleman and Steel (Coleman and Steele 1989). The total uncertainty in the THeTA sensitivity, S_{THeTA}, for a particular measurement is

$$\left(\frac{U_{S_{THeTA}}}{S_{THeTA}}\right)^2 = \sum_{i=1}^{j}\left(\frac{1}{S_{THeTA}}\frac{\partial S_{THeTA}}{\partial X_i}U_{X_i}\right)^2 \qquad \textbf{4.12}$$

where Us_{THeTA} is the total experimental uncertainty, which is a function of experimental variables X_i. The total 95% uncertainty in each variable is given by Ux_i, while the partial derivatives are the associated sensitivity coefficients. Ux_i is estimated or calculated by combining variable's precision and bias error limits. Bias limits for the DAQs, thermocouples, and reference sensor were provided while precision limits were calculated from 128 continuous samples of nominal room temperature data using a Student's t-distribution with a 95% confidence interval. Plugging Eq. 4.5 into Eq. 4.12 gives the uncertainty of the sensitivity found in conduction.

$$U_{S_{THeTA-Cond}} = S_{THeTA}\sqrt{\left(\frac{U_{V_{THeTA}}}{V_{THeTA}}\right)^2 + \left(\frac{-U_{Vref}}{V_{ref}}\right)^2 + \left(\frac{U_{Sref}}{S_{ref}}\right)^2 + U_{rep}{}^2} \qquad \textbf{4.13}$$

where U_{rep} is the estimated bias error in the repeatability of the conduction calibration facility and is estimated at 5%. Uncertainty calculations for radiation calibrations are performed in the same manner as shown in Eq. 4.14.

$$U_{S_{THeTA-Rad}} = S_{THeTA}\sqrt{\left(\frac{U_{V_{THeTA}}}{V_{THeTA}}\right)^2 + \left(\frac{U_{q''}}{q''}\right)^2} \qquad \textbf{4.14}$$

where $U_{q''}$ is a combination of the error in the voltage reading supplied to the lamp and the error in the curve generated from the Schmidt-Boelter data. The total error in the conduction calibrations was determined to be approximately 9% while the radiation calibrations yielded an uncertainty of 8%.

To determine the uncertainty in the time constant estimation, a sequential perturbation method was used as outlined by Moffat (Moffat 1985). This method essentially uses finite differences to estimate the relative sensitivities of the time constant calculation to each measured variable. After some simplification, the time constant can be expressed as

$$\tau = \left[-\frac{d}{dt}\left(\ln\left|1 - \frac{V - V_0}{V_{SS} - V_0}\right|\right)\right]^{-1} \qquad \textbf{4.15}$$

where V is the measured voltage from the sensor, V_0 is the measured voltage offset, and V_{SS} is the measured voltage once the sensor reached steady state. Since the term inside the parentheses should be linear, the temporal derivative was estimated by the slope of a linear regression fit to the data. Each independent variable (V, V_o, and V_{SS}) was then perturbated independently by its respective uncertainty to determine the uncertainty contributions from each variable. These individual uncertainties were then

combined to determine the overall uncertainty for the time constant calculations. Averaging the uncertainties for the 10 sensors yielded an overall uncertainty of 13%.

4.10 Conclusions

The THeTA offers improved performance compared to currently available heat flux sensors. The use of thermoelectric foils results in a durable, sensitive transducer. In addition to measuring heat flux, the THeTA is capable of measuring simultaneous surface temperatures which allows it to more completely describe the thermal environment. Temperature measurements are also used in the HHF method to increase the performance of the sensor. The resulting time-resolved heat flux and temperature measurement capabilities make the THeTA very useful in a variety of research and practical applications. The capabilities of the THeTA were demonstrated by conduction and radiation calibrations as well as an example of the THeTA measuring the time-resolved convective heat transfer coefficient resulting from a transient flow field.

4.11 Acknowledgments

This material is based upon work supported by the National Science Foundation under Grant No. CTS-0423013. Any opinions, findings, and conclusions or recommendations expressed in this material are those of the authors and do not necessarily reflect the views of the National Science Foundation.

5 A Hybrid Method for Heat Flux Measurement

David O. Hubble and Tom E. Diller

Published in the ASME Journal of Heat Transfer, Vol. 132, Dec 2010

5.1 Abstract

The development and evaluation of a novel hybrid method for obtaining heat flux measurements is presented. By combining the spatial and temporal temperature measurements of a heat flux sensor, the time response, accuracy, and versatility of the sensor is improved. Sensors utilizing the hybrid method are able to make heat flux measurements on both high and low conductivity materials. It is shown that changing the thermal conductivity of the backing material four orders of magnitude causes only an 11% change in sensor response. The hybrid method also increases the time response of heat flux sensors. The temporal response is shown to increase by up to a factor of 28 compared to a standard spatial sensor. The hybrid method is tested both numerically and experimentally on both high and low conductivity materials and demonstrates significant improvement compared to operating the sensor as a spatial or temporal sensor alone.

5.2 Nomenclature

C	=	specific heat
Fo	=	Fourier number, $t\alpha/\delta^2$
k	=	thermal conductivity
h	=	convective heat transfer coefficient
q''	=	heat flux
q_0''	=	step change heat flux for simulation
q_1''	=	heat flux into sensor face
q_2''	=	heat flux out of sensor back
$q''_{Differential}$	=	heat flux measured by differential sensor
q''_{HFM}	=	heat flux measured by HFM reference sensor
q''_{Slug}	=	heat flux measured by slug calorimeter
t	=	time
t_{ss}	=	time to reach steady-state
T_1	=	temperature at sensor face
T_2	=	temperature at sensor back
T_{ave}	=	average sensor temperature

T_r	=	measured jet recovery temperature
$T_{S\ HFM}$	=	HFM surface temperature
$T_{S\ HTHFS}$	=	HTHFS surface temperature
T_∞	=	room temperature
x	=	distance from sensor face
α	=	thermal diffusivity of sensor, $k/\rho C$
Δt	=	time between temperature measurements, inverse of sampling frequency
δ	=	thickness of sensor
ρ	=	density

5.3 Introduction

Modeling of thermal systems requires a combination of temperatures and energy fluxes for prediction of their performance. Temperatures are commonly measured by a variety of standard methods, but the measurement of heat flux is a particular challenge because it is an energy flux normal to a plane of material rather than a property of a material. Therefore, sensors to measure heat flux usually must be mounted onto a material that provides a good heat sink so that the energy flow is not impeded. This makes it very difficult to use heat flux gages to measure heat flux on materials that are not good thermal conductors. The purpose of this paper is to present a new method which allows heat flux gages to make accurate measurements on any type of backing material. Applications include furnaces to thermal protection systems for spacecraft.

5.4 Background

Two of the most common modes of heat flux measurement are that of a differential heat flux sensor and that of a slug calorimeter (Diller 1993). A differential heat flux sensor measures the temperature difference over a spatial distance with a known thermal resistance, as illustrated in Fig. 5.1. The temperature difference is used to calculate the heat flux through the sensor from the steady-state version of Fourier's Law. T_1 is the temperature of the exposed face while T_2 is the temperature at the back of the sensor.

$$q''_{\text{Differential}} = k\frac{T_1 - T_2}{\delta} \qquad \textbf{5.1}$$

Under steady-state conditions the heat flux entering the sensor in Fig. 5.1, q_1'', is equal to that leaving, q_2''. Hager (Hager 1965) calculated the 98% response time to a step change of heat flux at the surface in terms of the sensor's thickness and thermal diffusivity. This is often considered as steady-state.

$$t_{ss} = 1.5\frac{\delta^2}{\alpha} \qquad \textbf{5.2}$$

Hager's (Hager 1965) analysis was performed on the ideal case of a sensor mounted on a perfect heat sink where the backside temperature, T_2, remains constant.

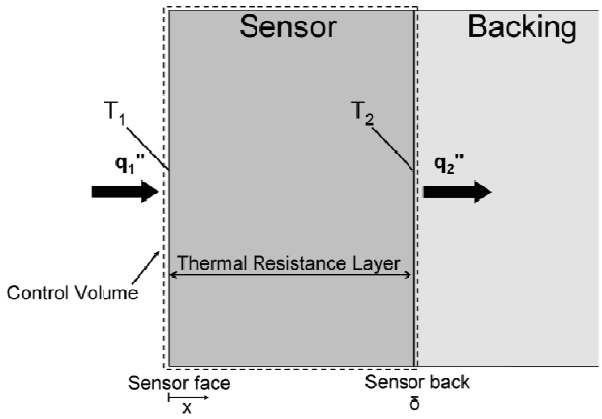

Fig. 5.1 Sensor-backing system. T_1 and T_2 are the two sensor surface temperatures.

In a slug calorimeter the amount of thermal energy absorbed by the sensor is measured as a function of time. The rate of change of the sensor's temperature is measured and its thermal capacitance is known. As illustrated in Fig. 5.1, conservation of energy for a control volume surrounding the sensor "slug" yields

$$q''_{\text{Slug}} = \rho C \delta \frac{dT_{ave}}{dt} = q_1'' - q_2'' \qquad \textbf{5.3}$$

where $\rho C \delta$ is the thermal mass of the slug per sensor area. The heat loss (q_2'') is minimized by insulating all sensor surfaces except for the sensor face. If the average temperature within the slug were known, Eq. 5.3 would perfectly measure the net heat flux into the slug. However, since it is not possible to measure the average temperature, the slug is typically made from a high conductivity material and the temperature at the back surface is used to approximate the slug's average temperature. Therefore, for a short time after a heat flux is applied to the slug, thermal energy is being absorbed by the slug (the slug's average temperature is increasing) before any heat has reached the back surface. This causes a delay before the slug accurately measures the actual net heat flux. The 99% response time to a step change of heat flux at the surface is given as

$$t_{ss} = 0.54\frac{\delta^2}{\alpha} \quad \textbf{5.4}$$

by Hightower et al. (Hightower, Olivares et al. 2008). This analysis was performed assuming a perfectly insulated backside surface (q_2"=0).

While these two modes of operation can be used for specific measurement applications, they both have serious limitations. For example, for a differential gage to have a fast time response, it must be very thin. This is difficult to achieve in harsh environments where sensors typically must be made with a substantial thickness to survive. Also, since a differential sensor only measures heat flowing through it, it must be provided with a good heat sink. This necessitates its mounting on or in a high conductivity material, not an insulator. The main problems encountered when using a slug calorimeter include adequately insulating the slug to minimize losses as well as noise amplification due to the differential operation. Also, since the output of a slug is proportional to the rate at which its temperature is changing, it is unable to measure a heat flux at steady-state. It is worth noting that the design criteria for these two types of sensors are opposite. A differential gage more accurately measures q_1" when q_2" is maximized with minimal heat storage in the gage. Conversely, a slug calorimeter needs to minimize q_2" and maximize the stored thermal energy.

A number of papers have reported using a combination of the spatial and temporal changes of temperature to infer or improve heat flux measurements. Kidd and Adams (Kidd and Adams 2001) used finite-element analysis to determine a response function for their Schmidt-Boelter heat flux gages. This was used to compensate for the energy deficit caused by the thermal capacitance of this differential style gage. They were able to substantially increase the time response of the heat flux measurements for their transient tests in high speed wind tunnels. A complete analysis of a simpler thin polyimide differential gage mounted on a metal heat sink was performed by Epstein et al. (Epstein, Guenette et al. 1986). This enabled measurements from steady-state to 100 kHz on metal turbine blades, but required solution of the equations for one-dimensional transient conduction for a particular mounting material. A “plug-type heat flux gauge” was developed by Liebert (Liebert 1992) to account for the combination of conduction and storage in the post normal to the surface. Four temperatures were measured along the post as a function of time and compared with transient temperature solutions to determine the surface heat flux. Experimental results were obtained for metal turbine blade models. Unfortunately, the method did not work well when the sensor was mounted in a low thermal conductivity material (Rooke, Fralick et al. 1998).

A popular variation of the slug calorimeter uses a single temperature measurement at the surface of the material and a semi-infinite solution to the transient thermal field. The results can be used only over a short time span before the thermal front reaches the backside of the material, which corresponds to the time *before* results from a slug calorimeter can be used. The data reduction procedure involves inverse solution methods because the measured surface temperature is the known boundary condition that is used to solve for the corresponding heat flux. Several digital and analogue processing methods have been developed in efforts to minimize the effect of noise in the resulting heat flux signal (Schultz and Jones 1973; George, Rae et al. 1991; Walker and Scott 1998). There are a number of methods available for measuring the transient surface temperature. Point measurements can be made with resistance temperature sensors (RTD's) (Anthony, Jones et al. 2005) or coaxial thermocouples (Kidd, Nelson et al. 1994). Optical methods include liquid crystals(Wang, Ireland et al. 1995), infrared thermography(Nasir, Ekkad et al. 2007), and thermographic phosphors (Bizzak and Chyu 1995) that can be used with high-speed imaging cameras to scan over an entire surface. The biggest limitations are that the initial temperature distribution throughout the material must be known, there are no steady-state results, and the test time is limited.

Clearly, there are advantages to including both the differential and transient slug type responses for measuring heat flux. It would be beneficial to design a simple sensor and analysis scheme which could utilize the advantages of these two sensor types together while minimizing their negative characteristics. It is with this goal in mind that the following analysis was performed on a simple one-dimensional sensor for such a hybrid heat flux (HHF) method.

5.5 HHF Methodology

5.5.1 Differential Term.

Fig. 5.1 shows the schematic of a one-dimensional heat flux sensor. The majority of differential heat flux sensors are designed to minimize 2-D effects and can therefore be treated as one-dimensional. The quantity q_1'' represents the heat flux into the sensor face, which is the desired measurement. Fig. 5.2 depicts a typical temperature profile resulting from a heat flux, applied at the sensor face, which diffuses through the sensor and into the backing material. These profiles will be non-linear until the entire system reaches steady-state at which point both curves will become linear. Using Fourier's law,

$$q'' = -k\frac{dT}{dx} \qquad \textbf{5.5}$$

the heat flux at any point can be calculated from the gradient of the temperature profile if the thermal conductivity is known.

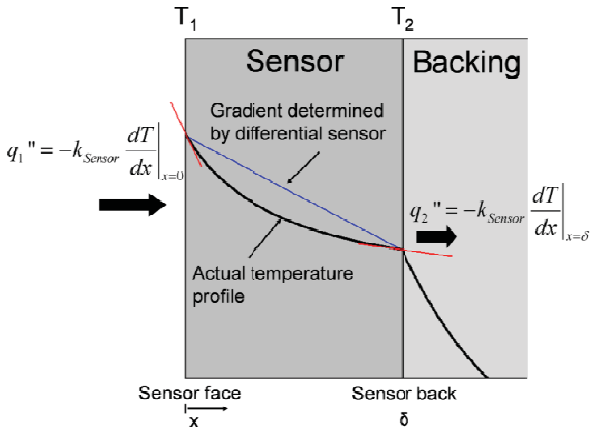

Fig. 5.2 Instantaneous temperature profile within sensor-backing system.

A differential heat flux sensor measures the temperature at the front and back surfaces of the sensor and indicates the heat flux based on the thickness and the thermal conductivity. Fig. 5.2 shows, however, that when the sensor is not at steady-state, the gradient (and therefore the heat flux) that the differential sensor is measuring (Eq. 5.1) is different from the gradient at the sensor face. However, once the temperature profile within the sensor is sufficiently developed, the gradient determined by the differential sensor equals the *average* of the gradients at the two surfaces. For example, it can be shown that this is true for any quadratic temperature profile, $T(x) = ax^2+bx+c$,

$$\underbrace{\frac{1}{2}\left(\left.\frac{dT}{dx}\right|_{x=x_1}+\left.\frac{dT}{dx}\right|_{x=x_1+\delta}\right)}_{\text{Average of two surface gradients}} = \underbrace{\frac{T(x_1+\delta)-T(x_1)}{\delta}}_{\text{Gradient determined by differential sensor}} = 2ax_1+a\delta+b \qquad \textbf{5.6}$$

Once the gradient measured by the differential sensor equals the average of the gradients at the two surfaces to within 2%, the temperature profile is considered fully developed. The time required for the temperature profile to develop can be calculated in a variety of ways. As an example, Eq. 5.7 utilizes the exact analytical solution for the case of a sensor mounted on a perfect heat sink subjected to a step change in surface temperature to calculate the gradients.

$$\left(\left.\frac{\partial T}{\partial x}\right|_{x=x_1}+\left.\frac{\partial T}{\partial x}\right|_{x=x_1+\delta}\right) = \frac{-2(T_1-T_2)}{\delta}+\sum_{n=1}^{\infty}\frac{-2(T_1-T_2)}{\delta}\exp\left(\frac{-n^2\pi^2}{\delta^2}\alpha t\right)\left(1+(-1)^n\right) \qquad \textbf{5.7}$$

The gradients at the two sensor surfaces are then compared to the gradient determined from the two surface temperatures, $(T_2-T_1)/\delta$, to see when they agree to within 2%. For the analytical case described by Eq. 5.7, a time corresponding to a Fourier number (non-dimensional time, $Fo = t\cdot\alpha/\delta^2$) of 0.12 is required. The Fourier number required for the temperature profile to become fully developed was also calculated analytically for a step change in heat flux on a perfect heat sink and was found to be 0.91. Numerical simulations of cases other than a perfect heat sink show that a step change in heat flux on a perfect heat sink requires the longest time to become fully developed. For a typical ceramic gage (Oishi, Gorbunov et al. 2006) with a thickness of 500μm and thermal diffusivity of 1.0E-5 m^2/s, a Fo of 0.91 corresponds to a time of 22.8 milliseconds. For a metallic sensor such as the High Temperature Heat Flux Sensor HTHFS (Gifford, Hubble et al. 2010) with a thickness of 3.2mm and thermal diffusivity of 5.5E-6 m^2/s a Fo of 0.91 corresponds to a time of 1.69 seconds.

Once the temperature profile is fully developed, Eq. 5.6 can be used to relate the heat fluxes q_1" and q_2". The temperature gradients at the sensor face and back surfaces represent the heat flux into and out of the sensor, respectively, and the differential sensor heat flux is proportional to the total temperature difference, $T_1 - T_2$. Substituting the corresponding heat fluxes into Eq. 5.6 gives

$$\frac{q_1"+q_2"}{2} = q"_{\text{Differential}} = k\frac{T_1-T_2}{\delta} \qquad \textbf{5.8}$$

5.5.2 Slug Term

A slug calorimeter measures heat flux by measuring the rate at which heat is absorbed by the slug. The absorbed flux represents the net heat flux into the control volume, $q_1"- q_2"$, as shown in Fig. 5.2. Eq. 5.3 states that this net heat flux can be measured using a slug calorimeter which measures the time rate of change of the slug's average temperature. As mentioned, the standard method for measuring this average temperature is to measure the temperature at the back of the sensor and assume that this approximates the actual average temperature. This is a valid assumption once enough time has passed for the heat that enters the sensor face to reach the sensor back. However, for the sensor shown in Fig. 5.1, both surface temperatures are known. By utilizing the temperature measurement at the sensor face, a more accurate measure of the absorbed heat flux can be made. Subsequently, the sensor can be operated as a slug calorimeter in three different modes; the sensor's average temperature can be approximated by the face temperature, the back temperature, or an average of the two. The response of a slug calorimeter to a step change in heat flux while mounted on a perfect insulator using these

three methods is shown in Fig. 5.3. The sensor properties and the numerical method are discussed in section 5.6.

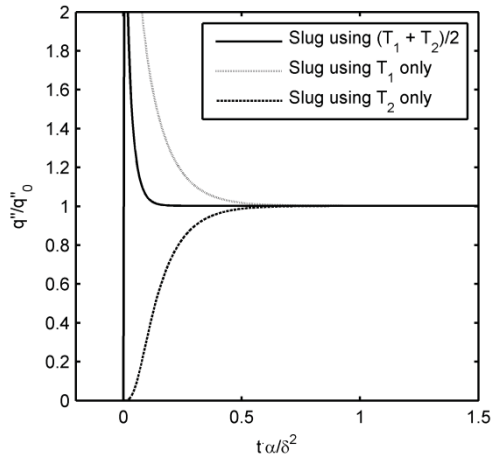

Fig. 5.3 Comparison of slug calorimeter response using different sensor temperature measurements.

Fig. 5.3 shows that utilizing only the surface temperature offers no advantages compared to only using the back temperature as it takes just as long for an accurate measurement to be made. On the other hand, utilizing the average of the two surface temperatures has advantages and drawbacks. By utilizing both the sensor face and back temperatures, the time response is more than a factor of three faster compared to using only T_2 but this temporal increase is accompanied by a large overshoot. The overshoot associated with using T_1 in the slug measurement is a result of the $\sqrt{t}$ dependence of the surface temperature since the sensor acts as a semi-infinite solid before heat has had a chance to reach its back surface. Since the surface temperature history is a function of $\sqrt{t}$, it has an infinite temporal derivative at t=0. While the overshoot associated with using the average of the two surface temperatures is initially large, it measures the applied heat flux more accurately than the standard method (curve is closer to one) for all Fourier numbers greater than 0.02. Therefore, in many situations it is advantageous to utilize the average of the two surface temperatures in order to increase the temporal response of the sensor. From this point on, q''_{Slug} will denote a slug calorimeter that utilizes the average of T_1 and T_2 unless specified otherwise.

$$q''_{\text{Slug}} = \rho C \delta \frac{d}{dt}\left(\frac{T_1 + T_2}{2}\right) = q_1'' - q_2'' \qquad \textbf{5.9}$$

5.5.3 Hybrid Heat Flux

To combine the spatial and temporal responses of a heat flux sensor, only Eqs. 5.8 and 5.9 are needed, as repeated here.

$$q_1'' + q_2'' = 2q''_{\text{Differential}} \quad \textbf{5.10}$$

$$q_1'' - q_2'' = q''_{\text{Slug}} \quad \textbf{5.11}$$

Combining Eqs. 5.10 and 5.11, and solving for the desired q_1'' yields the HHF method.

$$q_1'' = q''_{\text{Differential}} + \frac{1}{2} q''_{\text{Slug}} \quad \textbf{5.12}$$

Equation 5.12 shows how the differential and slug calorimeter outputs of a sensor can be combined. While this represents a simple model, it was derived from basic thermal energy conservation.

The validity of Eq. 5.12 can be supported by examining two limiting cases. First, consider the limit of a perfectly insulating backing material. For this case, the one-dimensional heat equation within the sensor simplifies to

$$\frac{d^2T}{dx^2} = \text{Const.} \quad \textbf{5.13}$$

once the temperature profile is fully developed. The solution to this equation yields a temperature profile within the sensor that is quadratic with a gradient of zero at $x=\delta$ since $q_2''=0$. This means, using Eq. 5.6, that the differential sensor will measure exactly half the heat flux entering the sensor. Also, since q_2'' is zero for this case, the slug calorimeter will measure the heat flux perfectly, i.e. $q''_{Slug} = q_1''$. Therefore, the hybrid method described in Eq. 5.12 will measure the correct heat flux for this case.

Another limiting case occurs when the entire system is at steady-state on a perfect heat sink ($d^2T/dx^2=0$). For this case, the temperature profile within the sensor is linear. Consequently, the differential sensor will measure the exact heat flux, $q''_{Differential} = q_1''$. Also, since the system is at steady-state, the time derivative of the temperature everywhere in the sensor is zero and the slug calorimeter will measure zero heat flux. Once again, the HHF method (Eq. 5.12) handles this limiting case.

The HHF method requires that a sensor be designed such that T_1, T_2, and ΔT are measured. However, accurately measuring any two of these allows the third to be calculated since $\Delta T = T_1 - T_2$. For the two sensors already mentioned (Oishi, Gorbunov et al. 2006; Gifford, Hubble et al. 2010) the hybrid

method can be used without any change in design since these two sensors already measure the required temperatures.

5.6 HHF Numerical Validation

In order to validate the HHF method, 1-D transient conduction through the sensor-backing system (Fig. 5.1) was modeled using finite-difference computations. This was accomplished using an in-house developed code which utilizes an implicit discretization of the 1-D heat equation in MATLAB. The derivation of this discretization can be found in (Incropera and DeWitt 2002). The boundary conditions at the senor face allowed any thermal condition to be applied including time varying fluxes and convective or radiative conditions. Temporal and spatial steps were kept sufficiently small to eliminate any grid and time step dependence. This was verified for the parameters shown in Table 5.1 by increasing both the temporal and spatial resolution by a factor of ten over the values in Table 5.1 and comparing the results to those obtained using the lower resolution. In both cases, the discrepancy was less than 0.1%. Changing material properties as well as the thickness of the sensor allowed for any sensor design to be tested. Also, the material properties and thickness of the backing material could be varied to investigate how this affected sensor performance. For all numerical simulations shown, the HTHFS (Gifford, Hubble et al. 2010) (described in section 5) was modeled mounted on a backing material three times thicker than the sensor. It was verified that the baking material thickness did not significantly affect the analysis. This was done by varying the thickness from one to ten times the thickness of the sensor which caused less than a 3% change in sensor performance. For all tests, the boundary condition at the back surface of the backing material was held at a constant temperature. Table 5.1 summarizes the parameters used in the numerical simulations.

Table 5.1 Parameters used in numerical simulation

Parameter	Value	Units
Sensor thermal conductivity	22	W/m K
Sensor density	7278	kg/m^3
Sensor specific heat	548	J/kg K
Sensor thickness	3.175	mm

Backing thickness	9.525	mm
Backing thermal conductivity	0.22 to 2200	W/m K
Spatial step	0.03175	mm
Time step	0.5	ms

At each time step in the code, the temperatures at the face and back of the sensor (T_1 and T_2) were recorded. This allowed the sensor's performance in all three modes of operation to be evaluated using only these two temperature histories along with the sensor's properties. The sensor's response to a step heat flux of q_0" is plotted against Fourier number (dimensionless time) in Fig. 5.4. A step change in heat flux is used in all the numerical simulations because it allows for the most direct comparison between different modes of sensor operation and backing conditions.

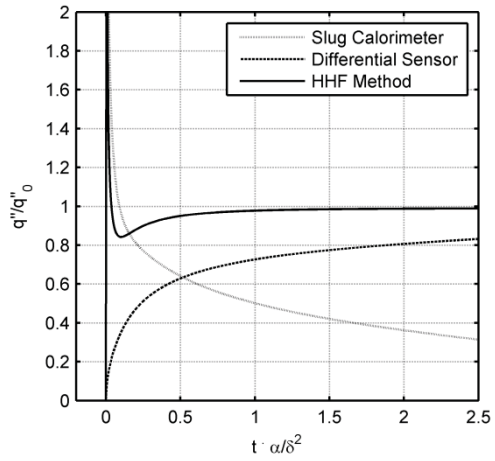

Fig. 5.4 Simulated response of sensor in three modes of operation. HHF method significantly increases sensor performance.

In the analysis shown in Fig. 5.4, the properties of the backing material were identical to the properties of the sensor. The accuracy as a slug calorimeter decreases with time while the differential sensor's accuracy increases with time. As the temperature of the sensor increases, more heat is conducted through the sensor into the backing material (q_2" is increasing). If steady–state conditions were reached, the differential sensor would measure the exact heat flux. Because the backing material in this case is identical to the sensor, the entire system acts as a semi-infinite solid, which never reaches

a steady-state. Fig. 5.4 shows the speed and accuracy of the HHF method. Not only does the HHF capture the transient heat flux better than the slug calorimeter, it quickly settles to the proper steady-state value.

The analysis was extended to a wide range of backing materials in Fig. 5.5. The error of the three methods for a step heat flux input is shown as a function of time and backing material thermal conductivity. In these tests, the backing material's thermal conductivity was stepped from 100 times lower than that of the sensor to 100 times greater. Specific regions are shown for each mode of sensor operation. The differential region is bounded by the high conductivity backing case above and the low conductivity case below while the slug calorimeter region is bounded by the low conductivity case above and the high conductivity case below. The large size of these regions indicates the sensitivity of the slug calorimeter and differential sensor to backing material conductivity. The much smaller region of the HHF in Fig. 5.5 indicates that its performance is far less dependent on the properties of the backing material. In fact, although the backing material thermal conductivity is varied by four orders of magnitude, at no point does this cause more than an 11% change in the response of the HHF method.

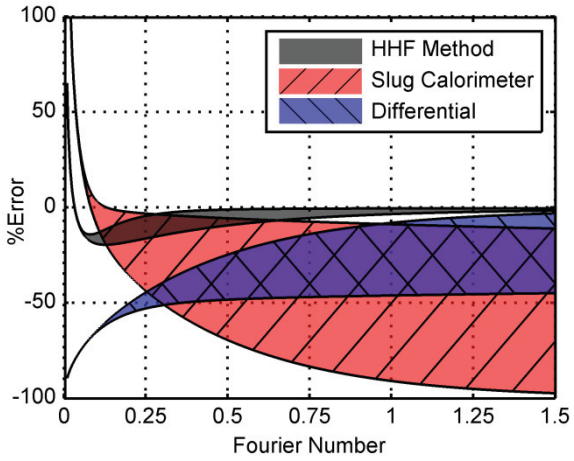

Fig. 5.5 Error as a function of time and backing material thermal conductivity for three modes of sensor operation.

The results in Fig. 5.5 can also be used to show the sensor response time as a function of backing material properties. The HHF region is bounded by the low conductivity case above and the high conductivity case below and obtains accuracy to within 2% at a Fourier number of 0.33 on an insulator and 1.40 on a conductor. Even on a highly conductive material, the best case scenario for a differential sensor, the HHF is faster (Fo=1.4 vs. 1.5). Finally, it is worth noting that for all Fourier numbers greater

than 0.02, the error of the HHF is never more than ±20% regardless of backing material. For comparison, a differential sensor requires a Fourier number greater than 0.57 to measure the heat flux to within ±20% on a perfect conductor, 28 times slower than the HHF method.

The primary limitation with the HHF method is the large over prediction in heat flux at Fourier numbers less than 0.02. As discussed previously, this is because the face temperature is used in the slug calorimeter term (Eq. 5.9). In certain situations, it would be desirable to eliminate the overshoot of the HHF method. This can be accomplished by using only the back temperature (T_2) in the slug calorimeter term as shown in Fig. 5.6. Hereafter, if the slug term of the hybrid method only includes the back temperature (T_2), it will be referred to as the HHF_2 method. Fig. 5.6 shows that there is no overshoot and the HHF_2 method still accurately measures the steady-state heat flux regardless of backing material. The only drawback to this method compared to the standard HHF method is its slower response time. While the time required to reach an accuracy of 2% is essentially unchanged, the time required for accuracy within 20% is drastically increased. For any Fourier number greater than 0.02 the HHF is within 20% while the HHF_2 method requires a Fourier number greater than 0.57, the same as for a differential sensor on a conductor. This implies that if the sensor is attached to a perfect heat sink, the HHF_2 method offers no advantages compared to a standard differential sensor. For all real materials, however, the HHF_2 method is superior to either the differential sensor or the slug calorimeter. As in Fig. 5.5, the top of the HHF region in Fig. 5.6 is the low conductivity case while the bottom of the region is the high conductivity case.

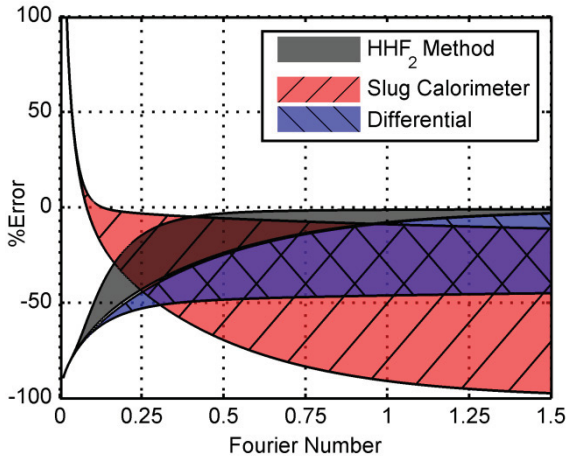

Fig. 5.6 Error of HHF_2 using only T_2 in slug calorimeter term of HHF compared with standard methods.

At the other extreme, the hybrid method was analyzed with the slug term only containing T_1 (HHF_1). This response is shown in Fig. 5.7 and demonstrates the versatility of the hybrid method. By simply changing the weighting of T_1 and T_2 in the slug term the response can be changed drastically. Fig. 5.5 through Fig. 5.7 show that as the ratio of T_1/T_2 in the slug term of the hybrid method increases, the overshoot increases and the response time decreases. In this case, accuracy within 2% is obtained at a Fourier number of 0.75, which represents a significant improvement compared to the value of 1.40 for the standard hybrid method shown in Fig. 5.5. On the other hand, accuracy within 20% doesn't occur until a Fourier number of 0.125 is reached instead of the value of 0.02 reported from Fig. 5.5. With this in mind, it is worth noting that Fig. 5.6 and Fig. 5.7 represent two extremes for implementing the hybrid method. Which method is best must be determined on a case by case basis. If no overshoot can be tolerated, T_2 should be heavily weighted. On the other hand, if response time is critical and some overshoot can be tolerated, T_1 should be more heavily weighted. The case where the two temperatures are weighted evenly (Fig. 5.5) is shown as a good tradeoff between overshoot and response time.

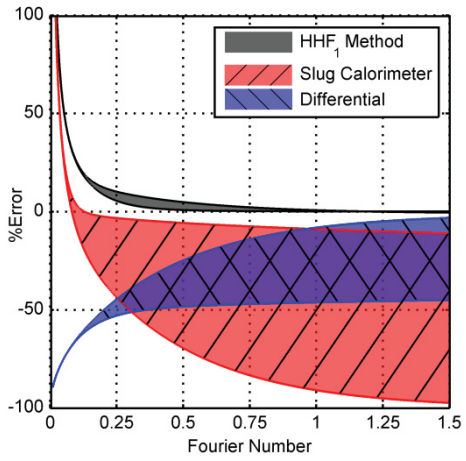

Fig. 5.7 Error of HHF_1 using only T_1 in slug calorimeter term of HHF compared with standard methods.

5.7 HHF Experimental Validation

To further validate the hybrid method, it was experimentally tested using a HTHFS(Gifford, Hubble et al. 2010). The HTHFS, shown in Fig. 5.8, consists of a thermopile which directly measures the temperature difference across the sensors as well as two thermocouples which measure the face and back surface temperatures. When operated as a differential sensor, the HTHFS has a sensitivity of 579 +/- 29 $\mu V/W/cm^2$. The HTHFS is made from materials which are thermally conductive to ensure that the heat flow is primarily one dimensional.

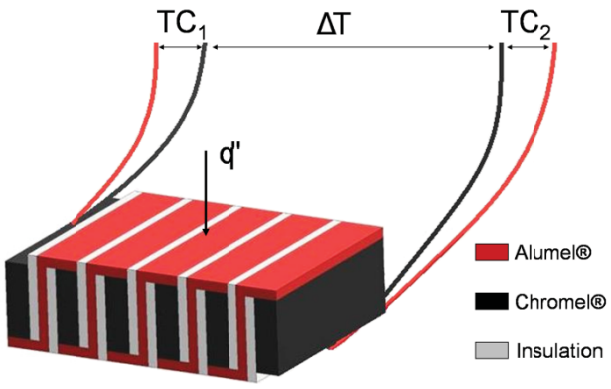

Fig. 5.8 HTHFS design overview. Thermopile use to measure temperature drop across calibrated thermal resistance.

The HTHFS was tested using two backing conditions; water cooled and insulated. The testing was performed in a stagnating jet convection stand which was fully characterized by Gifford et al. (Gifford, Hoffie et al. 2009). This stand, shown in Fig. 5.9, consists of a fully adjustable T-nozzle which directs a 6mm diameter jet of heated air at both the test sensor and a Vatell Corp. HFM-7® reference sensor located 14 diameters away. The HFM is a differential sensor which measures both heat flux and surface temperature and has a time response faster than 100 kHz (Holmberg and Diller 1995), but it can only be used on high conductivity materials. The jet velocity was measured at the sensor location with a pitot-static tube and was found to be 55 +/- 2 m/s. By switching an HFM from one side to the other of the calibration stand, the heat transfer coefficient on each side of the T-nozzle was shown to be identical to within approximately 3% at the stagnation point. Because the hot free jet entrains ambient air and cools before it reaches the sensor location, the jet recovery temperature (T_r) at the sensor location is needed. Recovery temperatures were measured by 36 gauge type K thermocouples which were stretched 1mm above the stagnation point. The recovery temperatures relative to room temperature (T_r-T_∞) from one side to the other were identical to within 4%. It was verified that the thermocouples were measuring the recovery temperature by allowing the HTHFS to reach steady state on an adiabatic backing. The discrepancy between the thermocouple's recovery temperature and the HTHFS's recovery temperature was less than 0.5ºC.

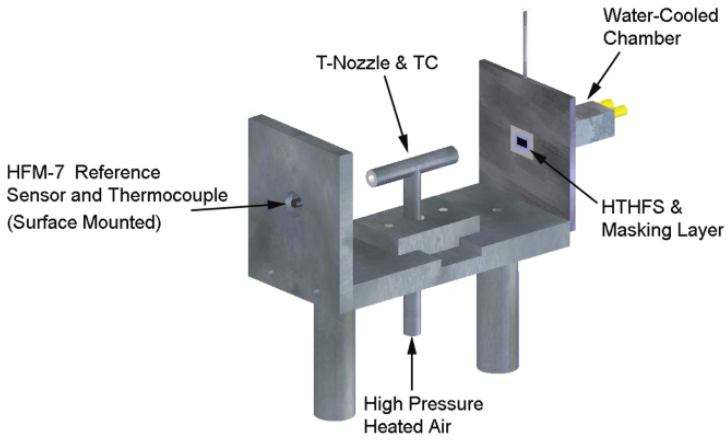

Fig. 5.9 Stagnation flow convection calibration facility. T-nozzle produces symmetric stagnating jets on test sensor and reference sensor.

Using the heat flux and surface temperature measured by the HFM with the measured jet recovery temperature, the convective heat transfer coefficient was calculated.

$$h = \frac{q''_{HFM}}{T_r - T_{S_{HFM}}} \tag{5.14}$$

The heat transfer coefficient is shown as a function of time in Fig. 5.10 and is constant on the mean to within 2% throughout the test. With the convective heat transfer coefficient determined, the heat flux to the test sensor was calculated using the recovery temperature and the measured surface temperature of the HTHFS.

$$q''_{HTHFS} = h\left(T_r - T_{S_{HTHFS}}\right) - q''_{Radiation} \tag{5.15}$$

The radiation term was included to account for any net radiation leaving the sensor face. Since the HTHFS is painted using Krylon™ ultra flat-black spray paint, the emissivity was assumed to be 0.97 (Kidd 1983). The surroundings were treated as a black body at room temperature. For all tests, the radiative flux was less than 2% of the convective flux indicating that a more thorough radiation analysis would not significantly affect the results.

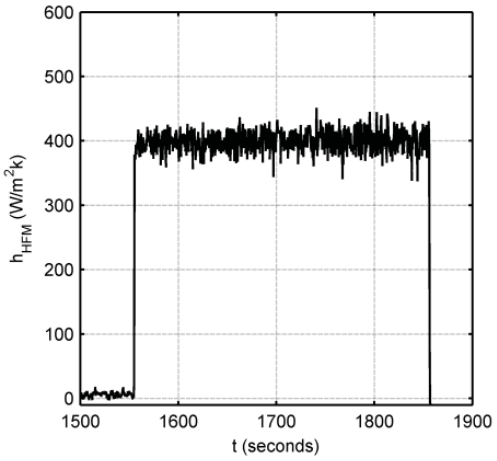

Fig. 5.10 Convective heat transfer coefficient measured by the HFM reference sensor.

The calculated heat flux is shown with the output of the HTHFS in Fig. 5.11 through Fig. 5.14. Fig. 5.11 shows the response of the sensor operated as a differential sensor, a slug calorimeter, and using the HHF method while mounted on a water cooled backing. The limitations of the slug calorimeter and differential sensor are obvious. Since the backing is water cooled, this represents the best case scenario for a differential sensor. Although the differential method performs well at steady-state, it has a slow time response. The slug calorimeter does not give an accurate measurement and as the sensor reaches steady-state, the slug calorimeter's output trends to zero. This is as expected and demonstrates why slug calorimeters cannot be used on conductive materials or to measure steady-state heat fluxes. The HHF method eliminates these problems and performs just as predicted numerically (Fig. 5.5). The HHF has the fast time response of the slug calorimeter, and then trends to the steady-state heat flux more quickly than the differential sensor.

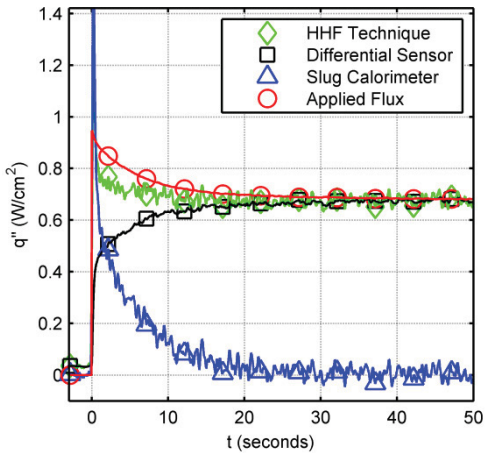

Fig. 5.11 Sensor response on water cooled backing with applied flux shown.

Fig. 5.12 shows the same test as Fig. 5.11 except the HHF_2 method was applied. As expected, the overshoot at the beginning of the test is eliminated for the HHF_2 method at the expense of a slower response time. As predicted in Fig. 5.6, an accurate measurement of the steady-state heat flux is still made.

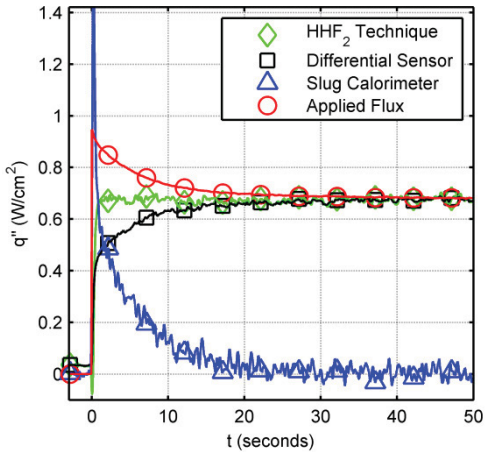

Fig. 5.12 Sensor on water cooled backing using only T_2 in slug and hybrid methods.

Fig. 5.13 and Fig. 5.14 show the response of the sensor mounted on a block of low conductivity, fibrous alumina insulation. Here the curves appear much different than for the water cooled case. In this test, the heat flux quickly trends to zero. This is because the HTHFS surface temperature quickly warms to the recovery temperature since very little heat leaves the sensor. Therefore, the temperature difference driving the heat flux trends to zero causing the heat flux to trend to zero. Although the test

time is short, the advantages of the HHF method are still apparent. This time, the differential sensor is unable to accurately measure the heat flux. This is because q_2" is much less than q_1" which implies that the average of q_2" and q_1" is not an accurate measure of q_1". On the other hand, since q_2" is small, the slug calorimeter works relatively well in this case. As stated previously, in the limit as the backing material becomes a perfect insulator, the HHF method and the slug calorimeter will give identical results once the temperature profile is fully developed. Therefore, for any real insulator with non-zero thermal conductivity, the HHF method will outperform the slug calorimeter. This is shown in Fig. 5.13. Even on this very low conductivity substance, there is still enough heat leaving the back surface of the sensor that the HHF method more accurately measures the heat flux compared to the slug calorimeter.

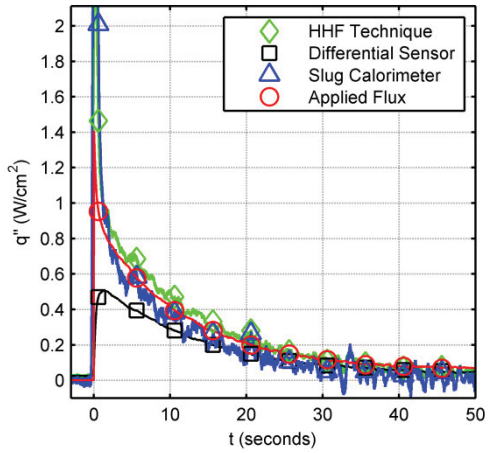

Fig. 5.13 Sensor response mounted on a thermal insulator with applied flux shown.

Fig. 5.14 shows the same test as Fig. 5.13 except only T_2 is used in the slug and hybrid analysis. Once again, the HHF_2 method accurately measures the heat flux with a much smaller initial overshoot. Here it is more difficult to see any slower time response. This is reasonable because, as shown in Fig. 5.6, as the backing material thermal conductivity is reduced, the time response of the HHF_2 improves. More experimentation is needed to fully examine the time response characteristics of sensors utilizing the various forms of the hybrid method.

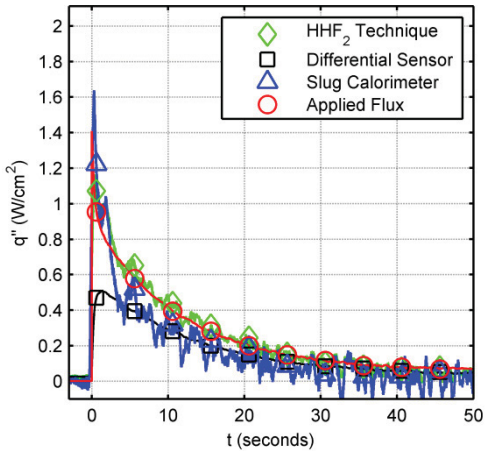

Fig. 5.14 Sensor on insulated backing using only T_2 in slug and hybrid methods.

5.8 Conclusions

This paper outlines a hybrid method for obtaining surface heat flux measurements. It is shown that by combining both spatial and temporal temperature measurements in a hybrid method, the time response and accuracy of heat flux sensors can be improved. More importantly, the HHF method causes the sensor's response to be much less dependent on the properties of the material to which it is mounted. In addition, it is shown that by adjusting how the temperatures used in the HHF method are weighted, the method can be specifically tailored to a particular test. The HHF method was validated by performing numerical simulations which were supported by experimentation. These results show significant improvements compared to operating the sensor as solely a spatial or temporal heat flux sensor.

5.9 Acknowledgments

The authors would like to acknowledge the support of NASA Dryden Flight Research Center through Tao of Systems Integration Inc. and contract monitor Larry Hudson.

6 Conclusions and Recommendations for Future Work

6.1 Conclusions

Several important conclusions made in this dissertation are worth reiterating. In chapter 2, it was shown that a vortex causes a large increase in convection in areas where fluid is being forced through the boundary layer towards the heated surface. Areas where fluid is swept along the surface or pulled from the surface experienced far smaller levels of convection. It was hypothesized that the resulting convection was due to conduction to the fluid and that the magnitude was a function of how long fluid heated within the thermal boundary layer prior to reaching the surface. This indeed appears to be the case as evidenced by the success of a mechanistic model based on this premise. The model was able to accurately predict the time-resolved convection across a range of vortex strengths taking only the transient properties of the vortices as inputs. These findings were further validated in chapter 3 by applying the mechanistic model to the vortices found in the stagnation region of a flow containing large-scale freestream turbulence. Again, the experimental measurements showed that even when multiple vortices are present, the large spikes in convection occur where vortices force fluid from the freestream to the surface. It was shown that the model was able to accurately predict the time-resolved convection when vortices dominated the local flow field. Since all that is required from the flow field is the location and properties of the coherent structures, the model can provide computationally cheap results if combined with a technique such as large eddy simulation (LES).

The THeTA, whose design, fabrication, and evaluation is described in chapter 4, represents a valuable tool for future convection research. In addition to measuring heat flux, the THeTA also measures the time-resolved surface temperature at all of its sensing locations which allows the time-resolved heat transfer coefficient to be mapped on a surface. Furthermore, since the THeTA is made on a flexible polymide film, it can be mounted onto curved surfaces such as cylinders and airfoils. This capability makes the THeTA much more practical than plug type sensors which must be mounted within the test article and should make the THeTA and attractive option for future convection research.

Finally, the HHF method reported in chapter 5 represents a large advance in heat flux measurement technology. Traditionally, heat flux sensors could only acquire usable measurements on materials which had a high thermal conductivity and therefore provided a good heat sink. Utilizing the hybrid method,

this is no longer the case. Differential style sensors can now operate on any material and still provide accurate measurements. The hybrid method has an additional benefit in that it also significantly increases the temporal response of differential heat flux sensors. This ability was utilized in chapters 2 and 3 to significantly increase the temporal capabilities of the THeTA.

6.2 Recommendations for Future Research

There are several areas in which work must continue to more fully understand the basic physics governing the mechanism by which heat transfer is augmented by freestream turbulence. One of the most obvious yet more challenging recommendations is to repeat the experiments in air since air is the fluid in which the vast majority of these problems arise. Besides changing the time scale in which the experiments must be performed, the largest affect is due to the change in Prandtl number from approximately 5 to less than 1. This in turn will cause the thickness of the thermal boundary layer to increase relative to the momentum boundary layer. Since the model makes certain assumptions about the velocity profile within the thermal boundary layer, a change in the ratio δ_T/δ could dramatically influence the model's behavior. Performing the vortex ring experiment in air might be a good first step to uncover how the Prandtl number influences the model as the complication of multiple vortices could again be avoided.

If the stagnation experiments are ever repeated in the water tunnel, several changes could be made to improve and expand the experimental results. First, it would be beneficial if more grids were constructed to give a larger range in turbulence length scales, specifically on the smaller side. Previous work has predicted that there is an optimal length scale where the augmentation reaches a maximum and any change either larger or smaller will result in less convection. Currently, the smallest grid produces the largest augmentation so it is unclear whether this condition has been reached. It would be interesting to study how this affects the vortices which form since no previous work has reported on this. Also, the magnification of the camera should be increased if possible to better resolve the flow field within the boundary layer. One possibility would be to use two cameras, one with a low magnification to capture the large structure, and a second with a much higher magnification to capture the simultaneous near-wall flow. These measurements could validate the assumptions of the velocity profile within the boundary layer.

Following the recommendation above, it is also recommended that any future THeTA sensors be fabricated such that their spatial resolution is higher. The THeTA used above was a prototype gage and

was fabricated with inner sensor spacing of ¼". While this is sufficient, more resolution would aid in the study of some of the smaller vortices that form near the surface, especially if a smaller grid is used. By refining the spot welding procedure, it should be a simple matter to double the spatial resolution of the THeTA.

In the vortex ring experiment reported in chapter 2, a single bore diameter was tested and the vortex ring properties were controlled by varying the stroke length and velocity. It is recommended that instead of changing the stroke length, the bore diameter be changed. The size of the vortex ring created is much more sensitive to the bore diameter than stroke length and so a larger range of vortex parameters could be tested in the same number of tests. This could then be used to better show that no matter the size of the vortex, as long as its circulation and location are known, then the resulting convection can be accurately predicted.

7 Appendix

This appendix contains additional information which would aid any individual who attempts to duplicate or expand upon the experimental work presented herein.

7.1 Experimental details of the vortex ring experiment

The vortex rings described in chapter 2 were produced using a tank of compressed air as the driving force. The test matrix consisted of tests at tank pressures of 10, 20, 30, and 40 psi. During processing, the 30 and 40 psi test cases were thrown out for several reasons. First, the vortex rings were turbulent upon reaching the plate and it was desired to study a laminar ring. Second, the vortex rings interacted with the surface so quickly that the THeTA lacked the temporal resolution to capture the event. Finally, the circulation of the vortices was far larger than anything observed in the stagnation experiments. Therefore, the 30 and 40 psi tests were replaced with two later tests conducted at 5 and 7.5 psi. All the tests reported were conducted at a stroke length equal to 1.5 orifice diameters except for test number three which was performed at a stroke length of 2.5 diameters. The 5 and 7.5 psi tests were never performed at any value except 1.5 and there was an error in the heat flux measurements which occurred during the 20psi 2.5 diameters test. Table 7.1 summarizes the specific parameters used in the vortex ring experiment. The predicted circulation values were calculated based on a correction of the slug flow model which used the time-history of the piston location from the shadowgraph measurements. The vortex propagation velocity (U) was found by tracking the vortex locations in the TRDPIV measured velocity fields prior to their reaching the plate.

Table 7.1 Summary of test conditions used in vortex ring experiment

Test	Pressure	L/D	$\Gamma_{measured}$ (cm^2/s)	$\Gamma_{predicted}$ (cm^2/s)	U (cm/s)
1	5	1.47	24	20	5.3
2	7.5	1.56	42	32	8.8
3	10	2.52	45	49	8.4
4	10	1.65	49	49	9.9
5	20	1.97	80	98	19.1

7.2 Details of the fabrication of the THeTA

After several attempts, the following was found to be a repeatable procedure for fabricating the THeTA. While by no means perfect, it should be used as a starting point for future attempts.

1) Cut copper, constantan, and Kapton to required shape
    a) Kapton should be 4”X4” with at least one perfectly straight edge
    b) Crease copper from 4”X5” to 4”X2.5”
    c) Cut in jig with roller knife with final cut separating two halves
    d) Cut ends all from one side down to 1/16” from 3/16”
2) Clean materials, wear latex gloves from here on
    a) Use acetone and isopropyl
3) Align copper and constantan in welding jig (acrylic fixture with holes at welding locations)
    a) Ensure constantan is centered
    b) Ensure copper is symmetrical
    c) Copper should be above constantan and closer to the smaller of the two jigs
4) Weld junctions
    a) Tungsten electrode on copper, copper electrode on constantan
    b) Copper against positive electrode
    c) Tungsten electrode is on top and positive since copper faces up
    d) For the single constantan-constantan junction use both copper
5) Solder leads
    a) Copper to copper, con to con
    b) Flux should be removed immediately with acetone and isopropyl
    c) Cut copper to separate leads

Gage encapsulation

6) Prepare hot press and Mylar
    a) Construct Teflon pyramid
7) Place long piece of Mylar (5X9) on a piece of Teflon
    a) Tape (use Kapton tape) corners so that mylar is taught
    b) Apply thin layer of epoxy
8) Carefully removed welded foils from jig and invert on Mylar
    a) Apply a thin layer of epoxy on metals (foils should now be covered on both sides)
        i) This step also serves to flatten foils with foam brush

b) Align Kapton on foils ensuring that straight edge is aligned with constantan centerline
c) Tape Kapton down so it remains in correct location
    i) Especially the two corners of the fold
d) Remove tape from far end of Mylar and carefully fold sensor over
    i) A straight ruler edge might be required to start crease
e) Roll to improve crease and remove bubbles starting at fold line and working towards wires

9) Hot press in a t-shirt press
    a) 325 F for 4-8 hours

7.3 Experimental validation of the HHF method

In the original paper (chapter 5), the HHF method was experimentally validated by subjecting it to a step change in convective flux. At the time, no radiation calibration facility existed in the lab and this was used as an acceptable alternative. However, one of the reviewers of the paper said it would be a much better comparison to the numerical work if a radiation comparison was performed. Since the completion of the HHF work, the halogen lamp calibration system was designed and fabricated and has since been used to characterize a number of sensors. As a standard procedure, the HHF response of differential sensors is determined using this facility as demonstrated by the TheTA sensor in Fig. 4.13. The following will show and discuss the figure that *should* have gone into the published HHF paper.

In the fall of 2009, our group was contracted to develop a plug style high temperature heat flux sensor (HTHFS) for a test in the arc jet at NASA's Ames research laboratory. As part of our work, we were to fully calibrate the sensor in radiation and determine its HHF response. This was done by subjecting the sensor to a step change in incident radiation. Values of the applied heat flux ranged from 0.5 to 5W/cm^2. The differential response was easily calibrated at steady state using standard methods. Once this was accomplished, the HHF response was calibrated by using a least squares approach to obtain the thermal mass per unit area ($\rho C\delta$). The response of the sensor is shown in Fig. 7.1. Here, 6 tests are shown overlaid and normalized by the applied heat flux, q''_{in}. Here, the sensor behaves exactly as expected and predicted by Fig. 5.5 and truly demonstrates the advantage of operating a sensor using the HHF method. Note that the HHF has a 95% response in just 0.251 seconds compared with over 4 seconds for the differential response. As expected, since the sensor is heat sunk and quickly approaches a steady state, the slug response is completely unusable.

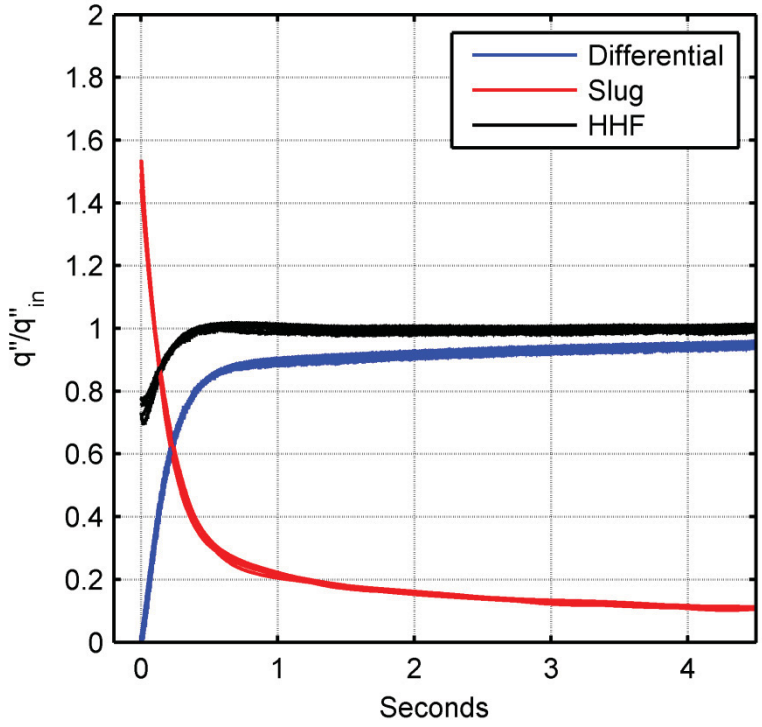

Fig. 7.1 Differential, slug, and HHF response of sensor to step radiation flux. Results of 6 tests overlaid and normalized by the applied heat flux.

7.4 Computational codes

7.4.1 Vortex ring analysis

```
%%Written by David Hubble 2-15-10
%%this code reads in the heat flux and TRDPIV data after it has been
%%through the POD code and allows for easy viewing. This code was also used
%%to make the tifs that made the movies shown in my dissertation defense
clc;clear all;close all;
num=4;%pick the test number fromt he list in TEST below
TEST={'05_15_500' '75_15_500' '10_05_500' '10_15_625' '10_25_625' '20_05_625' '20_15_1250'...
    '20_25_1250' '40_15_2000'};
FLUX={'05_15_PIV_1_test_only.mat' '75_15_PIV_1_test_only.mat' '10_05_PIV_1_test_only.mat'...
    '10_15_PIV_1_test_only.mat' '10_25_PIV_1_test_only.mat' ...
    '20_05_PIV_1_test_only.mat' '20_15_PIV_1_test_only.mat' '20_25_PIV_1_test_only.mat'...
    '40_15_PIV_1_test_only.mat'};
DPFS=[500 500 500 625 625 625 1250 1250 2000];%double pulsed sample frequency
FS=[250 250 250 250 250 250 250 250 400];%actual TRDPIV sample frequency
Sen=[215 189 293 175 195 203 328 215 190 201];%THeTA senitivity
See=34.3;%Seebeck coefficent
ds=2;%downsample by???
color_max=[20 30 20 25 25 30 55 55 90];%color max used in contours
direc=strcat('W:\Users\dhubble\Hubble\Feb_2010_tests\Vortex\final\',TEST{num},'\PIV\Andy_POD\');
direc2='W:\Users\dhubble\Hubble\Feb_2010_tests\All_heat_flux\Reduced_heat_flux\';
load(strcat(direc2,FLUX{num}));
PIVstop=find(abs(a(22,:))>.1,1,'last');%a noise spike could really mess this up!
PIVstart=round(PIVstop-1000*3270/(2*FS(num)));
t=0:.001:(.001*(PIVstop-PIVstart));
h_co=zeros(10,length(t));
```

```
h_co_plot=h_co;
St=h_co;
dpc=[.066 .066 .089 .067 .070 .07 .06 .05 .05 .07];ss=9;
for j=1:10%%process heat flux signals
    differ=1000*a(j+1,PIVstart:PIVstop)/(Sen(j));
    Ts=1000*(smooth(a(j+11,PIVstart:PIVstop),ss)'/See);
    dT=1000*smooth(a(j+1,PIVstart:PIVstop),ss)'/See;
    Tb=Ts+dT;
    Ta=.5*(Ts+Tb);
    slug=dpc(j)*1000*diff(Ta);slug(length(differ))=0;
    HHF=smooth(differ-.5*slug,2*ss);
    h_co_hhf(j,:)=10000*(HHF'./Ts);
    h_co_dif(j,:)=10000*(differ./Ts);
end
mag=51.9;
vector_spacing=8;
basename='VelsFrame';
tempu=load(strcat(direc,'u',basename,num2str(2),'.mat'),'-ascii');
uvec=tempu';
[J,I]=size(uvec);
numvects_x=I;numvects_y=J;
maxx=(I+2)*vector_spacing*mag/10000;maxy=1280*mag/10000;
[X,Y] = meshgrid(1:1:numvects_x,1:1:numvects_y);
%Calculate physical space vectors for plotting:
XX=X*vector_spacing*mag*100/(10^6);%(cm)
YY=Y*vector_spacing*mag*100/(10^6);%(cm)
gagelocy=.28285:2.54*.25:6;gagelocx=maxx*ones(1,10);
count=1;
Dave=zeros(J,111);
for i=6:2:800%%what frames to look at
    close all
    tempu=load(strcat(direc,'u',basename,num2str(i),'.mat'),'-ascii');
    tempv=load(strcat(direc,'v',basename,num2str(i),'.mat'),'-ascii');
    uuvec=tempv';vvvec=tempu';
    uuvec=(mag*DPFS(num)*uuvec/10000);vvvec=mag*DPFS(num)*vvvec/10000;
    Umag=(uuvec.^2+vvvec.^2).^.5;
    S=4*max(max(Umag))/color_max(num);
    [dudx,dudy,dvdx,dvdy]=gradient_dudxdvdy_order2(uuvec,vvvec,vector_spacing*mag/10000,…
       vector_spacing*mag/10000);
    vort=dvdx-dudy;
    uvec=downsample((downsample(uuvec,ds))',ds)';vvec=downsample((downsample(vvvec,ds))',ds)';
    X=downsample((downsample(XX,ds))',ds)';Y=downsample((downsample(YY,ds))',ds)';
    figure1=figure('Position',[10 35 1400 780]);
    axes1=axes('Parent',figure1,'Position',[0.05 .13 0.4 0.855]);box('on');hold('all');tcolor=[.7
.7 .7];
    hold on;
    ddd=colormap(jet);
    ddd(31:34,:)=ones(4,3);
    dfin=cat(1,ddd(1:25,:),ddd(31:34,:),ddd(40:64,:));
    dfin(30:34,3)=[.90 .8 .6 .4 .2];
    dfin(21:25,1)=fliplr([.90 .8 .6 .4 .2]);
    mycmap=dfin;
    set(gcf,'Colormap',mycmap);
    %     patch([maxx maxx+.15 maxx+.15 maxx],[0 0 maxy maxy],[.5 .5
.5]);%xlabel('cm');ylabel('cm');
    %     [cc,hh]=contourf(XX,YY,uuvec,-
1*color_max(num):(2*color_max(num))/100:color_max(num));hold all;caxis([-1*color_max(num)
color_max(num)]);
    %     [cc,hh]=contourf(XX,YY,vvvec,-
1*color_max(num):(2*color_max(num))/100:color_max(num));hold all;caxis([-1*color_max(num)
color_max(num)]);
    %     [cc,hh]=contourf(XX,YY,Umag,-
1*color_max(num):(2*color_max(num))/100:color_max(num));hold all;caxis([-1*color_max(num)
color_max(num)]);
    [cc,hh]=contourf(XX,YY,vort,-
15*color_max(num):(20*color_max(num))/100:15*color_max(num));hold all;caxis([-10*color_max(num)
10*color_max(num)]);%%change limits to +-10X
    set(hh,'EdgeColor','none');hold on;
    hhh = colorbar('peer',gca,'location','WestOutside');
    set(get(hhh,'ylabel'),'String', 'Vorticity (1/s)','FontSize',18);set(gca,'YTick',-
15:5:15,'FontSize',18)
```

```
    quiver(X,Y,uvec,vvec,S,'k');hold on;%ylabel('cm');xlabel('cm');
    plot(gagelocx,gagelocy,'k.','MarkerSize',30);hold on;
    xlim([0 maxx]);
    set(gca,'XTick',-1:17:16);set(gca,'YTick',-1:17:16);
    axes1=axes('Parent',figure1,'Position',[0.5 .080 .45 0.914]);box('on');hold('all');tcolor=[.7
.7 .7];hold on
    XXX=cat(2,t,fliplr(t));
    for j=1:10
        plot(t,4*(j-5)+h_co_hhf(j,:)/h_co_hhf(j,100),'k-','LineWidth',2);hold all
        YYY=cat(2,4*(j-5)+h_co_hhf(j,:)/h_co_hhf(j,100),4*(j-5)+ones(size(t)));
        patch(XXX,YYY,[.85 .85 .85])

    end
    ylim([-19 24.5]);hold on
    plot([i/FS(num),i/FS(num)],[-1000,1e5],'r-
','LineWidth',2);;set(gca,'YTick',0:2:4,'FontSize',18);
    xlim([2 4])
    ylabel('St/St_0','FontSize',20);xlabel('Seconds','FontSize',20)
    h=gcf;set(h,'Color',[1 1 1]);
    %%use to save tifs for movies
    drawnow
    pause(.01)

filename=strcat('W:\Users\dhubble\Hubble\Feb_2010_tests\Vortex\final\',TEST{num},'\Movie\','movie
2_',num2str(i),'.tif');
    F=getframe(gcf);
    junk=frame2im(F);
    imwrite(junk,filename,'tiff');
end

%% Saves daq signal from a txt file to a mat file while also only keeping
%% duration from 2 seconds before the camera started until 10 seconds after
%% which cuts the file size by about 99%
clc;clear all;close all
grid={'lam' 'Grid1' 'Grid2','Grid3'};%test name
test={'3','4','5'};%test number
for gr=1
    for tst=1:2;
        direc='Y:\puddinpop\Hubble\Feb_2010_tests\All_heat_flux\';%location
        load(strcat(direc,'feb6_',grid{gr},'_',test{tst},'_16bit.mat'))
        stop=find(a(22,:)>.2,1,'last');%find end of camera signal
        temp=a(:,stop-20000:stop+10000);
        temp2=zeros(size(temp));
        off=zeros(1,20);
        for i=1:20
            off(i)=mean(a(i+1,1:5000));%get the offset
            temp2(i+1,:)=temp(i+1,:)-off(i);%subtract off offset
        end
        temp2(22,:)=temp(22,:);
        clear a
        a=temp2;
        sname=strcat(direc,'Reduced_heat_flux\feb6_',grid{gr}...
            ,'_',test{tst},'_test_only.mat');
        save(sname,'a')%save as mat file
        clear a temp temp2
    end
end


%%Written by David Hubble 6-11-10
%%this code applies the my model to the vortex data
%%collected in the vortex ring experiment and comapares it to the measured
%%transient convection
clc;clear all;
close all
test={      '05_15_500'      '75_15_500'   '10_05_500'   '10_15_625'   ...
    '10_15_2_625' '10_25_625'   '20_05_625'   '20_15_1250'  '20_15_2_1250'};
test_HF={   '05_15_PIV_1'    '75_15_PIV_1' '10_05_PIV_1' '10_15_PIV_1' ...
    '10_15_PIV_2' '10_25_PIV_1' '20_05_PIV_1' '20_15_PIV_1' '20_15_PIV_2' };
plot_title={'05 15'          '75 15'       '10 05'       '10 15'       ...
    '10 15 2'     '10 25'       '20 05'       '20 15'       '20 15 2'};
```

```
Camera_FS=[  500              500           500           500          ...
    500           500           500           500           500];
Gplot=[24 42 0 49 45 0 0 80 0 0 0 0];


for tst=[6];%test

    direc='W:\Users\dhubble\Hubble\Feb_2010_tests\Vortex\final\';
    vs=8;
    MAG=52;
    Sen=[215 189 293 175 195 203 328 215 190 201];%from laminar data.
    See=34.3;
    load(strcat('W:\Users\dhubble\Hubble\Feb_2010_tests\All_heat_flux\Reduced_heat_flux\'...
        ,test_HF{tst},'_test_only.mat'));
    PIVstop=find(abs(a(22,:))>.1,1,'last');%%a noise spike could really mess this up!
    PIVstart=round(PIVstop-1000*3272/(Camera_FS(tst)));
    t=[0:.001:(.001*(PIVstop-PIVstart))];
    h_co=zeros(10,length(t));h_co_temp=h_co;
    Stanton=h_co;
    h_ave=zeros(10,1);
    q_ave=h_ave;
    dpc=[.066 .066 .089 .067 .070 .07 .06 .05 .05 .07];
    tc=.001*[172 172 208 180 176 174 165 144 121 173];
    ss=35;
    for j=1:10
        differ=1000*a(j+1,PIVstart:PIVstop)/(Sen(j));
        Ts=1000*(smooth(a(j+11,PIVstart:PIVstop),ss)'/See);
        dT=1000*smooth(a(j+1,PIVstart:PIVstop),ss)'/See;
        Tb=Ts+dT;
        Ta=.5*(Tb+Ts);
        slug=dpc(j)*1000*diff(Ta);slug(length(differ))=0;
        HHF=smooth(differ-.5*slug,2*ss);
        h_co(j,:)=10000*(HHF'./Ts);
        Stanton(j,:)=(2000*(j-5)+10000*((a(j+1,PIVstart:PIVstop)/(Sen(j))).\(smooth(a(j+11,...
            PIVstart:PIVstop),51)'/See)))/(.001*1000*.1*4200);%convert to stanton number
    end
    FilmT=36;
    [Visc,den,Pr,k,knu,alpha,C] = fluid_props(FilmT);
    BL=.2;%
    load(strcat(direc,test{tst},'\Vortex\',test{tst},'_MASTER_ARRAY.mat'))
    Sens_y_loc=linspace(3,140,10);
    Sens_x_loc=127;
    time_pred=zeros(num,10);time_pred2=zeros(num,10);time_pred_andy=zeros(num,10);
    X1=Sens_x_loc*vs*MAG/10000;
    X2=X1-BL;
    Var=zeros(10,num);
    dt=2/Camera_FS(tst);
    TIME=start*dt:dt:dt*stop-dt;
    T_Delayed=zeros(10,num);delay=zeros(10,num);
    tmaster=zeros(1,num);DIST=tmaster;
    for frame=1:1:num
        num_vorts=find(VMA(:,1,frame)==0,1,'first')-1;
        tempmat=VMA(1:num_vorts,2:5,frame);
        Xv=tempmat(:,1)*vs*MAG/10000;
        Yv=tempmat(:,2)*vs*MAG/10000;%cm location of vorticies
        G=tempmat(:,3);%Circulation cm^2/s
        Circ1(frame)=-1*min(G);
        Circ2(frame)=max(G);
        if sum(tempmat(:,1))==0
            time_pred(frame,:)=100;
            time_pred_andy(frame,:)=100;
            time_pred2(frame,:)=100;
            T_Delayed(1:10,frame)=TIME(frame);
            dob(frame)=0;
            dba(frame)=0;
            Circ(frame)=0;
            VIND(frame)=0;
        else
            for sens=3:8%only look at center 6 sensors
                Ar=tempmat(:,4);
                Y1=Sens_y_loc(sens)*vs*MAG/10000;%cm
```

```
                d=(((X1-Xv).^2+(Y1-Yv).^2).^.5);%in cm from sensor to vortex center
                Vind=abs(G)./(2*pi*d);%Biot-Savart cm/s at sensor
                Influence=find(Vind==max(Vind));%%find the vortex that induces the largest
velocity at the sensor
                dist_t=d(Influence);%chosen distance, distance to most important vortex
                if Xv(Influence)<.4% get rid of partial vorticies strange circulation
                    time_pred(frame,sens)=100;
                    delay(sens,frame)=0;
                elseif dist_t>50;
                    time_pred(frame,sens)=100;
                    delay(sens,frame)=0;
                else
                    if (Xv(Influence)-X2) > dist_t
                        Y2=Y1;
                    else
                        Len=(4*Ar(Influence)/pi)^.5;
                        top=find(G==min(G));
                        bot=find(G==max(G));
                        if G(Influence) > 0 %if ClockWise
                            Y2=Yv(Influence)+(dist_t^2-(Xv(Influence)-X2)^2)^.5;
                        else %CCW
                            Y2=Yv(Influence)-(dist_t^2-(Xv(Influence)-X2)^2)^.5;
                        end
                    end
                    Uind=sign(G(Influence))*Vind(Influence)*((Y1-Yv(Influence))/dist_t);
                    Circ(frame)=-1*min(G);
                    dob(frame)=dist_t;
                    d3=(BL^2+(Y2-Y1)^2)^.5;
                    dba(frame)=d3;
                    VIND(frame)=Vind(Influence);
                    time_pred(frame,sens)=2*d3/Vind(Influence);
                    delay(sens,frame)=2*BL/Vind(Influence);
                end
            end
        end
        tmaster(frame)=TIME(frame);
        disp(frame)
    end
    h_t=((10000*k./(2.0*(pi*alpha*time_pred).^.5)).^2+500^2).^.5;
    t_plt_mod=start*dt:dt:dt*stop-dt;
    close all
    for sens=[6]%%page 133 in notebook
        figure(100*tst+sens);
        ind=find(h_t(:,sens)==max(h_t(:,sens)));
        tmax=tmaster(ind);
        td=tmaster+delay(sens,:);
        t_temp=td(1:ind);%satisfies t<tmax
        ind2=find(t_temp>tmax+delay(sens,ind));
        h_t(ind2,sens)=NaN;    sts=t(500+find(h_co(sens,500:length(t))>800,1,'first'));
st1=100+find(h_co(sens,100:length(h_co))>800,1,'first');
        plot(t,smooth(h_co(sens,:),15),'k-');xlim([sts-1 sts+1]);;hold all;grid on
        plot(tmaster+delay(sens,:),h_t(:,sens),'r.');ylim(500*[0 5]);ylabel('St/St_0');xlabel('t
(seconds)')
        legend('Measured','Model','Location','NorthWest')
    end
end


%%Written by David Hubble 6-11-10
%%calcualtes the properties of water at a given temperature, FilmT given
%%in C
function [Visc,den,Pr,k,knu,alpha] = fluid_props(FilmT)

Ttable=[273.15 280 290 295 300 305 310 315 320 325]';%(K)
ktable=[0.569 .582 .589 .606 .613 .620 .628 .634 .640 .645]';%(W/mK)
Prtable=[12.99 10.26 7.56 6.62 5.83 5.20 4.62 4.16 3.77 3.42]';%(ND)
Viscosity=[0.001750 0.001422 0.001080 0.000959 0.000855 0.000769...
    0.000695 0.000631 0.000577 0.000528]';%(Ns/m^2)
specvol=[0.001 0.001 0.001001 0.001002 0.001003 0.001005 0.001007...
    0.001009 0.001011 0.001013]';%(m^3/kg)
Visc=interp1(Ttable(:,1),Viscosity(:,1),(FilmT+273.15));%(Ns/m^2)
```

```
den=1/(interp1(Ttable(:,1),specvol(:,1),(FilmT+273.15)));%(kg.m^3)
Pr=interp1(Ttable(:,1),Prtable(:,1),(FilmT+273.15));%(ND)
k=interp1(Ttable(:,1),ktable(:,1),(FilmT+273.15))/100;%(W/cmK)
knu=((interp1(Ttable(:,1),Viscosity(:,1),(FilmT+273.15)))*...
    (interp1(Ttable(:,1),specvol(:,1),(FilmT+273.15))))*100^2;%(cm^2/s)
alpha=knu/Pr;%(cm^2/s)
```

7.4.2 Stagnating flow analysis

```
%%Adapted from a code by Andrew Gifford by David Hubble
%%This code tracks the vortex strucutres in time and saves them sorted in
%%order of life span
clear all;close all;clc
Grid='Grid3';
test='test3';
slash='\';
direc=strcat('Y:',slash,'puddinpop',slash,'Hubble',slash,'Feb_2010_tests',slash,'Vortex',slash);
%%% VR
maxlen=0;
start=1;
stop=3269;
load([direc,'Final',slash,'10_25_625',slash,'Vortex',slash,'10_25_625_MASTER_ARRAY.mat']) %%% VR
vortarray=VMA;
[m,n,p]=size(vortarray);

dist_lim_x=5;%%%how far (in vector spacing) can the vortex move in the x direction
dist_lim_y=5;%%%how far (in vector spacing) can the vortex move in the y direction
Gamma_lim=.2;%%%percent change in circulation
time_lim=2;%%%how long can the vortex dissapear alltogether (in number of frames)

vortcount=0;
count=0;
temp_x_1(1:m)=0;
temp_y_1(1:m)=0;
temp_G_s2(1:m,1:p)=0;
temp_G_s1(1:m)=0;
V_Track=zeros(4000,5);
temp_t_2(1:m,1:p)=0;
temp_x_2(1:m,1:p)=0;
temp_y_2(1:m,1:p)=0;
temp_G_2(1:m,1:p)=0;
temp_G_s2(1:m,1:p)=0;
res_x(1:m,1:p)=0;
res_G(1:m,1:p)=0;
res_y(1:m,1:p)=0;
res_t(1:m,1:p)=0;

%%%This loop creates V_Track. Then each Vortex Track is individually saved
%%%so the number of files created is equal to the number of different
%%%vortex tracks present
for i=1:p-1%For comparison of vortices at time step 1 through time steps p-1
    for j=1:m%For a given time step look at all vortices present
        temp_x_1(j)=(vortarray(j,2,i))';
        temp_y_1(j)=(vortarray(j,3,i))';
        temp_G_s1(j)=sign(vortarray(j,4,i))';
        if temp_x_1(j)~=0 && temp_y_1(j)~=0
                vortcount=vortcount+1;
                orig_vort=vortarray(j,:,i);
            for k=(i+1):1:(p-1)%Look at the next time step after the one your're on and search
till the end..
                    V_Track(1,1:5)=[orig_vort];
                    temp_t_2(:,k)=(vortarray(:,1,k))';
                    temp_x_2(:,k)=(vortarray(:,2,k))';%got to look at every vortex at time k
                    temp_y_2(:,k)=(vortarray(:,3,k))';
                    temp_G_2(:,k)=(vortarray(:,4,k))';
                    temp_G_s2(:,k)=sign(vortarray(:,4,k))';
                    for q=1:m%Must compare with only kept vortices
```

```
                        if temp_x_2(q,k)~=0 && temp_y_2(q,k)~=0
                            res_G=abs((abs(temp_G_2(q,k))-
abs(V_Track(count+1,4)))/V_Track(count+1,4));
                            res_x=abs(((temp_x_2(q,k)-V_Track(count+1,2))));
                            res_y=abs(((temp_y_2(q,k)-V_Track(count+1,3))));
                            res_t=(temp_t_2(q,k)-V_Track(count+1,1));
                            if res_x<=dist_lim_x && res_y<=dist_lim_y && res_t<=time_lim &&
res_G<=Gamma_lim   %temp_G_s2==sign(Master_Array(count+1,4,vortcount))
                                count=count+1;
                                tempvort=[vortarray(q,:,k)];
                                V_Track(count+1,1:5)=[tempvort];
                                vortarray(q,:,k)=0;
                                clear tempvort
                            end
                        end
                    end
            end
            Vortex_Track=zeros(count+1,5);
            count=0;
            pause(0.01)
            for dave=1:4000;
                if V_Track(dave,2)~=0
                    Vortex_Track(dave,:)=V_Track(dave,:);
                end
            end

tempname=strcat(direc,Grid,slash,test,slash,'Vortex',slash,'Vortex_Track',num2str(vortcount),'.ma
t');
            save(tempname,'Vortex_Track')
            disp(['Vortex Track ',num2str(vortcount),' done'])
            clear V_Track
            V_Track=zeros(4000,5);
        end
    end
end

len=zeros(1,vortcount);
for i=1:vortcount
    load([direc,Grid,slash,test,slash,'Vortex',slash,'Vortex_Track',num2str(i),'.mat']);
    len(i)=length(Vortex_Track);
end
[Y,I]=sort(len);%%sorts based on life span
I2=fliplr(I);
Y2=fliplr(Y);
filted=find(Y2<50,1,'first');%%finds only the vortices that lastest more than 50 time steps
MASTER_TRACK=zeros(3270,5,filted);
count=1;
for i=I2(1:filted)%%saves in order or life span
    load([direc,Grid,slash,test,slash,'Vortex',slash,'Vortex_Track',num2str(i),'.mat']);
    [r,c]=size(Vortex_Track);
    MASTER_TRACK(1:r,:,count)=Vortex_Track;
    count=count+1;
end
tempname=strcat(direc,Grid,slash,test,slash,'Vortex',slash,'MASTER_TRACK_ARRAY.mat');
save(tempname,'MASTER_TRACK','Y2','I2')

%% Written by David Hubble 3-2-10
%% apply vortex model to vortices in stagnating flow
clc;clear all;close all
%                 1    2    3    4    5    6    7
Number=[4];%1-7%%G1T3,G1T4,G1T5,G2T3,G2T4,G3T3,G3T4

vs=8;%vecotr spacing in TRDPIV
MAG=52;%magnification um/pixel
folder={'Grid1','Grid2','Grid3','Lam'};
test={'1' '2' '3','4','5'};
direc='W:\Users\dhubble\Hubble\Feb_2010_tests\Stagnation\';
tests=[1 1 1 2 2 3 3 4;3 4 5 3 4 3 4 1];
name=strcat(folder{tests(1,Number)},' test ',test{tests(2,Number)});
Sen=[215 189 293 175 195 203 328 194 190 201];%THeTA sensitivity
See=34.3;
```

```
load(strcat('W:\Users\dhubble\Hubble\Feb_2010_tests\All_heat_flux\Reduced_heat_flux\feb6_'...
    ,folder{tests(1,Number)},'_',test{tests(2,Number)},'_test_only.mat'));
PIVstop=find(abs(a(22,:))>.1,1,'last');%%a noise spike could really mess this up!
PIVstart=round(PIVstop-1000*3272/(250));
t=0:.001:(.001*(PIVstop-PIVstart));
h_co=zeros(10,length(t));
Stanton=h_co;
h_ave=zeros(10,1);
q_ave=h_ave;
dpc=[.066 .066 .089 .067 .070 .07 .06 .05 .05 .07];
ss=15;

for j=1:10
    differ=1000*a(j+1,PIVstart:PIVstop)/(Sen(j));
    Ts=1000*(smooth(a(j+11,PIVstart:PIVstop),ss)'/See);
    dT=1000*smooth(a(j+1,PIVstart:PIVstop),ss)'/See;
    Ta=Ts+.5*dT;
    slug=dpc(j)*1000*diff(Ta);slug(length(differ))=0;
    HHF=smooth(differ-0*.5*slug,2*ss);
    h_co(j,:)=10000*(HHF'./Ts);
    Stanton(j,:)=(2000*(j-5)+10000*((a(j+1,PIVstart:PIVstop)/(Sen(j)))./...
        (smooth(a(j+11,PIVstart:PIVstop),51)'/See)))/(.001*1000*...
        .1*4200);%divide by den*vel*Cp .001 gets in between 0 and 10
    h_ave(j)=round(mean(h_co(j,:)));
    q_ave(j)=mean(1000*a(j+1,:)/Sen(j));
end
FilmT=36;
[Visc,den,Pr,k,knu,alpha,C] = fluid_props(FilmT);
BL=2.4*(knu/.98)^.5%cm a=.98
BL=BL*Pr^-.4%thermal boundary layer
load(strcat(direc,folder{tests(1,Number)},'\test',test{tests(2,Number)},...
    '\Vortex\test',test{tests(2,Number)},'_MASTER_ARRAY_CI.mat'));
Sens_y_loc=linspace(140,3,10);%1-10 1 is top 10 is bottom OPPOSITE FOR VRE!!
Sens_x_loc=123;
time_pred1=ones(num_POD,10);
time_pred2=ones(num_POD,10);
X1=Sens_x_loc*vs*MAG/10000;
X2=X1-BL;
TIME=.004:.004:.004*num_POD;
T_Delayed=zeros(10,num_POD);
min_time_master=zeros(num_POD,10);
vind_master=zeros(num_POD,10);
for frame=1:num_POD
    num_vorts=find(VMA(:,1,frame)==0,1,'first')-1;
    tempmat=VMA(1:num_vorts,2:5,frame);
    if sum(tempmat(:,1))==0
        time_pred1(frame,:)=100;
        time_pred2(frame,:)=100;
    else
        for sens=3:8
            Y1=Sens_y_loc(sens)*vs*MAG/10000;%cm
            Xv=tempmat(:,1)*vs*MAG/10000;Yv=tempmat(:,2)*vs*MAG/10000;%cm location of vorticies
            d=(((X1-Xv).^2+(Y1-Yv).^2).^.5);%in cm from sensor to vortex center
            G=tempmat(:,3);%Circulation cm^2/s
            Vind=abs(G)./(2*pi*d);%Biot-Savart cm/s at sensor
            circ(frame)=min(G);
            circ2(frame)=max(G);
            Y2=zeros(num_vorts,1);
            for ii=1:num_vorts
                if G(ii) > 0 %if CW
                    Y2(ii)=Yv(ii)+(d(ii)^2-(Xv(ii)-X2)^2)^.5;
                else %CCW
                    Y2(ii)=Yv(ii)-(d(ii)^2-(Xv(ii)-X2)^2)^.5;
                end
            end
            d3=(BL.^2+(Y2-Y1).^2).^.5;
            t_temp=2*d3./Vind;MET=abs(G)./(2*pi*d.^2);
            maybe=sum(1./t_temp)^-1;%adding the inverse of all times together.
            INFL=find(Vind==max(Vind));%%find the vortex that induces the largest velocity at the
sensor
            vind_master(frame,sens)=INFL;
```

```
            dist_t=d(INFL);%chosen distance, distance to most important vortex
            met2=1/(sum((1./t_temp)));
            min_time_master(frame,sens)=find(t_temp==min(t_temp));
            time_pred1(frame,sens)=min(t_temp);%%use vortex that causes minimum estimateed time
through BL
            time_pred2(frame,sens)=t_temp(find(Vind==max(Vind)));%%use vortex that induces
largest velocity
            T_Delayed(sens,frame)=TIME(frame)+.0+(2*BL/Vind(INFL));
        end
    end
    disp(frame)
end

t_plt_mod=0:.004:.004*num_POD-.004;
h_t1=10000*k./(2.*(pi*alpha*time_pred1).^.5);
h_t2=10000*k./(2.*(pi*alpha*time_pred2).^.5);

H_T1=zeros(num_POD,10);
H_T2=zeros(num_POD,10);
for i=1:10
    H_T1(:,i)=(smooth(h_t1(:,i),1).^2+755^2).^.5;
    H_T2(:,i)=(smooth(h_t2(:,i),1).^2+755^2).^.5;
end
mint=mean(mean(H_T1))
maxV=mean(mean(H_T2))
Stb=.1*1000*4200*.001;%divide h by this to get St
close all
ds=1;
for sens=[3]
    figure(1*sens)
    plot(downsample(t_plt_mod,ds),downsample(H_T2(:,sens),ds)/Stb,'r.');hold all;grid on
    plot(downsample(T_Delayed(sens,:),ds),downsample(H_T2(:,sens),ds)/Stb,'b.');hold all;grid on
    plot(downsample(t_plt_mod,ds),downsample(H_T1(:,sens),ds)/Stb,'g.');hold all;grid on
    plot(t,h_co(sens,:)/Stb,'k-');ylim([0 2000/Stb]);
    xlabel('Seconds');
    ylabel('St (1e-3)');
    plot([0 14],[757/Stb 757/Stb],'g-');set(gca,'YTick',0:1:4);
    legend('Model','Measured','Laminar')
    xlim([0 13.5])
end



%%written by David Hubble fall 2010
%%makes a variety of plots shown in chapter 3 of dissertation
clear all
close all
clc
% %After Vortex_tracking_dave, loads in a large matrix containing all
% vortex tracks sorted from longest to shortest.
Number=[4];%1-7%%G1T3,G1T4,G1T5,G2T3,G2T4,G3T3,G3T4
vs=8;
MAG=52;
folder={'Grid1','Grid2','Grid3','Lam'};
test={'1' '2' '3','4','5'};
direc='W:\Users\dhubble\Hubble\Feb_2010_tests\Stagnation\';
tests=[1 1 1 2 2 3 3 4;3 4 5 3 4 3 4 1];
name=strcat(folder{tests(1,Number)},' test ',test{tests(2,Number)});
Sen=[215 189 293 175 195 203 328 194 190 201];%from laminar data.
See=34.3;
load(strcat('W:\Users\dhubble\Hubble\Feb_2010_tests\All_heat_flux\Reduced_heat_flux\feb6_'...
    ,folder{tests(1,Number)},'_',test{tests(2,Number)},'_test_only.mat'));
PIVstop=23001;
PIVstart=6913;
t=0:.001:(.001*(PIVstop-PIVstart));
h_co=zeros(10,length(t));
Stanton=h_co;
h_ave=zeros(10,1);
q_ave=h_ave;
dpc=[.066 .066 .089 .067 .070 .07 .06 .05 .05 .07];
```

```
ss=25;
for j=1:10
    differ=1000*a(j+1,PIVstart:PIVstop)/(Sen(j));
    Ts=1000*(smooth(a(j+11,PIVstart:PIVstop),ss)'/See);
    dT=1000*smooth(a(j+1,PIVstart:PIVstop),ss)'/See;
    Ta=Ts+.5*dT;
    slug=dpc(j)*1000*diff(Ta);slug(length(differ))=0;
    HHF=smooth(differ-0*.5*slug,2*ss);
    h_co(j,:)=10000*(HHF'./Ts);
    Stanton(j,:)=(2000*(j-
5)+10000*((a(j+1,PIVstart:PIVstop)/(Sen(j))./(smooth(a(j+11,PIVstart:PIVstop),51)'/See)))/(.001*
1000*.1*4200);%divide by den*vel*Cp .001 gets in between 0 and 10
    h_ave(j)=round(mean(h_co(j,:)));
    q_ave(j)=mean(1000*a(j+1,:)/Sen(j));
end
num_POD=3270;
stop=num_POD;
vs=8;
MAG=52;
FilmT=36;
[Visc,den,Pr,k,knu,alpha] = fluid_props(FilmT);
BL=2.4*(knu/.98)^.5;%cm a=.98
BL=BL*Pr^-.4;%thermal boundary layer
Sens_x_loc=123;
time_pred1=ones(num_POD,10);
time_pred2=ones(num_POD,10);
X1=Sens_x_loc*vs*MAG/10000;
X2=X1-BL;
load(strcat(direc,folder{tests(1,Number)},'\test',test{tests(2,Number)},'\Vortex\MASTER_TRACK_ARR
AY.mat'))
[r,c,a]=size(MASTER_TRACK);
Sens_y_loc=linspace(140,3,10);
TIME=1e9*ones(num_POD,a,10);TIME2=TIME(:,:,3);
len_vect=Y2;clear Y2
Vind_t=zeros(r,15);t_t=zeros(r,15);d_t=zeros(r,15);circ_t=zeros(r,15);d3_t=zeros(r,15);tmod_t=zer
os(r,15);
for track=[1 3 4 5 6 7 8 9 10 11 12 13 14 15 16 17 18 19 20]%what tracks to look at
    for sens=3
        track_len=find(MASTER_TRACK(:,1,track)==0,1,'first')-1;
        Y1=Sens_y_loc(sens)*vs*MAG/10000;%cm
        Xv=MASTER_TRACK(:,2,track)*vs*MAG/10000;
        Yv=MASTER_TRACK(:,3,track)*vs*MAG/10000;%cm location of vorticies
        d=(((X1-Xv).^2+(Y1-Yv).^2).^.5);%cm from sensor to vortex center
        G=MASTER_TRACK(:,4,track);%Circulation cm^2/s
        Vind=abs(G)./(2*pi*d);%Biot-Savart cm/s at sensor
        Y2=zeros(num_POD,1);
        for ii=1:num_POD
            if G(ii) > 0 %if CW
                Y2(ii)=Yv(ii)+(d(ii)^2-(Xv(ii)-X2)^2)^.5;
            else %CCW
                Y2(ii)=Yv(ii)-(d(ii)^2-(Xv(ii)-X2)^2)^.5;
            end
        end
        d3=(BL.^2+(Y2-Y1).^2).^.5;
        t_temp=2*d3./Vind;
        t_d=BL./Vind;
        circ_t(:,track)=G;
        d_t(1:track_len,track)=smooth(d(1:track_len),15);
        Vind_t(:,track)=Vind;
        t_t(1:track_len,track)=MASTER_TRACK(1:track_len,1,track);
        d3_t(1:track_len,track)=smooth(d3(1:track_len),15);
        tmod_t(1:track_len,track)=smooth(t_temp(1:track_len),15);
        TIME(MASTER_TRACK(1:track_len,1,track),track,sens)=t_temp(1:track_len);
        TIME2(MASTER_TRACK(1:track_len,1,track),track)=t_d(1:track_len);
    end
    disp(strcat(num2str(track),'_of_',num2str(a)))
end
t_plt_mod=0:.004:.004*num_POD-.004;
t4=min(TIME(:,[5 11 14],3),[],2);track_4=sqrt((10000*k./(2*(pi*alpha*t4).^.5)).^2+755^2);
td2=min(TIME2,[],2)';
plot(t_plt_mod(2457:end),smooth(track_4(2457:end),1)/755,'r.','MarkerSize',10);hold all;hold all;
```

```
plot(t,h_co(3,:)/755,'k-');ylim([0 2.5]);xlim([3 16])
legend('Model','Measured','Location','SouthWest')
t3=min(TIME(:,:,3),[],2);track_3=sqrt((10000*k./(2*(pi*alpha*t3).^.5)).^2+755^2);plot(t_plt_mod,s
mooth(track_3,5)/755,'r.','MarkerSize',4)
plot(t,h_co(3,:)/755,'k-');ylim([0 2.5]);xlim([3 16])
plot(t_plt_mod+td2,smooth(track_3,5)/755,'g.','MarkerSize',4)
close all
sen=sens;
figure(sen)
plot(t,h_co(sen,:),'k-');ylim([0 2300]);hold all
for track=1:15
    track_pred=sqrt((10000*k./(2*(pi*alpha*TIME(:,track,sen)).^.5)).^2+755^2);
    plot(t_plt_mod,track_pred,'.');hold all
end
%% look at vortex tracks (This replaces the oct 26th code and does a better job)
skip=0; %%only do this section if skip == 1
if skip==1
    track_number=1;
    sensors=[2:4];
    temp_props=MASTER_TRACK(:,:,track_number);
    stop=find(temp_props(:,1)==0,1,'first')-1;
    xv=smooth(temp_props(1:stop,2),35);
    yv=smooth(temp_props(1:stop,3),35);
    Circ=smooth(temp_props(1:stop,4),35);
    figure
    I=125;J=157;
    maxx=(I+2)*8*52/10000;maxy=52/10000*1280;gagelocy=.28285:2.54*.25:6;gagelocx=maxx*ones(1,10);
    ddd=colormap(jet(128));
    for ii=1:10:length(xv)
        CC=ceil(ii*128/length(xv));

plot(8*52/10000*xv(ii),8*52/10000*yv(ii),'ko','MarkerSize',.01+4*abs(Circ(ii)),'MarkerEdgeColor',
'k','MarkerFaceColor',ddd(CC,:));hold all
        text(8*52/10000*xv(ii),8*52/10000*yv(ii),num2str(ii))
        hold all
    end
    time=[temp_props(1,1) temp_props(1,1)+range(temp_props(1:stop,1))]/250;
    patch([maxx maxx+.15 maxx+.15 maxx],[0 0 maxy maxy],[.5 .5 .5])
    plot(gagelocx(1:3),gagelocy(7:9),'k.','MarkerSize',30)
    caxis([0 range(time)])
    xlim([2.5 maxx+.15])
    ylim([3 6])
    set(gca,'XTick',-1:17:16);set(gca,'YTick',-1:17:16);
    axis equal
    colorbar
    figure
    h_plot=h_co(sensors,time(1)*1000:time(2)*1000)/755;
    pt=0:.001:range(time);
    skipper=[250:500:length(h_plot)];
    plot(pt,h_plot(1,:),'k-',pt,h_plot(2,:),'k-',pt,h_plot(3,:),'k-');ylabel('St/St_l_a_m');hold
all

plot(pt(skipper),h_plot(1,skipper),'k^',pt(skipper),h_plot(2,skipper),'k+',pt(skipper),h_plot(3,s
kipper),'ko','MarkerSize',10);ylabel('St/St_l_a_m');hold all
    ylim([0 2.5]);xlim([0 range(time)])
end
%% look at track 11 and 14
skip=0;
if skip==1
    for track_number=[14];
        temp=MASTER_TRACK(:,:,track_number);
        stop=find(temp(:,1)==0,1,'first')-1;
        temp_props=MASTER_TRACK(1:stop,:,track_number);
        xv1=smooth(temp_props(:,2),35,'loess');yv1=smooth(temp_props(:,3),35);
        track_number=11;
        temp=MASTER_TRACK(:,:,track_number);
        stop=find(temp(:,1)==0,1,'first')-1;dstop=stop;
        start=find(temp(:,1)==temp_props(length(temp_props),1));
        temp_props2=temp(start:stop,:);
        xv2=smooth(temp_props2(:,2),35,'loess');yv2=smooth(temp_props2(:,3),35);
        final_props=cat(1,temp_props,temp_props2);
```

```
        xv=cat(1,xv1,xv2);yv=cat(1,yv1,yv2);
        Circ=(final_props(:,4));
        figure(10)
        I=125;J=157;

maxx=(I+2)*8*52/10000;maxy=52/10000*1280;gagelocy=.28285:2.54*.25:6;gagelocx=maxx*ones(1,10);
        ddd=colormap(jet(128));
        for ii=1:8:length(xv)
            CC=ceil(ii*128/length(xv));

plot(8*52/10000*xv(ii),8*52/10000*yv(ii),'ko','MarkerSize',.01+4*abs(Circ(ii)),'MarkerEdgeColor',
'k','MarkerFaceColor',ddd(CC,:));hold all
            hold all
        end
        time=[final_props(1,1) final_props(length(final_props))]/250;
        patch([maxx maxx+.15 maxx+.15 maxx],[0 0 maxy maxy],[.5 .5 .5])
        plot(gagelocx(1:3),gagelocy(7:9),'k.','MarkerSize',30)
        caxis(time)
        xlim([2.5 maxx+.15])
        ylim([2 6])
        set(gca,'XTick',-1:17:16);set(gca,'YTick',-1:17:16);
        axis equal
        colorbar
    end
end
%% model results plotting  look at track 11 and 14 at end of sens3
skip=0;
if skip==1
    sens=3;
    tracks=[5 11 14];
    temp=min(TIME(:,tracks,sens),[],2);
    h_mod=sqrt((10000*k./(2*(pi*alpha*temp).^.5)).^2+755^2);
    start=find(h_mod>756,1,'first');
    figure
    plot(t_plt_mod(start:3265)-3,h_mod(start:3265)/755,'r.');hold all
    plot(t-3,h_co(sens,:)/755,'k-');ylim([0 2.5]);xlim([0 13.08])
    plot([0 13.08],[1.285 1.285],'b--');plot([0 13.08],[1 1],'b-')
    legend('Model','Measrued','Mean Turbulent','Mean Laminar','Location','SouthEast')
    ylabel('St/St_l_a_m');xlabel('t (seconds)')
end
%% plots of vortex properties during interaction for s3 track 11 and 14
skip=0;
if skip==1
    mc={'k' 'k' ,'k'};
    figure(100)
    sens=3;
    tracks=[5 11 14];
    stopp=[111 500 355];
    startt=[1 30 8];
    ds=1;
    for ii=1:length(tracks)
        plot(downsample(t_t(startt(ii):stopp(ii),tracks(ii))/250-
3,ds),downsample(d_t(startt(ii):stopp(ii),tracks(ii))/BL,ds),strcat(mc{ii},'+'),'MarkerSize',5);h
old all%%distance from vortex to sensor
        plot(downsample(t_t(startt(ii):stopp(ii),tracks(ii))/250-
3,ds),2*downsample(abs(circ_t(startt(ii):stopp(ii),tracks(ii))),ds),strcat(mc{ii},'d'),'MarkerSiz
e',5)%%circulation of vortices
    end
    h=legend('d_{OA}','Circulation','Location','NorthWest');%legend('boxoff')
    grid on
    xlim([9.5 13.5]-3);ylim([0 20])
    figure(101)
    for ii=1:length(tracks)
        plot(downsample(t_t(startt(ii):stopp(ii),tracks(ii))/250-
3,ds),downsample(d3_t(startt(ii):stopp(ii),tracks(ii))/BL,ds),strcat(mc{ii},'+'),'MarkerSize',5);
hold all%%distance within BL
        plot(downsample(t_t(startt(ii):stopp(ii),tracks(ii))/250-
3,ds),2*downsample((Vind_t(startt(ii):stopp(ii),tracks(ii))),ds),strcat(mc{ii},'d'),'MarkerSize',
5)%%induced velocity at sensor
    end
    h=legend('d_{BA}','V_{IND}','Location','NorthWest');legend('boxoff')
```

```
    xlim([9.5 13.5]-3);ylim([0 6])
    grid on
end
%% plot vortex tracks for track 5 11 and 14
skip=1;
if skip==1
    track_number=5;stopper=10.34*250;
    temp=MASTER_TRACK(:,:,track_number);
    stopper2=find(temp(:,1)>stopper,1,'first');
    temp1=temp(1:stopper2,:);
    track_number=14;stopper=11.66*250;
    temp=MASTER_TRACK(:,:,track_number);
    stopper2=find(temp(:,1)>stopper,1,'first');
    temp2=temp(1:stopper2,:);
    track_number=11;stopper=13.064*250;
    temp=MASTER_TRACK(:,:,track_number);
    stopper2=find(temp(:,1)>stopper,1,'first');
    temp3=temp(1:stopper2,:);
    final_props=cat(1,temp1,temp2,temp3);
    t_ind=(final_props(:,1)-750)/250;
    xv1=smooth(temp1(:,2),35,'loess');yv1=smooth(temp1(:,3),35);
    xv2=smooth(temp2(:,2),35,'loess');yv2=smooth(temp2(:,3),35);
    xv3=smooth(temp3(:,2),35,'loess');yv3=smooth(temp3(:,3),35);
    xv=cat(1,xv1,xv2,xv3);yv=cat(1,yv1,yv2,yv3);
    Circ=(final_props(:,4));
    figure(10)
    I=125;J=157;
    maxx=(I+2)*8*52/10000;maxy=52/10000*1280;gagelocy=.28285:2.54*.25:6;gagelocx=maxx*ones(1,10);
    ddd=colormap(jet(128));
    close all
    for ii=1:8:length(xv)
        CC=ceil(128*((t_ind(ii)-(t_ind(1)-.5))/(1+range(t_ind))));

plot(8*52/10000*xv(ii),8*52/10000*yv(ii),'ko','MarkerSize',.01+3*abs(Circ(ii)),'MarkerEdgeColor',
'k','MarkerFaceColor',ddd(CC,:));hold all
        hold all
    end
    for ii=1:8:128
        CC=ceil(128*((t_ind(ii)-(t_ind(1)-.5))/(1+range(t_ind))));

plot(8*52/10000*xv(ii),8*52/10000*yv(ii),'ko','MarkerSize',.01+3*abs(Circ(ii)),'MarkerEdgeColor',
'k','MarkerFaceColor',ddd(CC,:));hold all
        hold all
    end
    time=[final_props(1,1) final_props(length(final_props))]/250-3;
    patch([maxx maxx+.15 maxx+.15 maxx],[0 0 maxy maxy],[.5 .5 .5])
    plot(gagelocx(1),gagelocy(8),'k.','MarkerSize',30)
    caxis([time(1)-.5 time(2)+.5])
    ylim([2 6.5])
    set(gca,'XTick',1.983:5*.11:16);set(gca,'YTick',2:5*.11:16);
    axis equal
    colorbar
    figure
    sensors=[3];
    h_plot=h_co(sensors,(time(1)+2.5)*1000:(time(2)+3.5)*1000)/755;
    pt=(time(1)-.5):.001:time(2)+.5;
    skipper=[250:500:length(h_plot)];
    plot(pt,h_plot(1,:),'k-');ylabel('St/St_l_a_m');hold all
    ylim([.5 2]);xlim([time(1)-.5 time(2)+.5])
end

%%Written by David Hubble 2-5-10
%%Makes one master array of vortex parameters and saves as a mat file for
%%easy loading
clc;clear all;close all

folder={'Grid1','Grid2','Grid3'};%test name
test={'3','4','5'};%test number
num_POD=3270;%number of frames total
direc='Y:\puddinpop\Hubble\Feb_2010_tests\Stagnation\';
for GG=1:3;
```

```
    for tst=1:3;

basename=strcat(direc,folder{GG},'\test',test{tst},'\Vortex\test',test{tst},'_vortarray_step_');
        VMA=zeros(50,5,num_POD);%zero master array
        for i=1:num_POD
            load(strcat(basename,num2str(i),'CI.mat'))%load each vortex tempmat for each time
            [r,c]=size(tempmat);
            VMA(1:r,:,i)=tempmat;
            disp(i)
        end

sname=strcat(direc,folder{GG},'\test',test{tst},'\Vortex\test',test{tst},'_MASTER_ARRAY_CI.mat');
        disp('saving...')
        save(sname,'VMA','num_POD')
        disp('done')
    end
end
```

7.4.3 Simulation of heat flux sensors

```
%%%%1D transient conduction, implicit, two non similar materials
%%%Written by David Hubble 7-14-08

clc; clear all; close all;
plott=5;                              %%control what plots are created, 5 makes shaded error plot
%%% IC and BC
Tinf1=398;                            %%used for convection at side 1
h0=000;                               %%convection co at side 1
q0=10000;                            %%constant heat flux into side 1
Freq=5;%[1:2:10];                     %%%Used to give frequency range for TF calculation
T0=298;                               %%starting temperature of entire system
Tinf2=T0;                             %%used for convection at side 2
h2=1e10;                              %%convection co at side 2
Error=2.05;                           %%percent, used to find time to accuracy
%%%Test parameters
Time=1;                               %%duration of test
Fs=1000;                             %%Sample frequency for finite difference
yhigh=4;                              %%*mean(q1), used for plot limits;
noise=0;                              %%allows for noise to be added to temperature measurements
%%%Material A properties
KA=[.288 2.2 22 220];                      %%thermal conductivities
ka=KA(1);                             %%pull off thermal conductivity
rhoa=1420;                            %%density of mat A
ca=1090;                               %%Specific heat of mat A
% La=.125*.0254;                       %%thickness of mat A
La=.000120;
%%%Material B properties
n=0;%-2:4:2%:8:4;%-2:2:2;                          %%Orders of magnitude for k of mat B
XX=[10.^n];                           %%Values to multiply ka to get kb
% KB=ka*XX;                            %%calculation of kb
KB=11.6;
FO=.01:.002: 1.5;                     %%FO numbers to get error at in time
Es1=zeros(length(FO),length(XX));     %%initialize
Ed1=zeros(length(FO),length(XX));     %%initialize
En1=zeros(length(FO),length(XX));     %%initialize
for z=1:length(XX)                    %%loop to step through mat B properties, let n=constant to
eliminate loop effect
    for zz=1:length(Freq)             %%loop to step through changing q0 for TF calc, let
Freq=constant to eliminate loop effect
        freq=Freq(zz);                %%set new frequency
        kb=KB(z);                     %%set kb for this z value in loop
        rhob=7278;                    %%density of mat B
        cb=548;                       %%specific heat of mat B
        Lb=300*La;                     %%thickness of mat B + thickness of mat A, i.e. let Lb=La
if thickness of mat B is zero
        dx=La/100;                    %%set number of grid points in mat A, will be used as spacing
in mat B
        dt=1/Fs;                      %%time step
```

```
        %%%Initialization
        pp=round(Fs*Time);          %%number of time points
        ii=round(La/dx);            %%number of grid points in mat A
        iii=round(Lb/dx);           %%total number of grid points
        ab=kb/(cb*rhob);            %%alpha of mat B
        aa=ka/(rhoa*ca);            %%alpha of mat A
        q1=zeros(1,pp);             %%initialize
        q2=zeros(1,pp);             %%initialize
        TC1=zeros(1,pp);            %%initialize
        TC2=zeros(1,pp);            %%initialize
        t=zeros(1,pp);              %%initialize
        R(1:iii)=T0;                %%use varible R to represent all T values at last time step,
this means all Ts in x and t need not be stored since new Ts are always function of old Ts
        TC1(1)=T0;TC2(1)=T0;        %%TC1 and TC2 are the two thermocouple location, initialize
at intial temperature T0
        t(1)=0;                     %%initialize time varible

        Foa=aa*dt/dx^2;             %%FO number for mat A, used in solver
        Fob=ab*dt/dx^2;             %%FO number for mat B, used in solver
        Bia=h0*dx/ka;               %%Biot number for mat A, used in solver
        Bib=h2*dx/kb;               %%Biot number for mat B, used in solver

        i=1:ii;j=ii:iii;            %%stepping vectors, i in mat A, j in mat B
        a=zeros(1,iii);
        %%%%Setup Tridiagonal Solver Using Thomas Algorithm
        a(i)=-1*Foa;a(j)=-1*Fob;a(ii)=-ka;a(1)=0;a(iii)=-2*Fob;
        c=a;c(1)=-2*Foa;c(iii)=0;c(ii)=-kb;                                 %%%%
        %%%%Step through in time solving at each step                       %%%%
        for j=2:pp;                                                         %%%%
            %         Trad=T0+.3*T0*sin(5*j*dt);
            %%Allows for changing radiation source temp
            %         q0=5.67e-8*(Trad^4-R(1)^4);
            %%uncomment to allow for radiation
            %         q0=10000*sin(2*pi*freq*j*dt);
            %%allows changing heat source at side 1
            d(1)=R(1)+2*Foa*(q0*dx/ka+Bia*Tinf1);                           %%%%
            d(ii)=((rhoa*ca+rhob*cb)*(dx^2/(2*dt)))*R(ii);                  %%%%
            d(iii)=R(iii)+2*Fob*Bib*Tinf2;                                  %%%%
            b(1)=1+2*Foa+2*Foa*Bia;                                         %%%%
            b(ii)=((ka+kb)+(rhoa*ca+rhob*cb)*dx^2/(2*dt));                  %%%%
            b(iii)=1+2*Fob+2*Fob*Bib;                                       %%%%
            for i=2:ii-1            %%solve in mat A
                b(i)=1+2*Foa;                                               %%%%
                d(i)=R(i);                                                  %%%%
            end                                                             %%%%
            for i=ii+1:iii-1        %%solve in mat B
                b(i)=1+2*Fob;                                               %%%%
                d(i)=R(i);                                                  %%%%
            end                                                             %%%%
            T=tridiagSolve(a,b,c,d);                                        %%%%
            q1(j)=q0+h0*(Tinf1-R(1));                                       %%Q into side 1
            q2(j)=ka*(T(ii-1)-T(ii-0))/dx;                                  %%Q into mat B
            t(j)=(j-1)*dt;                                                  %%time at step j
            TC1(j)=T(1)+noise*rand;                                         %%pull off temperature at
side 1
            TC2(j)=T(ii)+noise*rand;                                        %%pull off temperature at
interface
            R=T;                                                            %%R will represent Tp-1
in step p
        end
        SF=1/Fs;                                                            %%Sample freq, used to
downsample temp data to that of experiments
        tc1=downsample(TC1,round(SF/dt));                                   %%downsample temp data
        tc2=downsample(TC2,round(SF/dt));                                   %%downsample temp data
        t=downsample(t,round(SF/dt));                                       %%downsample time
        q1=downsample(q1,round(SF/dt))/10000;                               %%downsample q1
        differential=(ka*(tc1-tc2)/La)/10000;
        slug=(rhoa*La*ca*diff(.5*(tc1+tc2))/SF)/10000;
        new = zeros(1,length(tc1)-1);
        B(1)=ka/La;B(2)=rhoa*La*ca;%Differential and Capacitance constants
        for i=2:length(tc1)-1;
```

```
            new(i)=(B(1)*(tc1(i)-tc2(i))+Fs/4*B(2)*(tc1(i)+tc2(i)-tc1(i-1)-tc2(i-1)))/10000;
        end
        LL=length(slug);
        foa=La^2/aa;
        Es=(100*(slug(1:LL)-q1(1:LL))./q1(1:LL));%calculates errors as a function of time for
three methods
        Ed=(100*(differential(1:LL)-q1(1:LL))./q1(1:LL));
        En=(100*(new(1:LL)-q1(1:LL))./q1(1:LL));
        plot(t,q1,t(1:length(new)),new,t,differential)
        asdf
        aratio(z)=aa/ab;
        t=t*aa/La^2;
        yhigh2=yhigh*mean(q1);
        ylow=0;
        figure(1000*z+10*zz)
        subplot(3,1,1)
        plot(t(1:LL),slug,'r-',t,q1,'k-');ylim([ylow yhigh2]),xlabel('Fo_s_e_n_s_o_r - t ^.
\alpha/\delta^2'),ylabel('q"/q"_0'),legend('Slug Calorimeter','Actual Heat Flux')
        title(['\alpha_a / \alpha_b= ',num2str(aa/ab)])
        subplot(3,1,2)
        plot(t,differential,'r-',t,q1,'k-'),ylim([ylow yhigh2]),xlabel('Fo_s_e_n_s_o_r - t ^.
\alpha/\delta^2'),ylabel('q"/q"_0'),legend('Differential Sensor','Actual Heat Flux')
        subplot(3,1,3)
        plot(t(1:LL),new,'r-',t,q1,'k-');ylim([ylow yhigh2]),xlabel('Fo_s_e_n_s_o_r - t ^.
\alpha/\delta^2'),ylabel('q"/q"_0'),legend('New Method','Actual Heat Flux')
    end
end
%%
Z=real(log(1-differential));
figure
plot(Z)
sad
% %%%%%%%%%%%%%%%%%%%%%%%%lines to fill in shaded plots
if plott==5
    m=200;
    figure(23532)
    for i=1:length(n)
        plot(FO,En1(:,i),'k-',FO,Es1(:,i),'r-',FO,Ed1(:,i),'b-');hold on;ylim([-100 100])
    end
    %%%%%%%%%%%%%%%%%%%%%%%%EVERYTHING NEEDED FOR SHADED PLOTS
    X=cat(2,FO,fliplr(FO));

Yd=cat(2,max(Ed1'),fliplr(min(Ed1')));Yn=cat(2,max(En1'),fliplr(min(En1')));Ys=cat(2,max(Es1'),fl
iplr(min(Es1')));
    patch(X,Yn,'k','FaceAlpha',.6)
    hold on
    patch(X,Ys,'r','FaceAlpha',.6);
    for i=1:15
        ytemp=m*FO+30*i-400;
        in=inpolygon(FO,ytemp,X,Ys);
        reg=find(in);
        plot(FO(reg),ytemp(reg),'k-')
    end
    patch(X,Yd,'b','FaceAlpha',.6);
    for i=1:15
        ytemp=-1*m*FO+30*i-40;
        in=inpolygon(FO,ytemp,X,Yd);
        reg=find(in);
        plot(FO(reg),ytemp(reg),'k-')
    end
    grid
    ylim([-100 100]);xlabel('Fourier Number');ylabel('% Error')
    legend('HHF_1 Method','Slug
Calorimeter','Differential');set(gca,'XTick',0:.25:1.5);set(gca,'YTick',-100:50:100);
end

function [y]=tridiagSolve(a,b,c, d)
%%%%%%%%%%%%%%%%%%%%%%%%%%%%%%%%%%%%%%%%%%%%%%%%%%%%%%%%%%%%%%%%
% Program: thomas
% To solve a tridiagonal
% linear system using the
```

```
% Thomas algorithm
% The ith equation is:
% a(i)*y(i-1) + b(i)*y(i) + c(i)*y(i+1) = d(i)
% N x N matrix
% note that a(1)=0 and c(N)=0
% Andrew Duggleby 2007
%%%%%%%%%%%%%%%%%%%%%%%%%%%%%%%%%%%%%%%%%%%%%%%%%%%%%%%%%%%%%%%%%%%%%%%%%%%%
N=length(d);
for k=2:N
    m=a(k)/b(k-1);
    b(k)=b(k)-m*c(k-1);
    d(k)=d(k)-m*d(k-1);
end
y(N)=d(N)/b(N);

for k=N-1:-1:1
    y(k)=(d(k)-c(k)*y(k+1))/b(k);
end


%%written by David Hubble 12-22-09
%%looks at an electrical analog of the THeTA sensor and solves the
%%resulting coupled ODEs
close all;clear all;clc
[t,T]=ode45(@DAVE_eanalog,[0:.0002:.4],[0 0 0 0 0 0 0 0]);
[r,c]=size(T);
figure
for i=1:8
    plot(t,T(:,i)/T(r,i));hold all
end
xlim([0 1])
FS=(t(2)-t(1))^-1;
diff_fin=6.1729;
differ=1618.4*(T(:,3)-T(:,7));
ATemp=(.5*T(:,3)+.5*T(:,7));
slug=FS*1*317*diff(ATemp);slug(length(differ))=0;
% ratio=diff./diff_fin;
HHF=differ+.5*slug;
figure
plot(t,differ,t,HHF)
t90=t(find(ratio>.90,1,'first'));
t95=t(find(ratio>.95,1,'first'));
t98=t(find(ratio>.98,1,'first'));
tau=t(find(ratio>.632,1,'first'))
figure
first=(1-exp(-1*t/tau));
plot(t/tau,ratio,'k-',t/tau,first,'r-','MarkerSize',2);xlabel('t/\tau');xlim([0 4])
legend('(TC_1-TC_2)/\DeltaT_\infty','1-e^-^t^/^\tau','Location','SouthEast')
figure
plot(t,ratio./first);xlim([0 .1])
figure
plot(t,log(1-ratio),t,-1*t/tau);xlim([0 .4]);ylabel('ln(1-q_0/q_i_n)');xlabel('Seconds')

function dT=DAVE_eanalog(t,T,R1)
%%%inputs to ODE45 to solve the coupled ODEs in the electrical analog
dT=zeros(7,1);
cm=87;%metal specific heat
cg=33;%glue specific heat
ck=77;%kapton specific heat
cp=45;%paint specific heat
rm=6.2e-7;%metal resitance
rg=1e-4;%glue resistance
rk=4.1667e-4;%kapton resistance
rp=3.378e-5;%paint resistance

q=10000*sin(2*pi*10*t);%qin

dT(1)=(1/cp)*(q-(T(1)-T(2))/(.5*rp+.5*rg));
dT(2)=(1/cg)*((T(1)-T(2))/(.5*rp+.5*rg)-(T(2)-T(3))/(.5*rg+.5*rm));
dT(3)=(1/cm)*((T(2)-T(3))/(.5*rg+.5*rm)-(T(3)-T(4))/(.5*rm+.5*rg));
```

```
dT(4)=(1/cg)*((T(3)-T(4))/(.5*rm+.5*rg)-(T(4)-T(5))/(.5*rg+.5*rk));
dT(5)=(1/ck)*((T(4)-T(5))/(.5*rg+.5*rk)-(T(5)-T(6))/(.5*rk+.5*rg));
dT(6)=(1/cg)*((T(5)-T(6))/(.5*rk+.5*rg)-(T(6)-T(7))/(.5*rg+.5*rm));
dT(7)=(1/cm)*((T(6)-T(7))/(.5*rg+.5*rm)-(T(7)-T(8))/(.5*rm+.5*rg));
dT(8)=(1/cg)*((T(7)-T(8))/(.5*rm+.5*rg)-(T(8)-0)/(.5*rg));
```

7.5 References

Adrian, R. J. (2007). "Hairpin vortex organization in wall turbulence." Physics of Fluids **19**(4): -.

Anthony, R. J., T. V. Jones, et al. (2005). "High frequency surface heat flux imaging of bypass transition." Journal of Turbomachinery-Transactions of the Asme **127**(2): 241-250.

Arevalo, G., R. H. Hernandez, et al. (2007). "Vortex ring head-on collision with a heated vertical plate." Physics of Fluids **19**(8): -.

ASTM (1981). Manual on the Use of Thermocouples in Temperature Measurement. Baltimore.

Baines, W. D. and E. G. Peterson (1951). "An Ivestigation of Flow Through Screens." ASME Jounral of Heat Transfer **73**: 467-480.

Bizzak, D. J. and M. K. Chyu (1995). "Use of a Laser-Induced Fluorescence Thermal Imaging-System for Local Jet Impingement Heat-Transfer Measurement." International Journal of Heat and Mass Transfer **38**(2): 267-274.

Blackwelder, R. (1988). "Coherent Structures Associated with Turbulent Transport." Transport Phemomena in Turbulent Flows: 69-88.

Chong, M. S., A. E. Perry, et al. (1990). "A General Classification of 3-Dimensional Flow-Fields." Physics of Fluids a-Fluid Dynamics **2**(5): 765-777.

Coleman, C. W. and W. G. Steele (1989). Experimentation and Uncertainty Analysis for Engineers. New York, John Wiley & Sons.

Diller, T. E. (1993). Advances in Heat Flux Measurement. Advances in Heat Transfer. Boston, Academic Press**:** 279-368.

Doebelin, E. O. (2004). Measurement Systems: Application and Design, Fifth Edition. New York, McGraw Hill.

Doligalski, T. L., C. R. Smith, et al. (1994). "Vortex Interactions with Walls." Annual Review of Fluid Mechanics **26**: 573-616.

Eckstein, A. C. and P. Vlachos (2009). "Digital Particle image Velocimetry (DPIV) Robust Phase Correlation." Measurement Science & Technology **20**: 14.

Epstein, A. H., G. R. Guenette, et al. (1986). "High-Frequency Response Heat-Flux Gauge." Review of Scientific Instruments **57**(4): 639-649.

Ewing, J. A. (2006). **Development of a direct-measurement thin-film heat flux array**. Mechanical Engineering. Blacksburg, Virginia Tech. **M.S.**

Ewing, J. A., A. R. Gifford, et al. (2010). "Development of a Direct-Measurement Thin-Film Heat Flux Array." Measurement Science & Technology **21**(10).

George, W. K., W. J. Rae, et al. (1991). "An Evaluation of Analog and Numerical Techniques for Unsteady Heat-Transfer Measurements with Thin-Film Gauges in Transient Facilities." Experimental Thermal and Fluid Science **4**(3): 333-342.

Gifford, A. R., T. E. Diller, et al. "The Physical Mechanism of Heat Transfer Augmentation in Stagnating Flows Subject to Freestream Turbulence." in press ASME Jounral of Heat Transfer.

Gifford, A. R., A. Hoffie, et al. (2009). "Convection Calibration of Schmidt-Boelter Heat Flux Gages in Shear and Stagnation Air Flow." accepted to ASME Journal of Heat Transfer.

Gifford, A. R., D. O. Hubble, et al. (2010). "Durable Heat Flux Sensor for Extreme Temperature and Heat Flux Environments." Journal of Thermophysics and Heat Transfer **24**(1): 69-76.

Goldstein, S. (1938). Modern Devlopments in Fluid Dynamics. Oxford, Clarendon Press.

Hager, J. M., S. Simmons, et al. (1991). "Experimental Performance of a Heat-Flux Microsensor." Journal of Engineering for Gas Turbines and Power-Transactions of the Asme **113**(2): 246-250.

Hager, N. E. J. (1965). "Thin Foil Heat Meter." Review of Scientific Instruments **36**: 1564-1570.

Hightower, T. M., R. A. Olivares, et al. (2008). "Thermal Capacitance (Slug) Calorimeter Theory Including Heat Losses and Other Decaying Processes." NASA **TM-200-0215364**.

Holmberg, D. G. and T. E. Diller (1995). "High-frequency heat flux sensor calibration and modeling." Journal of Fluids Engineering-Transactions of the Asme **117**(4): 659-664.

Holmberg, D. G. and T. E. Diller (2005). "Simultaneous heat flux and velocity measurements in a transonic turbine cascade." Journal of Turbomachinery-Transactions of the Asme **127**(3): 502-506.

Hubble, D. O. and T. E. Diller (2010). "Development and Evaluation of the Time-resolved Heat and Temperature Array." J. Thermal Sci. Eng. Appli. **2**(3).

Hubble, D. O. and T. E. Diller (2010). "A Hybrid Method for Measuring Heat Flux." Journal of Heat Transfer-Transactions of the Asme **132**(3): -.

Hutchins, N. and I. Marusic (2007). "Evidence of very long meandering features in the logarithmic region of turbulent boundary layers." Journal of Fluid Mechanics **579**: 1-28.

Incropera, F. and D. DeWitt (2002). Introduction to Heat Transfer, 5th ed. New York.

Kidd, C. (1983). Determination of the Uncertainty of Experimental Heat-Flux Calibrations. AEDC Report TR-83-13.

Kidd, C. T. and J. C. Adams (2001). "Fast-response heat-flux sensor for measurement commonality in hypersonic wind tunnels." Journal of Spacecraft and Rockets **38**(5): 719-729.

Kidd, C. T., C. G. Nelson, et al. (1994). "Extraneous Thermoelectric EMF Effects Resulting from the Press-Fit Installation of Coaxial Thermocouples in Metal Models." Int. Instrum. Symp. **40th**: 317-335.

Liebert, C. H. (1992). "High Temperature Plug-Type Heat Flux Gauges." NASA **TM 105403**.

Martin, R. and R. Zenit (2008). "Heat transfer resulting from the interaction of a vortex pair with a heated wall." Journal of Heat Transfer-Transactions of the Asme **130**(5): -.

Marusic, I., R. Mathis, et al. (2010). "Predictive Model for Wall-Bounded Turbulent Flow." Science **329**(5988): 193-196.

Moffat, R. J. (1985). "Using Uncertainty Analysis in the Planning of an Experiment." Journal of Fluids Engineering-Transactions of the Asme **107**(2): 173-178.

Moss, R. W. and M. L. G. Oldfield (1996). "Effect of free-stream turbulence on flat-plate heat flux signals: Spectra and eddy transport velocities." Journal of Turbomachinery-Transactions of the Asme **118**(3): 461-467.

Mosyak, A., E. Pogrebnyak, et al. (2001). "Effect of constant heat flux boundary condition on wall temperature fluctuations." Journal of Heat Transfer-Transactions of the Asme **123**(2): 213-218.

Murthy, A. V., B. K. Tsai, et al. (2000). "NIST Radiative Heat-Flux Sensor Calibration Facilites and Techniques." Journal of Research of the National Institute of Standards and Technology **105**(2): 293-305.

Nasir, H., S. V. Ekkad, et al. (2007). "Effect of tip and pressure side coolant injection on heat transfer distributions for a plane and recessed tip." Journal of Turbomachinery-Transactions of the Asme **129**(1): 151-163.

Nix, A. C., T. E. Diller, et al. (2007). "Experimental measurements and modeling of the effects of large-scale freestream turbulence on heat transfer." Journal of Turbomachinery-Transactions of the Asme **129**(3): 542-550.

Oishi, T., S. Gorbunov, et al. (2006). Thermal Sensor Development and Testing for NASA Entry Probe Thermal Protection Systems. AIAA Aerospace Sciences Meeting and Exhibit. Reno, NV. **44th**.

Ortolano, D. J. and F. F. Hines (1983). A Simplified Approach to Heat Flow Measurement. Advances in Instrumentation. Research Triangle Park. **38:** 1449-1456.

Ostrach, S. (1953). "An Analysis of Laminar Free-Convection Flow and Heat Transfer About a Flat Plate Parallel tot he Direction of the Generating Body Force." National Advisory Committee for Aeronautics, Report 1111.

Panton, R., Ed. (2005). Incompressible Flow. Hoboken, John Wiley & Sons.

Piccini, E., S. M. Guo, et al. (2000). "The development of a new direct-heat-flux gauge for heat-transfer facilities." Measurement Science & Technology **11**(4): 342-349.

Pitts, W. M., A. V. Murthy, et al. (2006). "Round robin study of total heat flux gauge calibration at fire laboratories." Fire Safety Journal **41**(6): 459-475.

Pullin, D. I. (1979). "Vortex Ring Formation at Tube and Orifice Openings." Physics of Fluids **22**(3): 401-403.

Raffel, M., C. Willert, et al. (2007). Particle Image Velocimetry, Springer.

Romero-Mendez, R., M. Sen, et al. (1998). "Enhancement of heat transfer in an inviscid-flow thermal boundary layer due to a Rankine vortex." International Journal of Heat and Mass Transfer **41**(23): 3829-3840.

Rooke, S., G. Fralick, et al. (1998). "Heat transfer analysis of a plug-type heat flux gauge." Journal of Thermophysics and Heat Transfer **12**(4): 536-542.

Schultz, D. L. and T. V. Jones (1973). "Heat Transfer Measurements in Short Duration Hypersonic Facilities." AGARDograph **165**.

Shariff, K. and A. Leonard (1992). "Vortex Rings." Annual Review of Fluid Mechanics **24**: U235-U279.

Simmons, S. G., J. M. Hager, et al. (1990). "Simultaneous Measurements of Time-Resolved Surface Heat-Flux and Freestream Turbulence at a Stagnation Point." Heat Transfer 1990, Vols 1-7: 375-380.

Sutera, S. (1965). "Vorticity Amplification in Stagnation-Point Flow and its Effect on Heat Transfer." Journal of Fluid Mechanics **21**: 513-534.

Tanaeva, S. A. and L. E. Evseeva (1997). "Thermophysical Properties of Epoxy Compounds at Low Temperatures." Jounral of Engineering Physics and Thermophysics **70**.

Thole, K. A. and D. G. Bogard (1995). "Enhanced Heat-Transfer and Sheer Stress Due to High Free-Stream Turbulence." Journal of Turbomachinery-Transactions of the Asme **117**(3): 418-424.

Vanfossen, G. J. and R. J. Simoneau (1987). "A Study of the Relationship between Free-Stream Turbulence and Stagnation Region Heat-Transfer." Journal of Heat Transfer-Transactions of the Asme **109**(1): 10-15.

Walker, D. G. and E. P. Scott (1998). "Evaluation of estimation methods for high unsteady heat fluxes from surface measurements." Journal of Thermophysics and Heat Transfer **12**(4): 543-551.

Walker, J. D. A., C. R. Smith, et al. (1987). "The Impact of a Vortex Ring on a Wall." Journal of Fluid Mechanics **181**: 99-140.

Wang, Z., P. T. Ireland, et al. (1995). "An Advanced Method of Processing Liquid-Crystal Video Signals from Transient Heat-Transfer Experiments." Journal of Turbomachinery-Transactions of the Asme **117**(1): 184-189.

Wei, C. Y. and J. J. Miau (1992). "Stretching of Freestream Turbulence in the Stagnation Region." Aiaa Journal **30**(9): 2196-2203.

Westerweel, J. (1997). "Fundamentals of digital particle image velocimetry." Measurement Science & Technology **8**(12): 1379-1392.

White, F. M. (1974). Viscous Fluid Flow. New York, Mcgraw Hill.

Xiong, Z. M. and S. K. Lele (2007). "Stagnation-point flow under free-stream turbulence." Journal of Fluid Mechanics **590**: 1-33.

Zhou, J., R. J. Adrian, et al. (1999). "Mechanisms for generating coherent packets of hairpin vortices in channel flow." Journal of Fluid Mechanics **387**: 353-396.

7.6 Copyright Transfer Material

The following form was obtained from the ASME which allows the reproduction of chapters 4 and 5.

Dave Hubble

From: Beth Darchi [DarchiB@asme.org]
Sent: Friday, March 25, 2011 2:02 PM
To: 'dhubble@vt.edu'
Subject: FW: ASME PUBLICATIONS PERMISSION REQUEST FORM SUBMISSION

Follow Up Flag: Follow up
Flag Status: Flagged

Categories: Red Category

Dear Mr. Hubble:
It is our pleasure to grant you permission to use the following ASME materials:

- "Development and evaluation of the time-resolved heat and temperature array," by David Hubble, Tom Diller, Journal of thermal science and engineering application, Vol. 2, 2010;
- "A hybrid method for measuring heat flux," by David Hubble, Tom Diller, Journal of heat transfer, Vol. 132, 2010

cited in your letter for inclusion in a Doctoral Thesis entitled An experimental investigation of the mechanism of heat transfer augmentation by coherent structures to be published by Virginia Tech.

As is customary, we ask that you ensure full acknowledgment of this material, the author(s), source and ASME as original publisher on all printed copies being distributed.

Many thanks for your interest in ASME publications.

Sincerely,

Beth Darchi
Permissions & Copyrights
ASME, 3 Park Avenue
New York, NY 10016
T: 212-591-7700
F: 212-591-7841
E: darchib@asme.org